Bachelor Thesis

Degree Project in
Marine Geology 30 hp

Bottom Morhpology of Lake Siljan

Linda Hoff

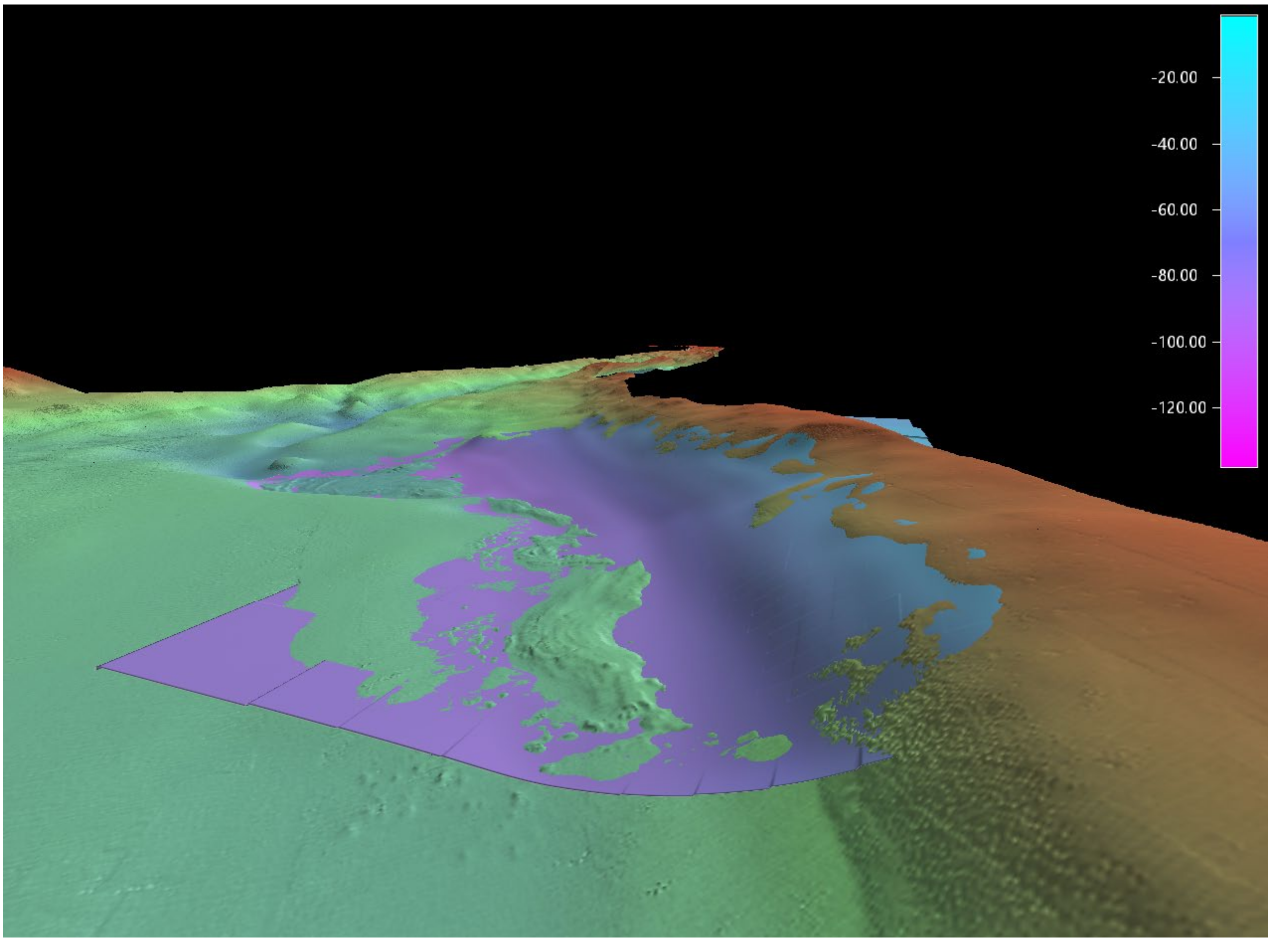

Stockholm 2022

Department of Geological Sciences
Stockholm University
SE-106 91 Stockholm

Abstract

Lake Siljan is located in the southern part of the Siljan impact structure in south central Sweden. The Weichselian Fennoscandian Ice Sheet left the area covered by glacial landforms indicating a complex deglaciation history. Glacial landforms found in marine, and sometimes also lacustrine environments, are often better preserved than glacial landforms situated on land and may give valuable information about past ice sheets and, in particular, the conditions during deglaciation. A geophysical survey was performed in the southern part of Lake Siljan in 2020 for a project aiming to reconstruct the deglacial history of the area. The survey revealed a complex bathymetry in what is interpreted to be the pre-glacial river valley of Österdalälven. In this river valley, glacial landforms indicating a subglacial drainage system and several mass-transport deposits (MTD) are identified in this present study. Even small subaquatic MTDs may cause tsunamis that pose a threat to humans and human infrastructure. A MTD with a volume of 350-400 000 m^3 generated a tsunami in Statland, Norway in 2014 and caused severe damage to the village. The largest mass transport deposit in the survey area in Lake Sijan has a volume of 678 650 m^3 and is in this study compared to MTDs known to have generated tsunamis to see if a tsunami may have occurred in Lake Siljan.

Keywords: Lake Siljan, glacial landforms, mass-transport deposits, tsunamis, subglacial drainage systems, marine geophysical mapping.

Table of Contents

1. Introduction

Lake Siljan has an area of 293 km^2 (SMHI, 2022) and is situated in the southern part of the Siljan impact structure in south-central Sweden (Figure 1). The area where Lake Siljan is located has a complex deglaciation history, inferred from studies of glacial landforms and sediment records (Möller et al., 2022). Studies of the Lake Siljan basin has also provided information on water discharges and deglaciation rates in the area during the late stages of the last deglaciation (Calles, 1985). Mapping of glacial landforms and other features on lake or seafloors can be done using geophysical mapping methods (Dowdeswell et al., 2016). Glacial landforms in the marine environment, if situated below wave-base, are often protected from erosion and reworking, and are therefore better preserved than if situated on land (Dowdeswell et al., 2016). The same may be true for glacial landforms in lacustrine environments. Even when covered by marine or lacustrine sediments, the glacial landforms on sea or lake floors are often recognizable (Dowdeswell et al., 2016). Glacial landforms can be used for reconstruction of past ice sheets as they give information about the shape, flow and extent of the ice and about deglaciation conditions and past climates (Flink and Noormets, 2018) (Greenwood et al., 2015).

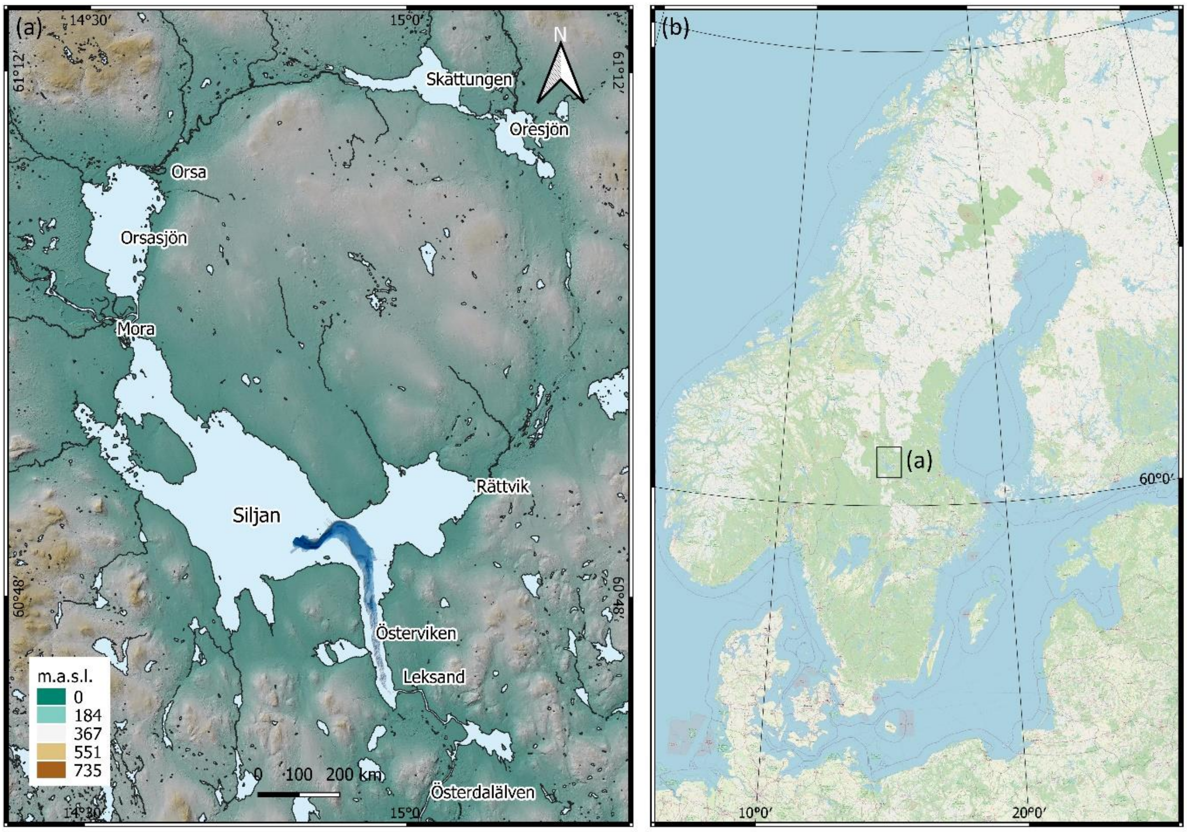

Figure 1. Location of Lake Siljan and the study area. (a) the central dome with its surrounding lakes and the survey area in Lake Siljan that is coloured blue. (b) the location of the Siljan impact structure in south-central Sweden. The map to the left was created from GSD-Elevation data, Grid 2+ ©Lantmäteriet, Quaternary deposites 1:25 000-1:100 0000 ©SGU that was used for water surfaces, and GSD Place-names ©Lantmäteriet. The base of the map to the right is from openstreetmap.org.

Scars caused by subaquatic mass-transport deposits (MTD) may also be found using geophysical mapping. Mass-transport deposits under water pose a threat to humans and human infrastructure because of their tsunami-generating ability. Both large MTDs, like the basin-wide scale Storegga landslide outside the coast of Norway with a volume of 2400-3200 km^3 (Bondevik, 2022), and smaller MTDs like the one that occurred in Skagway Harbor, Alaska in 1994 with a volume of 800 000 m^3 (Rabinovich et al., 1999), may cause tsunamis with a devastating effect on human communities.

In 2020, geophysical mapping of 18.5 km^2 in the southern parts of Lake Siljan in south-central Sweden was executed for a project aiming to reconstruct the deglacial history of the area. A multibeam echosounder and sub-bottom profiler was used, and the results show a complex lake morphology where several scars caused by mass movements can be seen together with eskers and channels. The survey area follows a deep channel that probably has a pre-glacial origin and may be a part of the Österdalälven river valley (Möller et al., 2022).
The main aim of this project is to analyse the lake floor morphology of Lake Siljan, using the available geophysical mapping data from 2020, to determine if glacial landforms can be recognised and used to derive information on the glacial history. In addition, the largest landslide scar found in the area during the 2020 survey is analysed with respect to its dimensions, i.e. size and volume of the mass-wasted material.

2. Background

2.1. Geological Setting

The impact structure where Lake Siljan is situated was created by a meteorite impact in the Late Devonian, approximately 377 Ma (Lehnert et al., 2014; Henkel and Aaro, 2005). It is the largest impact structure in western Europe (Henkel and Aaro, 2005), consisting of a central dome with a size of 28-30 km in diameter, surrounded by a depression where several different lakes are situated (Holm-Alwmark et al., 2017), including Lake Siljan in the south and south-west and Lake Orsa to the west (Figure 1). The total diameter of the ring structure is ~52 km (Möller et al., 2022).

The Siljan impact structure is located at the boundary between the Trans-Scandinavian Igneous Belt (TIB) to the west and older Svecofennian rocks to the east (Figure 2) (Holm et al., 2011). The rocks surrounding Lake Siljan consist mostly of Järna granite and Siljan granite, but also of Svecofennian units to the east and TIB-volcanites and sedimentary rocks to the west, in the ring-depression a megabreccia of Paleozoic sedimentary rocks is found (Figure 2) (Holm-Alwmark et al., 2017) (Holm et al., 2011).

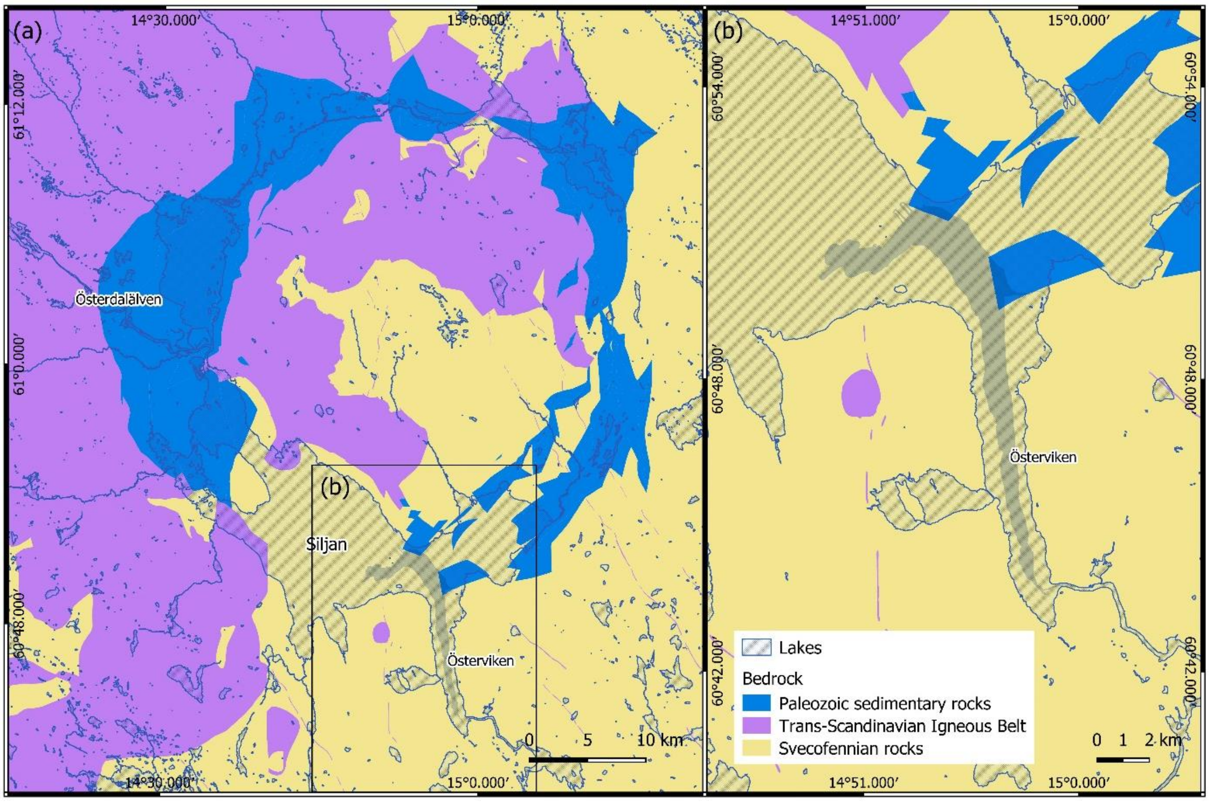

Figure 2. *(a) Bedrock in the area around Lake Siljan. The survey area is shown in gray. (b) Enlargement of the survey area and the area surrounding it. This map was created from Bedrock 1:50 000-1:250 000 ©SGU, GSD Place-names ©Lantmäteriet, and from Quaternary deposits 1:25 000-1:100 0000 ©SGU that was used for the water surfaces.*

The Area around Lake Siljan has an undulating hilly relief, consisting of hills separated by valleys, formed by kaolinitic weathering of fracture zones in the Sub-Cambrian peneplain during the Mesozoic (Lidmar-Bergström and Olvmo, 2015). Since the time of the meteorite impact around 4 km of erosion has occurred (Holm-Alwmark et al., 2017) and the landscape we see today is covered by glacial landforms created by the Weichselian Fennoscandian Ice Sheet (Smith and Peterson, 2014). The central dome is dominated by streamlined terrain in the form of drumlins and ribbed moraines (Möller et al., 2022). Streamlined landforms are produced subglacially at the ice-bed interface by fast-flowing ice or focused ice streams (Dowdeswell et al., 2016). They are directed parallel to the ice flow and some elongated subglacial landforms, like drumlins, have generally a steeper and blunt up-flow side with a tail in the down-flow direction (Dowdeswell et al., 2016). The ice flow in this area, as indicated by the streamlined landforms, was from the north-northwest (Figure 3) (Möller et al., 2022). The depression surrounding the impact crater have directed eskers and glaciofluvial channels (Smith and Peterson, 2014). Sandur deposits and glaciofluvial deltas are found at or above the elevation of the highest shoreline in large areas between the lakes (Möller, 2006). In the lake basins, lacustrine sediments, often containing varves are deposited (Möller, 2006).

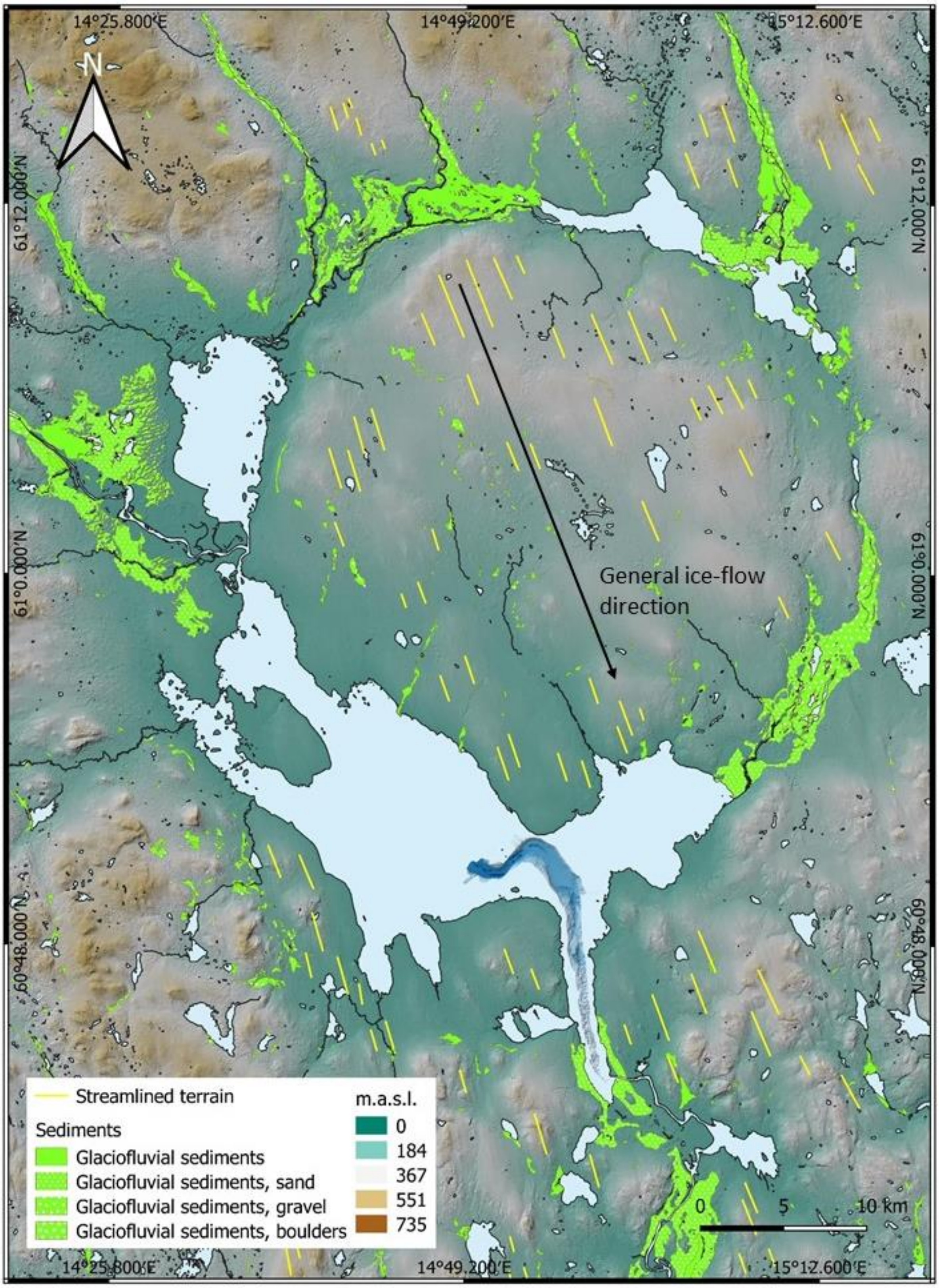

__Figure 3.__ Yellow lines show areas where streamlined terrain is found and their direction is indicating an ice flow from the north-northwest. Areas covered with glaciofluvial sediments are also shown. The streamlined terrain was manually mapped using the topographic data. The map was created from GSD-Elevation data, Grid 2+ ©Lantmäteriet and the areas covered by glaciofluvial sediments comes from Quaternary deposits 1:25 000-1:100 0000 ©SGU.

2.2. Geological history of Lake Siljan

When the Weichselian Fennoscandian Ice Sheet retreated in the area of Lake Siljan around 10,500-10,700 cal. BP (calibrated calendar years Before Present, i.e., 1950) (Möller et al., 2022), the Siljan-Orsa lake basin was covered by the Ancylus Lake, which reached Lake Siljan through the Dalälven river valley (Möller, 2006) (Figure 4). The fresh Ancylus Lake had formed when the outlet of the Yoldia Sea west of Lake Vänern became shallow enough to cause damming and a rise in the water level in the Baltic Basin (Andrén et al., 2011). The damming raised the Ancylus Lake to ca 10 m above the contemporary sea level of the Baltic (Andrén et al., 2011). The highest shoreline of the Ancylus Lake has been mapped around Lake Siljan and reaches 220 m.a.s.l. in the north of the area and 207 m.a.s.l. in the south (Möller et al., 2022). During the last 900 years before Lake Siljan was isolated from the Baltic Basin, the Ancylus Lake had evolved into the initial stage of the Littorina Sea (Möller et al., 2022). The initial Littorina Sea was formed when transgression and flooding caused a new outlet in the south to be established through the Dana River in Denmark (Andrén et al., 2011). The water level soon equilibrated at the North Sea-Atlantic level and saline water could enter the basin creating a brackish sea (Andrén et al., 2011). Isolation of lake Siljan from the Littorina Sea was caused by isostatic uplift (Paradeisis-Stathis, 2020). The Ancient Lake Siljan, covering the Siljan-Orsa lake basin was formed ca 9800 cal BP, with a water level at 168-169 m.a.s.l. (Möller et al., 2022). A re-routing of the outlet of the Ancient Lake Siljan between ca 8800 BP and 8500 BP lowered the water level and the modern Lake Siljan was formed with a lake level at 162 m.a.s.l. (Möller et al., 2022).

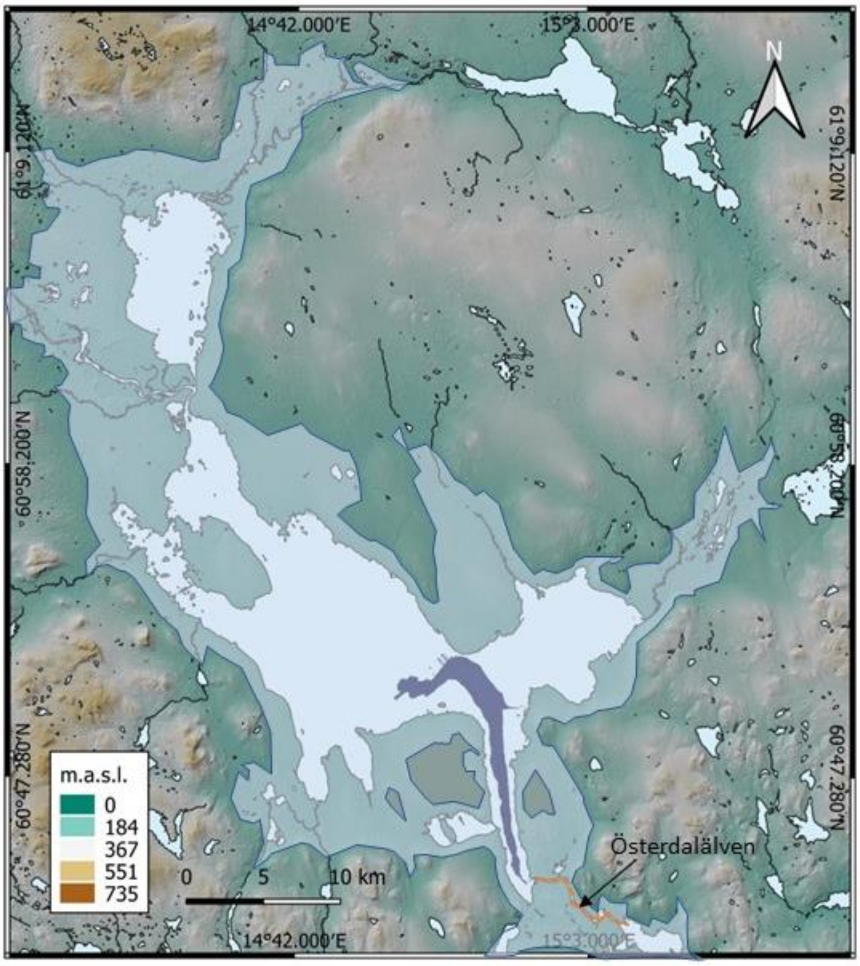

Figure 4. The semi-transparent polygon with a blue outline shows the area covered by the Ancylus Lake after the retreat of the Weichselian Fennoscandian Ice Sheet. The surveyed area of Lake Siljan is shown as a reference and Österdaläven is shown in orange. The map was created from GSD-Elevation data, Grid 2+ ©Lantmäteriet and Quaternary deposits 1:25 000-1:100 0000 ©SGU that was used for the modern water surfaces. The Ancylus Lake level is inferred from Möller et al., 2022.

2.3. Subglacial drainage systems

Eskers and channels, like the ones in Lake Siljan, are landforms found in subglacial drainage systems that are an important part of the glacial system (Simkins et al., 2021). It occurs either in the subglacial sediments or at the interface between the sediments and the ice (Sharp, 2005). The water arrives to the subglacial drainage system from both surface, englacial, subglacial, and groundwater sources and a strong seasonality is often seen if surface melting is the dominant source (Sharp, 2005). Drainage systems may be either slow and distributed, with winding pathways and slow flow velocities, or fast and channelized (Sharp, 2005). The style of drainage may change with the seasons with channelized drainage replacing distributed drainage during increased surface melting in the summer (Simkins et al., 2021). Channelized drainage is controlled by the subglacial topography and the hydraulic gradients and effective pressure caused by the geometry of the ice (Sharp, 2005). The topography effects the ice thickness which in turn influences the hydraulic gradients and effective pressure (Simkins et al., 2021). Transitions between erosion of meltwater channels in the bed and R-channels, where semi-circular channels are cut into the ice above, with esker deposition may occur (Livingstone et al., 2016). Low effective pressure favours the formation of R-channels while erosion of meltwater channels is favoured when the effective pressure is high (Simkins et al., 2021). Changes in the slope of the ice or in the subglacial surface (Livingstone et al., 2016) or thinning of the ice near the ice margin may lead to a change in the style of drainage from erosional meltwater channels to R-channel formation (Simkins et al., 2021). Subglacial water effects ice-sheet dynamics with changes in the subglacial water flow and effective pressure leading to changes in ice flow velocities (Kirkham et al., 2020). A distributed drainage and the presence of basal water leads to higher water pressure and increased ice flow, while a channelized drainage leads to lower effective pressure and a decelerated ice flow (Simkins et al., 2021). Meltwater channels may be used to understand glacial retreat pattens and subglacial channels can indicate the ice flow direction close to the terminus (Greenwood et al., 2007). They may also tell us something about thermal regime of the ice with subglacial channels indicating a warm-based ice sheet (Greenwood et al., 2007).

Eskers are straight to sinuous ridges consisting of glaciofluvial sediments (Dewald et al., 2021). They are formed englacially or subglacially in conduits or supraglacially in ice-walled tunnels in the glaciers drainage system (Forwick et al., 2016). Since they are situated at different elevations in the ice, the eskers may become superimposed on one another when the ice melts (Storrar et al., 2020). Eskers may be uniform ridges or complex dendritic networks and are usually sub-parallel to the direction of ice flow (Forwick et al., 2016). They may also follow the shape of the ice margin, and when eskers are oriented in both directions a cross-cutting pattern occurs (Storrar et al., 2020). Esker morphology are affected by several factors like, meltwater and sediment availability, topography, ice-marginal dynamics (channel abandonments, outwash heads and dead ice), and the position of formation in the ice round-crested eskers are believed to be formed subglacially, while sharp-crested esker may be formed in supraglacial channels or in level or descending terrain. Flat-topped esker are believed to have formed in ice walled canyons being deposited in standing water (Storrar et al., 2020). Modification of sharp-crested eskers into more round-crested ones, after deposition, may also occur (Storrar et al., 2020). Eskers may be single ridges or complex systems of multiple ridges (Storrar et al., 2020). (Storrar et al., 2020). So-called "beaded eskers" are formed when a water-terminating esker retreats stepwise and is deposited as subaqueous fans (Forwick et al., 2016). There may be areas of esker enlargements, that are segments up to 500 % wider than the trunk ridge (Dewald et al., 2021). They are spatially confined and reconverges downflow (Dewald et al., 2021). Esker enlargements may consist of a coherent sediment body or of complex ridge networks, with a flat topped, irregular, complex or hybrid morphology (Dewald et al., 2021). The formation of complex eskers is caused by a high sediment supply together with the response of the drainage system to a dynamic ice margin (Storrar et al., 2020). Processes in the ice margin that may control channel evolution are surges, outwash heads, dead ice, and channel abandonment (Storrar et al., 2020). Subglacial conduit choking may cause channels to diverge and minor conduits may form along the main channel if the waterflow increases (Dewald et al., 2021). Conduits may also breach on ascending slopes or form several eskers along the main esker because of an unstable position on top of a previously deposited ridge (Dewald et al., 2021). Complex esker enlargements roofs collapsing into subglacial conduits (Dewald et al., 2021). Conduit collapse is less likely if the ice margin terminated in deep water since the thickness of the ice is dependent on water depth, but if the topography causes the ice to be shallowly grounded conduit collapses is allowed (Dewald et al., 2021). Increased sediment supply or the existence of proglacial lakes may cause previously deposited ridges to be buried and flat-topped surfaces to evolve (Dewald et al., 2021). This makes the flat topped surfaces elevated over the ridge network in hybrid eskers (Dewald et al., 2021). Hybrid esker enlargements are believed to be formed by processes occurring in a deposited complex network, like sedimentation in standing waters and melt-out of ice blocks (Dewald et al., 2021). For the eskers to be preserved they need to contain a large enough amount of sediment, and surviving eskers are often formed in areas with high sediment supply (Storrar et al., 2020).

2.4. Submarine mass-transport deposits

Several mass-transport deposits can be seen on the multibeam bathymetry covering the survey area. Submarine mass-transport deposits (MTD) are found on slopes in all water depths and geological settings (Masson et al., 2006). A MTD may be recognized in the multibeam bathymetry by its headwall, failure scar and arcuate lobes (Figure 5) (Kremer et al., 2015). The headwall is a step-like escarpment often found where the slope angle increases (Kremer et al., 2015). Below the headwall the failure scar (head scar), from where the sediments have been removed, is seen above the arcuate lobes in the basin plain (Kremer et al., 2015). In the sub-bottom profiles, the MTD are often seen as wedge shaped bodies with chaotic to transparent facies and irregular upper surfaces (Sammartini et al., 2019).

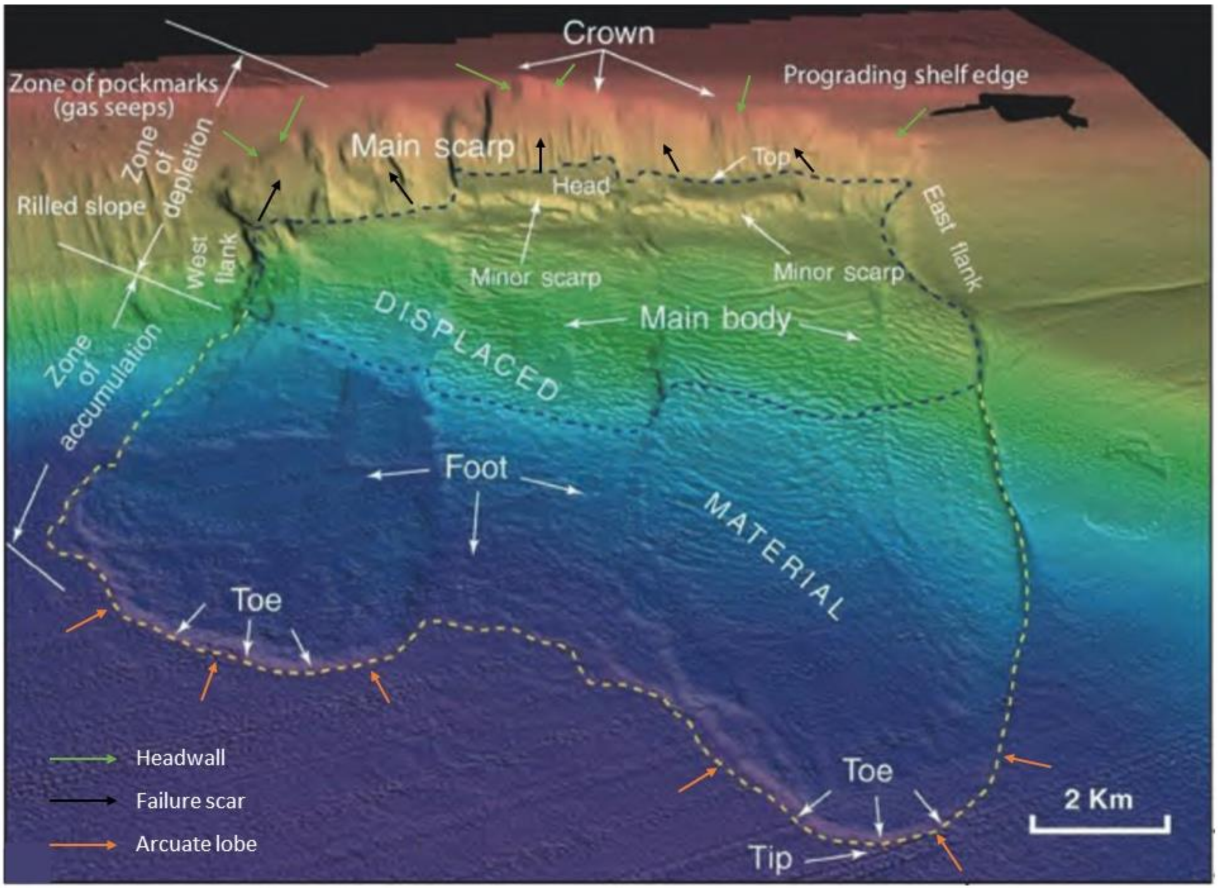

Figure 5. A mass-transport deposit in the Santa Barbara Channel, California. Figure modified from Shanmugam (2015).

Different factors make a surface more prone to mass-transport deposits. An important factor in most submarine MTDs is elevated pore pressure lowering the friction and the resistance to mass movements (Masson et al., 2006). Overpressure may be caused by rapid deposition (Masson et al., 2006), low tide (Kirby et al., 2017), or earthquake shaking (Masson et al., 2006). Excess pore pressure may also, during falling water levels in shallow areas, be caused by expanding gas bubbles in organic-rich sediments (Talling et al., 2014). If the elevated pore pressure occurs in a specific geological horizon, caused by changes in sedimentation, a weak layer is created which may contribute to a lower slope stability (Masson et al., 2006). Fine grained sediments produced by glaciers also favours MTD formation when accumulated in thick layers (Masson et al., 2006). So does rapid accumulation of sediments in submarines deltas and river fans (Masson et al., 2006) Often, external causes, like earthquakes or anthropogenic activity on the shoreline triggers the mass-transport deposit (Sammartini et al., 2019). Rapid water-level fluctuations is another possible cause, for example during tides (Hilbe and Anselmetti, 2015). Melting of the Weichselian ice sheet caused glacial isostatic adjustment to occur in Scandinavia, which led to seismic activity through reactivation of major bedrock fraction zones (Fjeldskaar et al., 2000) (Lund and Näslund, 2009). The process of glacial isostatic adjustment is active for tens of thousands of years after the melting of the ice sheet and is till occurring today (Lund and Näslund, 2009). MTDs may occur relatedly through history on a slope prone to mass-transport deposits (Masson et al., 2006).

Submarine mass-transport deposits pose a threat to humans by causing collapse of coastal areas and generating tsunamis (Masson et al., 2006). They may also destroy infrastructures both below water and onshore (Strupler et al., 2017). Tsunamis caused by MTDs often have a larger local than distal effect with a large run-up close to the MTD compared to earthquake tsunamis (Masson et al., 2006). Tsunamis in lakes and enclosed water bodies are different from tsunamis generated in the open ocean (Couston et al., 2015). In lakes the affected areas are close to the tsunami generating source, with a fast occurrence of destructive runups and waves being reflected back and forth in the enclosed area (Couston et al., 2015). If a tsunami is generated from a landslide, its wave height is depending on the volume and density of mass-moved material, water depth, slope angle, time-duration of the land slide, speed and initial acceleration of mass-moved material, coherence (meaning clay particles ability to stick together), vertical displacements and type of mass failure (Murty, 2003) (Strupler et al., 2017) (Beigt et al., 2016). Effective tsunami generating MTDs are so called rotational slides (slumps), that may cause tsunamis even whit a small vertical displacement of the material (Masson et al., 2006). A rotational slide (slump) occurs on a concave-up glide plane with a rotational movement of the masses leading to internal deformation, while a translational slide (slide) occurs on a planar glide plane as a coherent mass with no internal deformation (Shanmugam, 2015). The tsunami generating potential of a submarine MTD also depends on the Froude number with MTDs having a Froude number close to 1 being the most tsunamigenic (Glimsdal et al., 2016). The Froude number is calculated using (u) being the MTD speed and (c_0) the linear long-wave speed (Harbitz et al., 2006):

$$Fr = \frac{u}{c_0} \qquad \textit{(Eq. 1)}$$

The linear long-wave speed is calculated using (h) being the water depth and (g) the acceleration of gravity (Harbitz et al., 2006):

$$c_0 = (gh)^{1/2} \qquad \textit{(Eq. 2)}$$

MTD motion may be sub-critical (Fr<1), critical (Fr=1), or super-critical (Fr>1) with submarine mass-transport deposits often being sub-critical (Harbitz et al., 2006). There are few tsunamis generated by subaqueous MTDs reported historically compared to tsunamis caused by subaerial MTDs depositing sediments into the water (Kremer et al., 2021). A list of tsunami-generating mass-transport deposits can be seen below in table 1 and in Figure 6 the area and volume of some of the landslides are plotted. The MTDs in Lake Orsa adjacent to Lake Siljan are also listed.

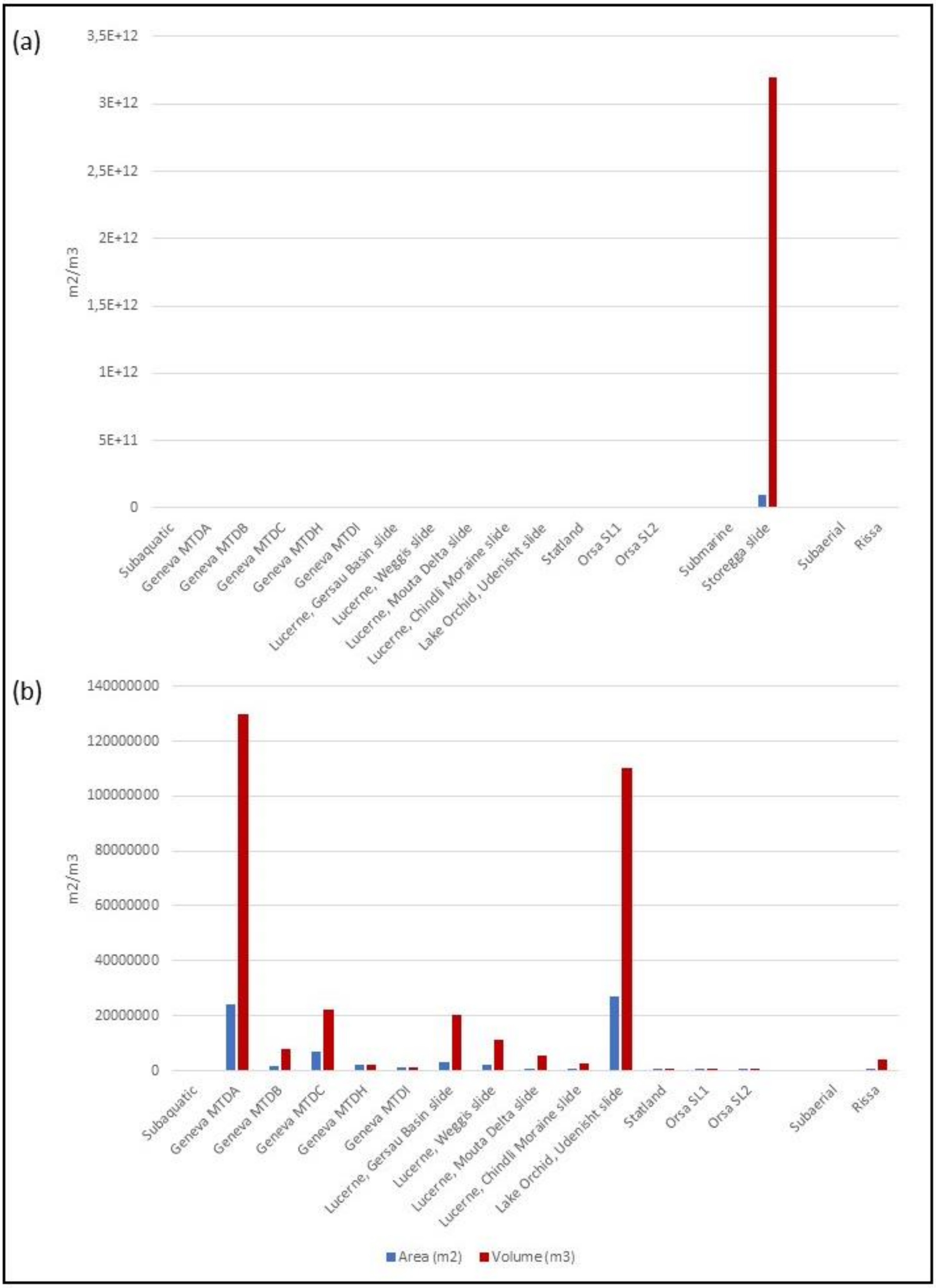

Figure 6. Comparison of area and volume of some of the mass-transport deposits in Table 1. (a) The Storegga slide is so large that the others are not seen in the plot. (b) With the Storegga slide removed the other MTD can be compared.

Table 1. Tsunami generating mass-transport deposits through history and the MTDs found in Lake Orsa adjacent to Lake Siljan.

Event	Type	Area (m^2)	Volume (m^3)	Slope (°)	Trigger	Tsunami	Run up height (m)	Max amplitude (m)	References
Vättern	Subaquatic		2.8 x 10^6	2.8 x 10^6	Earthquake	Assumed			(Jakobsson et al., 2014)
Lago Nahuel Huapi, Argentina, May 22, 1960	Subaquatic	29233		17	Valdivia earthquake, construction work	Observed		101	(Beigt et al., 2016)
Lake Tahoe, McKinney Bay, 21-12 ka	Subaquatic		12 x 10^9			Sedimentary evidence		50	(Kremer et al., 2021), (Moore et al., 2014)
Skagway Harbor, Alaska, Nov 3, 1994	Subaquatic		0.8x10^6	30-35	Failure of dock	Observed		11	(Rabinovich et al., 1999)
Kitimat arm, British Columbia, April 27, 1975	Subaquatic		~2.3x10^6		Low tide	Observed		8.2	(Kirby et al., 2016)
Lake Geneva:									(Kremer et.al., 2015)
MTDA, 3683±128 cal BP	Subaquatic	24 x 10^6	130 x 10^6		Earthquake	Modelled		12	(Kremer et.al., 2015)
MTDB 3895±225 cal BP	Subaquatic	1.5 x 10^6	8 x 10^6		Wind and storm waves, excess pore pressure, earthquake	Modelled			(Kremer et.al., 2015)
MTDC, 3683±128 cal BP	Subaquatic	7 x 10^6	22 x 10^6		Earthquake	Modelled			(Kremer et.al., 2015)
MTDE, 2185±85 cal BP	Delta collapse				Earthquake?	Modelled		1	(Kremer et.al., 2015)
MTDF, 1920±120 cal BP	Delta collapse					Modelled			(Kremer et.al., 2015)
MTDG, 1387 BP (563 AD)	Delta collapse		250 x 10^6		Massive rockfall	Described in historical records, modelled		13	(Kremer et.al., 2015)

Event	Type	Area (m^2)	Volume (m^3)	Slope (°)	Trigger	Tsunami	Run up height (m)	Max amplitude (m)	References
MTDH 1320±100 cal AD	Subaquatic	2 x 10^6	ca 2 x 10^6		High sediment input, earthquake 1322				(Kremer et.al., 2015)
MTDI 1500±100 AD	Subaquatic	1.4 x 10^6	1 x 10^6		Aigle earthquake 1584	Described in historical records, modelled			(Kremer et.al., 2015)
Udenisht slide, Lake Orchid, Makedonia/Albania	Subaquatic	27 x 10^6	0.11 x 10^9		Seismicity along an active fault	Modelled	10	5	(Lindhorst et al., 2014)
Lake Lucerne:									(Hilbe and Anselmetti, 2015)
Weggis slide, AD 1601	Subaquatic	2.3 x 10^6	11.4 x 10^6		Earthquake	Described in historical records, modelled	3-6	3	(Hilbe and Anselmetti, 2015)
Gersau Basin slide, AD 1601	Subaquatic	3.3 x 10^6	20.08 x 10^6		Earthquake	Described in historical records, modelled	>10	10	(Hilbe and Anselmetti, 2015)
Mouta Delta slide, AD 1687	Delta collapse	0.4 x 10^6	5.5 x 10^6		Spontaneous collapse		>10	6	(Hilbe and Anselmetti, 2015)
Chindli Moraine slide, AD 1601	Subaquatic	0.4 x 10^6	2,8 x 10^6	15-25	Earthquake			4	(Hilbe and Anselmetti, 2015)
Storegga slide 8120-8175 years BP	Submarine	95 x 10^9	2400-3200 x 10^9	0,3-2°	High sedimentation, gas hydrate melting, earthquake	Sedimentary evidence	20		(Bondevik, 2022)
Rissa, Norway 1978	Subaerial	25-30000 m2	5-6 x 10^6 m^3 (4 x 10^6 m^3 in Lake Botnen)		?	Observed	6.8		(Liu et al., 2021)
Askja, Iceland, July 21, 2014	Subaerial		20 x 10^6			Observed, well documented	80		(Løvholt et al., 2020)
Waikari river, New Zealand, 1931	Subaerial		1.7 x 10^6		Hawke´s Bay earthquake	Historical documents, sedimentary deposits	20?	15	(Kremer et al., 2021)

Event	Type	Area (m^2)	Volume (m^3)	Slope (°)	Trigger	Tsunami	Run up height (m)	Max amplitude (m)	References
Statland, Norway, Jan 29, 2014	Subaquatic	21000	350-400 000		Failure of soft marine (deltaic) sediments	Observed, modelled	8.2		(Glimsdal et al., 2016)
Lituya Bay, Alaska, July 10, 1958	Subaerial		30.6 x 10^6		Earthquake	Observed, modelled	524	162	(Fritz et al., 2009)
Trondheim, Norway, april 23, 1888	Subaquatic		1.45 x 10^6			Observed, modelled	1-7	1-2	(Glimsdal et al., 2013)
Lake Sils, Switzerland, 474-770 cal AD	Delta collapse		6.5 x 10^6			Modelled, sedimentary records	4	5	(Kremer et al., 2021)
Orkdalsfjorden, Norway, May 2, 1930	Subaquatic		18.5 x 10^6		Human activity, low tide, steep slopes	Observed	15		Jean-Sebastien L'Heureux
Lake Tekapo, New Zealand	Subaquatic		<0.05 x 10^6			Modelled			(Kremer et al., 2021)
Lake Orsa:									(Ståhl, 2019)
Lake Orsa SL1	Subaquatic	99539	336884	10					(Ståhl, 2019)
Lake Orsa SL2	Subaquatic	179218	622336	25					(Ståhl, 2019)
Lake Orsa SL3	Subaquatic	153069		30					(Ståhl, 2019)
Lake Orsa SL4	Subaquatic	73517		17					(Ståhl, 2019)
Lake Orsa SL5	Subaquatic			22					(Ståhl, 2019)

In 1960 vibrations from the reconstruction of a pier together with the Valdivia earthquake are believed to have caused a tsunami generating MTD in in Lago Nahuel Huapi, a proglacial lake with sediments consisting of glacienic, fluvial and pyroclastic materials, located in Argentina (Beigt et al., 2016). The tsunami generated by the MTD, with a volume of ~29 x 10^3 m^2, hit Puerto San Carlos, killed two people and caused the collapse of a pier (Beigt et al., 2016). A smaller subaqueous MTD occurred in Skagway Harbour, Alaska in 1994 (Blais-Stevens et al., 2006). This MTD that was caused by the collapse of a dock, because of overloading of slope materials, generated a tsunami that killed one person and caused damage for millions of dollars (Rabinovich et al., 1999) (Kulikov et al., 1996). The tsunami had according to eyewitnesses a wave height of 5-6 m in the inlet and 9-11 m at the shoreline (Kulikov et al., 1996).The smallest tsunami generating MTD on the list occurred in Statland, middle- Norway in 2014 with a volume of 350-400 000 m^3 and a maximum run-up height of 10 m (Glimsdal et al., 2016). No people got severely injured or killed by the tsunami but it caused damage to the Statland village with the destruction of 12 boathouses, a dock, and several boats and damage of an industrial building and a road (Glimsdal et al., 2016). In Sweden a mass-transport deposit scar found in Lake Vättern is large enough to potentially have caused a tsunami (Jakobsson et al., 2014).

3. Methods

3.1. Marine geophysical mapping

The geophysical mapping methods applied in Lake Siljan to acquire the data used in this study are based on the echo sounding method. The following brief basic description of the echo-sounding method is mainly taken from Jakobsson et al. (2016b). An echo sounder transmits a sound pulse and measures the time it takes for the pulse to return to a receiver. The time it takes for the sound pulse to travel through the water column and back, after being reflected by the seafloor or other objects, is called the two-way travel time (*TWT*). With knowledge of the speed of sound (v) in the water column, the TWT can be used for calculating depth (D) using:

$$D = v \times \frac{TWT}{2} \quad \text{(Eq. 3)}$$

The sound speed may vary through the water column because of differences in pressure, temperature, and salinity. An accurate sound velocity profile (SVP) is therefore important to collect in order to convert travel time to depth. The sound velocity can be measured through the water column or be calculated from measurements of pressure, temperature, and salinity. An incorrect SVP may lead to artifacts caused by refractions, where the sound wave is being bent at the interface of two layers with different sound speed. Artifacts are false features that may create problems when interpreting multibeam images caused by geometric, acoustic, or processing phenomena. Refractions causes distortion of the seabed in a curved upward (smiley) or a curved downward (frowny) manner (Mohammadloo et al., 2019). The curved upward distortion occurs when a sound pulse travels from a layer with lower sound speed to a layer with higher sound speed, while the curved downward distortion occurs when the pulse travels from a layer with higher sound speed to a layer where the speed of sound is lower (Jakobsson et al., 2016b).

A multibeam echo sounder (MBES) was used in the Siljan survey in 2018 by Jakobsson et al. (personal communication) to bathymetrically map the lake floor (see further details below). A MBES transmits several sound waves in a wide fan perpendicular to the ship track with receiving transducers rotated 90° compared to the transmitters (Jakobsson et al., 2016a). This configuration is called a Mills T or Mills cross and gives acoustic footprints that is a cross product of the transmitted and received beam (Jakobsson et al., 2016a). The wide swath makes the MBESs an effective tool for surveying large areas (Mohammadloo et al., 2019). A swath of high-resolution depth measurements is received and high-resolution digital elevation models representing the bathymetry can be created. MBESs also measures the acoustic backscatter, which is the strength of the returned signal that depends on the angle of incidence, the roughness of the seafloor, and the acoustic characteristic impedance contrast (Tang et al., 2005) (Jakobsson et al., 2016a). Acoustic characteristic impedance is the compressional sound speed times the bulk density of material the sound propagates through. Backscatter images and mosaics can be created from the acquired MBES data that provide information on the geological properties of the sea- or lake floors. A backscatter mosaic is essentially a georeferenced image showing the strength of the acoustic backscatter in different regions permitting a geological interpretation (Schimel et al., 2018).

The second acoustic mapping instrument used during the Siljan 2018 survey was a sub-bottom profiler (SBP), which provides information of the uppermost sediment stratigraphy (Jakobsson et al., 2016a). Higher output energy levels and lower frequencies of the applied sound pulses compared to a MBES, imply that the transmitted signals of a SBP penetrates the seabed (Jakobsson et al., 2016a). A profile image of the reflections, occurring where there are impedance contrasts within the sediment stratigraphy, is created for interpretations (Jakobsson et al., 2016a).

Geophysical mapping of an ~18.5 km^2 large survey area in Lake Siljan was done in July 2020 with Stockholm University's survey boat RV *Skidbladner* (Jakobsson personal communication). This boat was equipped with a bow-mounted Kongsberg Maritime EM2040 0.7° x 0.7°, 200-400 kHz, multibeam echo-sounder and a Kongsberg EA640 single beam echo-sounder using an Airmar Air15-17 (center frequency ~16 kHz) transducer installed in a device towed behind the boat. The relative low frequency of the Air15-17 transducer implies that the echosounder could be operated as a sub-bottom profiler. During the acquisition of the multibeam bathymetry, a frequency of 400 kHz was used. A Valeport mini SVP was used to acquire sound velocity profiles for calibration of the multibeam. Sub-bottom profiles were collected with the Kongsberg EA640 operating in chirp-mode using a bandwidth between 13-17 kHz and a pulse length of 1.024 ms. Positioning and altitude information to the multibeam acquisition was provided by a Seapath 320+ with a MR5+ motion sensor installed in RV *Skidbladner*. RTK (Real Time Kinematic) corrections were applied to the positioning data using SWEPOS stations connected through the internet. Tables showing the water levels are found in Appendix A. The positioning of the EA640 was done using a separate Hemisphere V100 GPS mounted directly on the towed vehicle with the transducer. This GPS was corrected using SBAS "Space Based Augmentation System".

3.1. Geophysical data processing

3.1.1. Multibeam data processing

Processing of Multibeam data was performed in the software Qimera 2.4.2 from QPS. Raw data were received in the .all format and imported into Qimera. The project coordinate system used was SWEREF99 15 00 + RH2000 height (EPSG:5848), and the geoid model SWEN17_RH2000 was applied to reference the depths to the RH2000 height system. A static offset of +161.170 m was set to adjust for Lake Siljans position above sea level. A dynamic surface was created with a cell size of 1.25 m and CUBE editing enabled. In the CUBE settings the configuration was set to shallow. The CUBE algorithm is able to handle both stochastic and systematic errors and creates a continuous surface of estimated "true" depth (Calder and Mayer, 2003). For each sounding, a vertical and horizontal error is calculated, and the information may be used in more than one estimation node. To correct for systematic bias regarding roll and pitch of the boat and for heading offset and position latency a patch test was implemented. Refractions caused by variations in the sound speed through the water column were evident in some of the acquired multibeam data. In an attempt to reduce these, the TU

Delft Sound Speed inversion algorithm implemented in Qimera was used. It uses the overlap between adjacent swaths and minimizes the difference in depth between them (Mohammadloo et al., 2019). A constant harmonic sound speed is assumed (Mohammadloo et al., 2019) and the depth differences between adjacent overlapping swaths due to refractions are minimized by corrections of the harmonic sound speed, for chosen pings and their neighbours, to find the best-fit solution (Beaudoin et al., 2018). Following the above procedures, the data was edited manually using point editing in the 3D editor to remove outliers (Figure 7).

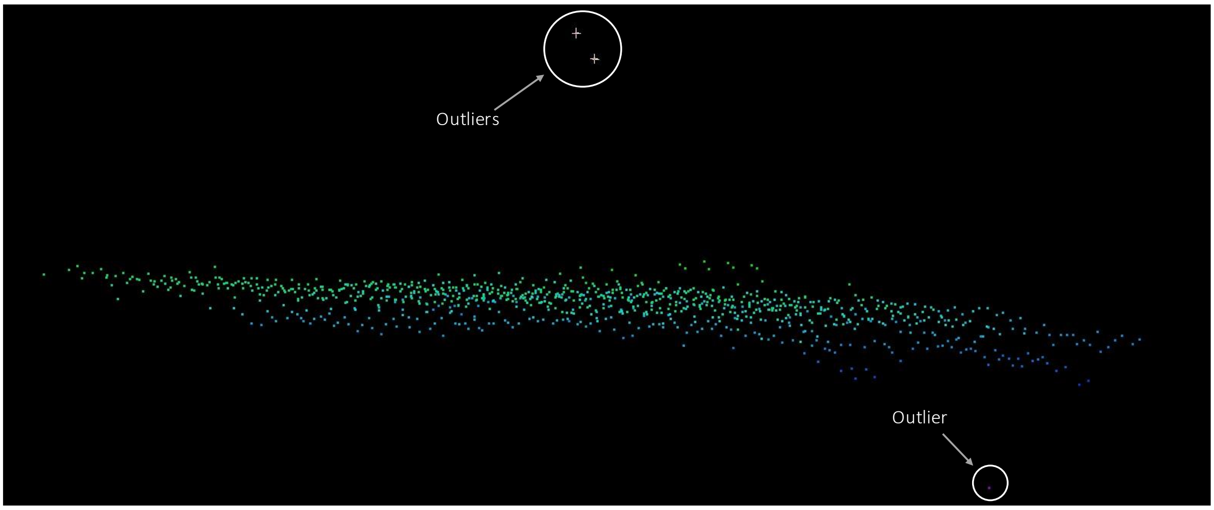

Figure 7. *Outliers being removed in the 3D editor.*

Wobbly outer beams (Figure 8) were removed in Qimera by an “Outer beams filter”, which rejects soundings outside of a specific beam angle range. The filter was here set to reject soundings outside of -55.0° respective 55.0° from nadir. Spline filters were used to reject soundings in areas with particularly noisy data. These filters create a smooth surface using the data, and then reject points that falls at a user set distance from the surface. The distance is set as a percentage of the depth. The CUBE surface had some small holes which were interpolated in Qimera using the build in function, with minimum neighbours set to 3, iterations to 1 and Interpolation type to average.

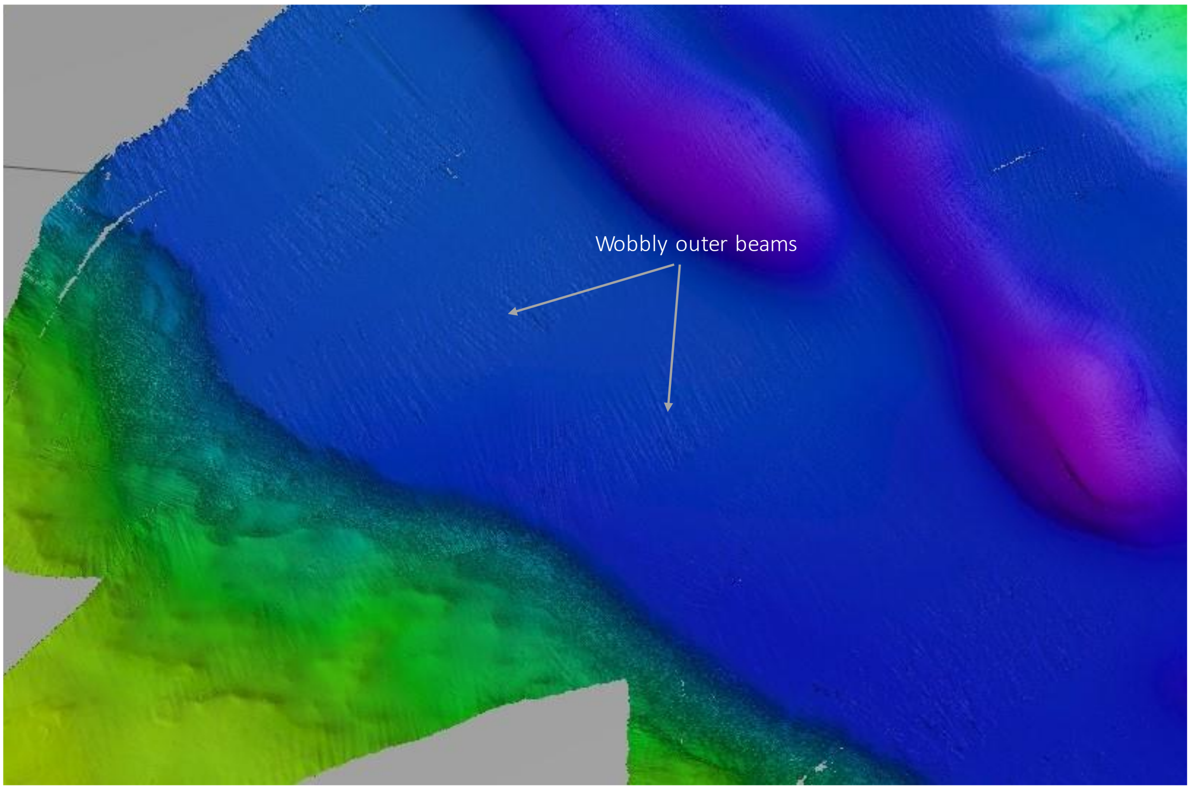

Figure 8. *Wobbly outer beams seen in the multibeam bathymetry. These are commonly due to poor sound-velocity control.*

3.1.2. Backscatter

The FMGeocoder Toolbox (FMGT) was used to create maps of backscatter mosaics, statistics, and Angular Range Analysis (ARA). FMGT implements the Geocoder algorithm, which creates a backscatter map by radiometrically and geometrically correcting the backscatter times series measurements before geocoding the values in a projection coordinate system (Fonseca and Calder, 2005). Intensity values are then interpolated to resemble the acquisition geometry (Fonseca and Calder, 2005). Geocoder also applies an anti-aliasing algorithm for better resolution and a blending algorithm to minimize seams between overlapping swaths (Fonseca and Calder, 2005). Along and across track slopes are taken into account and corrections are applied to reduce angular effects on the backscatter (Fonseca and Calder, 2005).

The Angular Range Analysis (ARA) produces estimates of seafloor properties like acoustic impedance, roughness, and mean grain size (Fonseca et al., 2009). An indication of the seafloor material is found by combining the backscatter strength and the grazing angle information, both measured by the multibeam sonar, to get the backscatter angular response (Fonseca and Mayer, 2007).

A dynamic surface with a grid-cell size of 1.25 m was imported from Qimera into FMGT as a reference grid in the form of a geotiff. Mosaic tiles were created with a size of 2048x2048 pixels, which gave 34 tiles, and a first mosaic, statistics and ARA were made with the resolution of 0.5 m. Survey lines that caused artifacts were removed and a beam-pattern correction was implemented. Since backscatter levels differed between different survey lines a Cascading Backscatter Normalization was done. Six lines was chosen as reference lines. This process left the surface with only a few lines where the backscatter needed to be adjusted manually by using the Line Backscatter Adjustment tool (Figure 9).

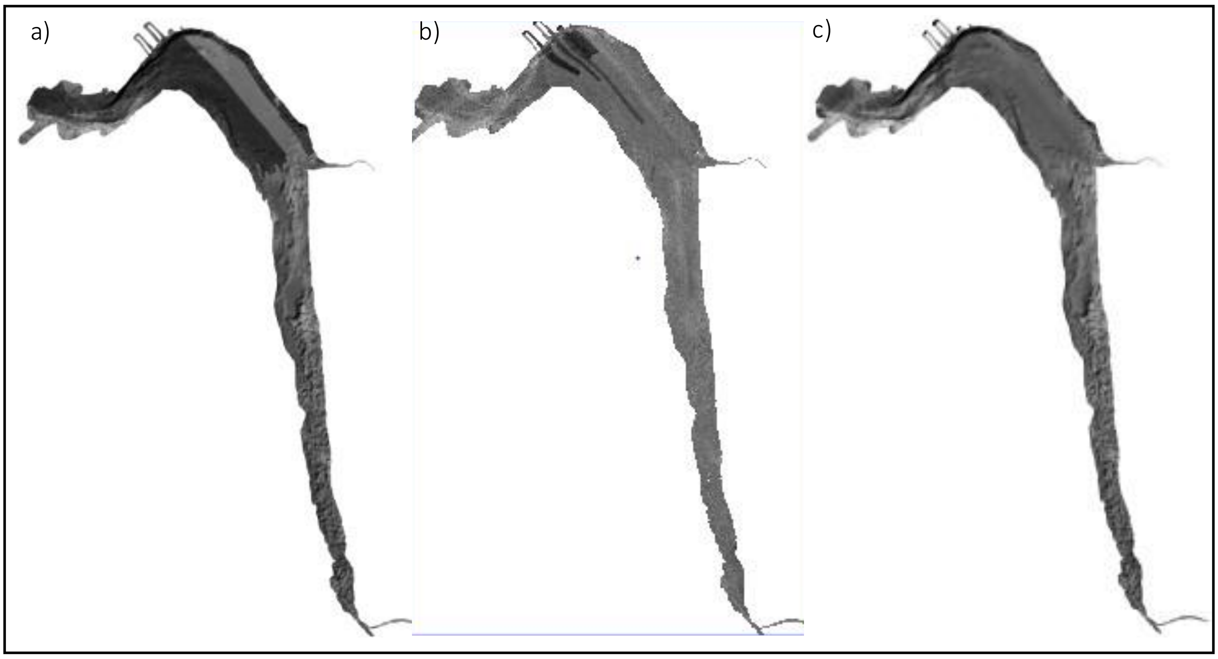

Figure 9. a) The backscatter map before the Cascading Backscatter Normalization. b) The backscatter map after the Cascading Backscatter Normalization. c) The backscatter map after manual adjustments with the Line Backscatter Adjustment tool.

New tiles were created with the size of 2048x2048 pixels and new mosaic, statistics, and ARA with 0.5 m resolution. Over the area of the largest mass-transport deposit a mosaic and ARA with resolution of 0.05 m was created for better detail. The created mosaics were imported to QGIS as geotiff files, where they were multiplied with a hillshaded version of the dynamic surface created in Qimera for better visualisation. A phyton program was created (Appendix B) that used the ϕ values from the ARA to calculate grainsizes in mm. An .xyz file containing the ϕ values was created in FMGT and imported to the Phyton program where the grainsize was calculated in mm. The values were then output into a new .xyz file that was used to create a map in QGIS.

3.1.3. Sub-bottom

The software SonarWiz 7 was used for processing of sub-bottom profiles. A new project was created with the coordinate system WGS84/UTM zone 33N, a water column sound velocity of 1450 m/s and sediment sound velocity 1600 m/s. The bathymetry was exported from QGIS as a geotiff and imported to SonarWiz as a grid with a cell-size of 1.25 m. A grid, with a cell -size of 1.25 m, clipped in QGIS to cover only the area of the largest MTD was also imported to SonarWiz to be used for volume calculations (Figure 11). The bottom was tracked in the sub-bottom profiles and converted to a bottom reflector that permits vertical datum adjustment so that the profiles can be aligned with the bathymetry (Jakobsson et al., 2021). A set of selected prominent reflectors were digitized which made it possible to compute the thickness of different stratigraphic units. In the sub-bottom profiles covering the largest MTD the bottom of the slide masses was interpreted and digitized as well as the position of the lake floor before the occurrence of the slide. Grids were interpolated for the bottom of the slide masses and the interpreted lake floor to be used in volume calculations (Figure 10).

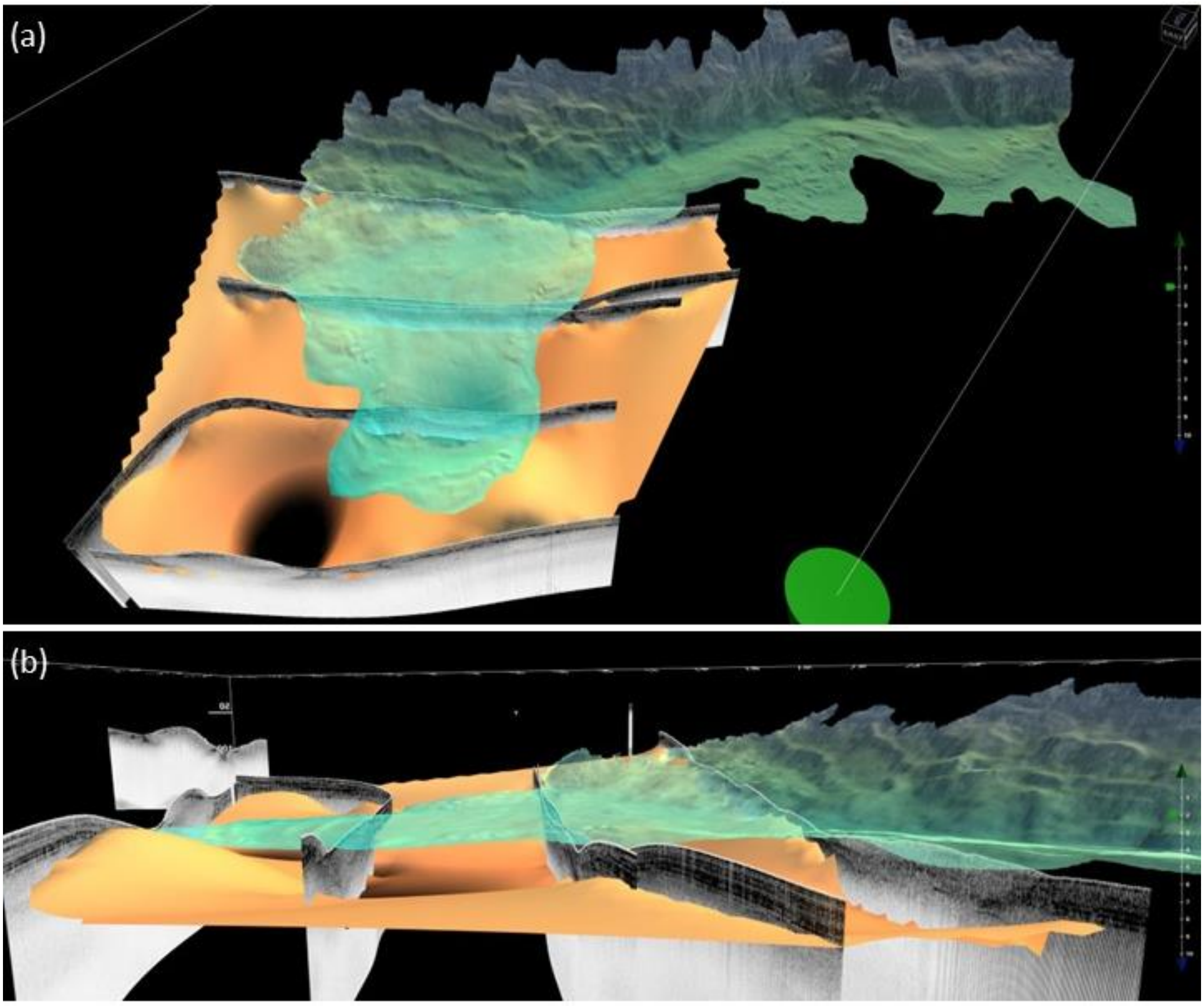

Figure 10. (a) Sub bottom profiles together with the interpolated surface for the bottom of the disturbed masses (orange) and the grid covering the area of the largest MTD (bluish green). (b) The same sub bottom profiles and surfaces seen from the side. The figures were created in the 3d viewer in SonarWiz, z=2.

3.2. Characterization of landforms

The dynamic surface was imported to QGIS and Fledermaus for landform characterization. Most of the work was performed in QGIS, but Fledermaus was used in addition to better visualise the landforms in 3D. Approximate measurements of length, width, height/depth, and areas were taken of visible parts of the landforms. To make sure that the derived dimensions of the landforms were representable, several different measurement-methods were used and compared. Contours, with a distance of one meter in between, were created to help visualising the landforms. Layers in QGIS, showing the slope and aspect, and slope contours were also generated to help with the interpretation (Figure 11). A multi-scale relief model (MSRM) and local dominance layer was created in the Relief visualisation toolbox (RVT). Both the multi-scale relief model and local dominance technique helps with the visual interpretation of landforms. The MSRM creates pyramids and uses differences in pyramid levels to extract landforms while the local dominance enhances very subtle features by showing how dominant an observer situated on a pixel would be to the area around it (Kokalj et al., 2019) (Orengo and Petrie, 2018). The RVT Multi directions hillshade tool was used to avoid azimuth biasing, which can make the same landform appear differently seen in different solar illumination directions (Smith and Wise, 2007). Fledermaus was used to get a 3D view of objects when their shape was hard to distinguish in QGIS.

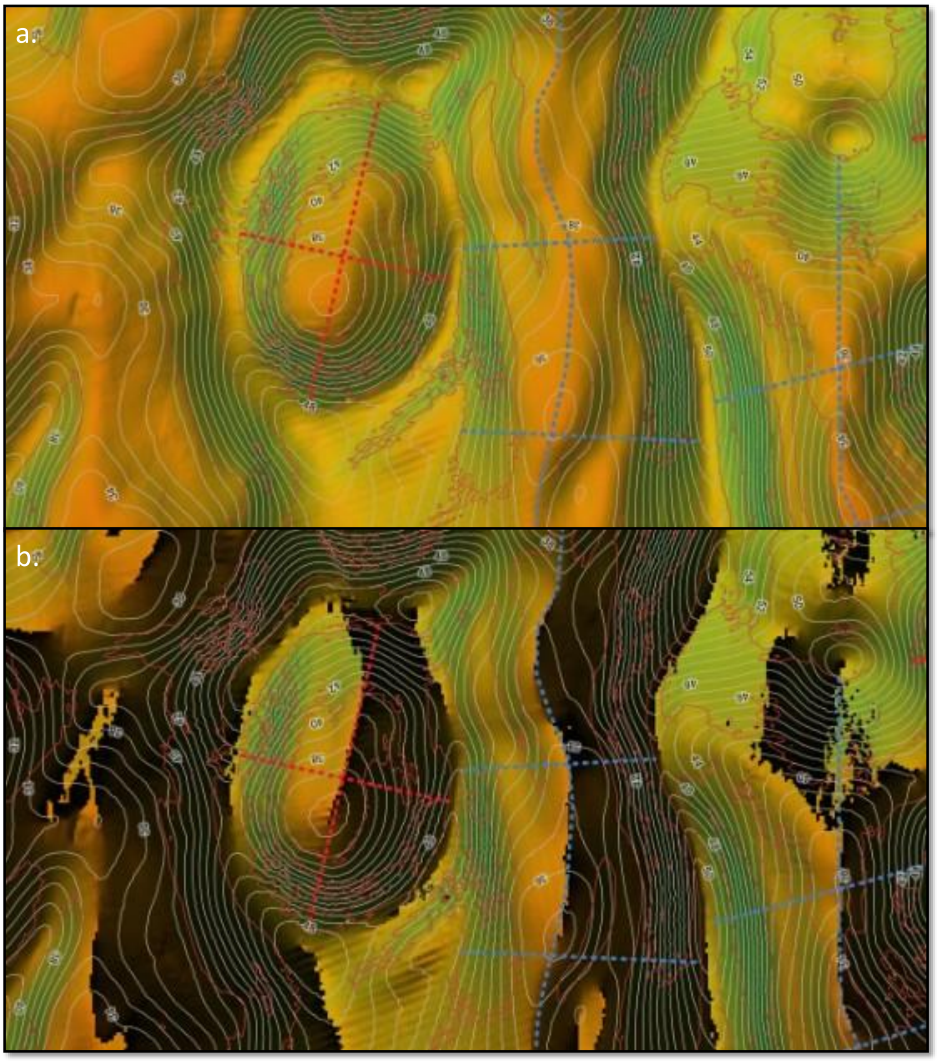

Figure 11. a) Depth contours (white), slope contours (pink) and a layer showing the slope coloured from red to green helped with the visualisation of the shapes of the landforms. b) A layer showing the aspect is added, here coloured from grey to black, to further help with the visualisation.

3.3. Volume calculations

Volumes were calculated both in SonarWiz and QGIS for the disturbed sediments seen in the sub-bottom profiles. Volume calculations in SonarWiz were executed as follows:

1. The sub-bottom profiles were interpreted and the base of the disturbed sediments and the assumed location of the lake floor before the occurrence of the MTD was digitized.
2. A grid representing the base of the disturbed sediments was created by interpolation using a grid cell-size of 10 m and the Natural Neighbour gridding algorithm.
3. A grid representing the assumed location of the lake floor before the occurrence of the MTD was created by interpolation using a grid cell-size of 10 m and the Natural Neighbour gridding algorithm.
4. The bathymetric grid from Qimera was clipped in QGIS to cover only the area of the mass-transport deposit and imported to SonarWiz.
5. The grid covering the area of the MTD was compared to the disturbed sediments interpreted in the sub-bottom profiles and corrections of the grid were made in QGIS until the area matched the sediments.

6. Volume calculations were made between the grid covering the area of the MTD and the grid representing the base of the disturbed sediments.
7. Volume calculations were made between the grid covering the area of the MTD and the grid representing the assumed location of the lake floor before the occurrence of the MTD.

Both grids created in SonarWiz where then imported as geotiffs to QGIS where the same calculations were done using the volume calculation tool.

Since the sub-bottom profiles did not cover the whole MTD the size of the headscar was used for calculations of the volume of removed sediments in QGIS. An interpolation of the lake floor, as it was situated before the MTD occurred, was made in QGIS and this surface was used, together with the bathymetry and a polygon covering the area of the mass-transport deposit, to calculate the volume with the volume calculation tool. Points with interpreted pre-MTD depths were created to be used in the interpolation. This was done in two different ways. For the first interpretation the thickness of the sediments in the headwall was interpreted in both QGIS and Fledermaus with the interpretations done in Fledermaus probably being more accurate since the headwall could be more clearly seen in the 3D view. The resulting values were used together with the thickness of the sediments above the head scar seen in the sub-bottom profiles to estimate the depth of the lake floor before the slide. For the second interpretation, depth contours were used to interpret the depth of the pre-slide lake floor. Contours with a distance of 1 and 0.5 meter in between were created in QGIS and a line layer was created where new contours representing the depth of the lake floor before the occurrence of the mass-transport deposit were manually drawn (Figure 12). To be able to create more accurate contours, a new dynamic surface with a resolution of 0.5 m was created in Qimera. The new contours followed the shape of the contours surrounding the head scar. Points to be used in the interpolation were then crated from, and given the depths of, the interpreted depth contours.

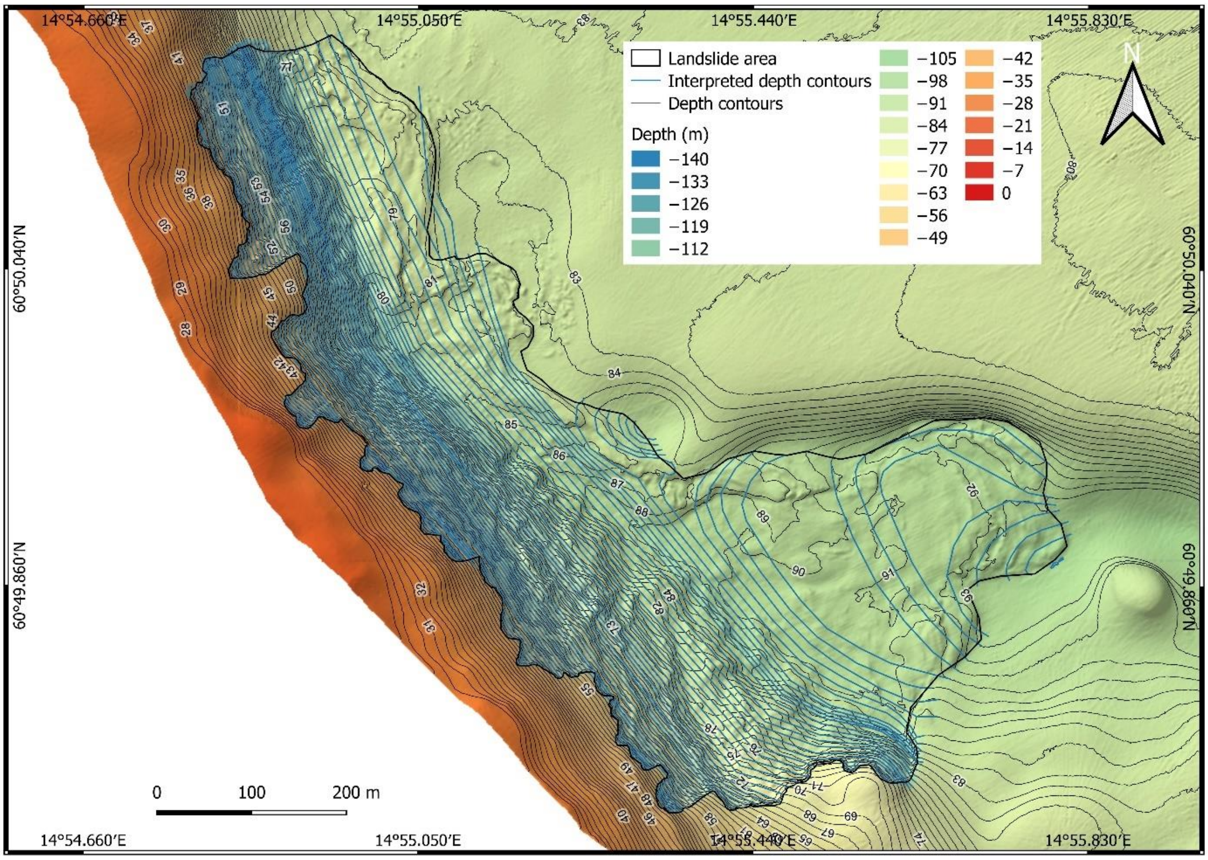

Figure 12. The depth contours in blue were manually created to represent the pre-slide lake floor.

The GRASS-v.surf.rst tool was used in QGIS to interpolate a surface from the manually created contours. While executing the interpolation using the depth contour values a small problem occurred causing a wavy surface (Figure 13). This was corrected for with the tension and smoothing parameters until a sufficient result was achieved (Figure 13). The tension parameter was then set to 20, the smoothing parameter set to 3 and the grid size to 1 m. The interpolated surface was exported as a geotiff and imported into Fledermaus for comparison in 3D with the dynamic surface. Volume calculations were then executed using the volume calculation tool.

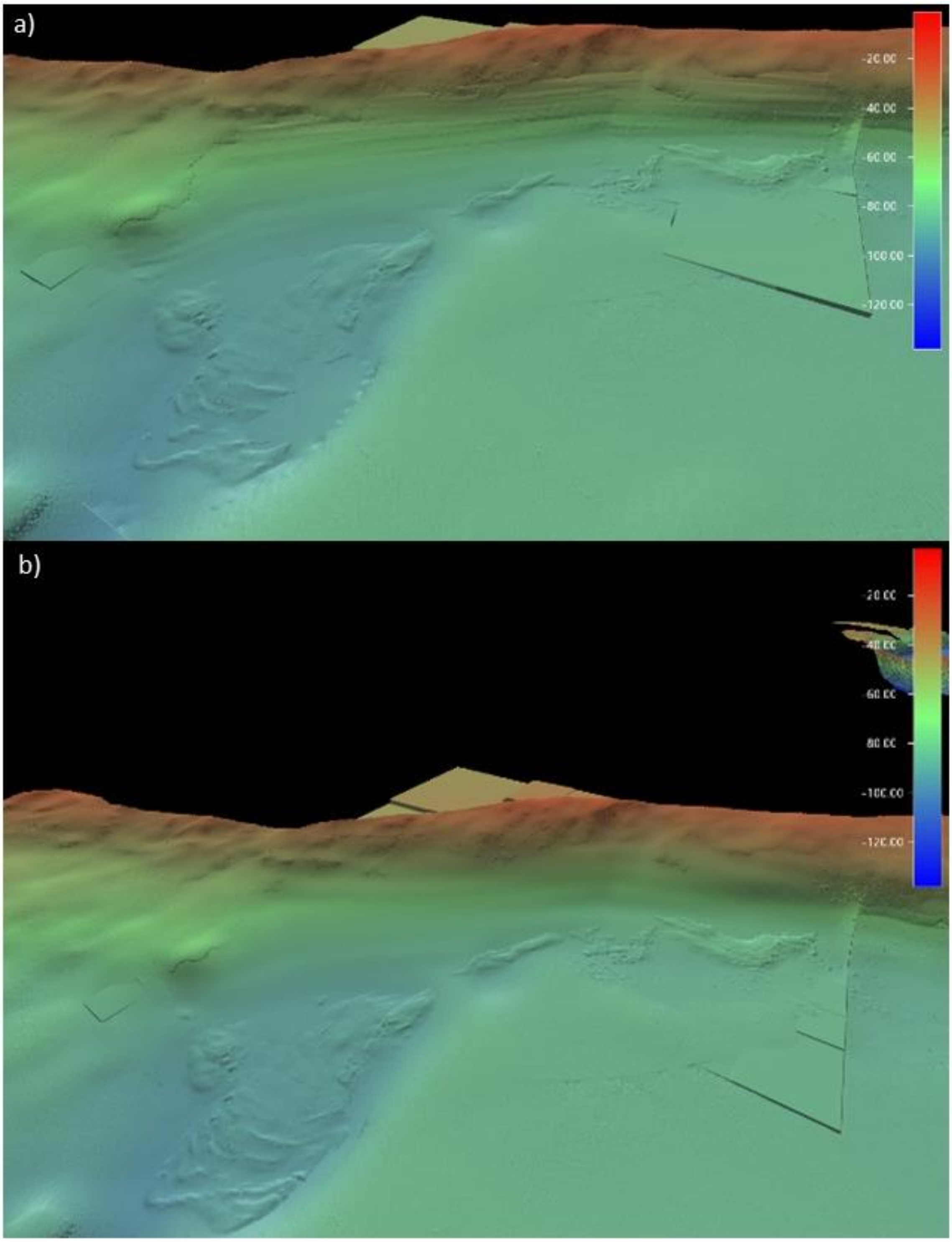

Figure 13. *(a) a wavy pattern is seen in the interpolated surface. (b) the result after the tension and smoothing parameters had been used to minimize the wavy pattern as much as possible.*

4. Result

4.1. Multibeam bathymetry and backscatter

The survey area follows the shape of a large sinuous channel formed in southern Siljan with steep sides and a smooth bottom surface in the north and a more complex bathymetry in the south (Figures 14 and 16). The surveyed area is approximately 18.5 km^2 with a maximum water depth of 138.3 m, a minimum water depth of 0.8 m, and a mean water depth of 65.7 m. The channel is deeper and wider in the north while both depth and width decreases while moving south through Österviken Bay (Figure 15). This channel will through this study be referred to as the main channel.

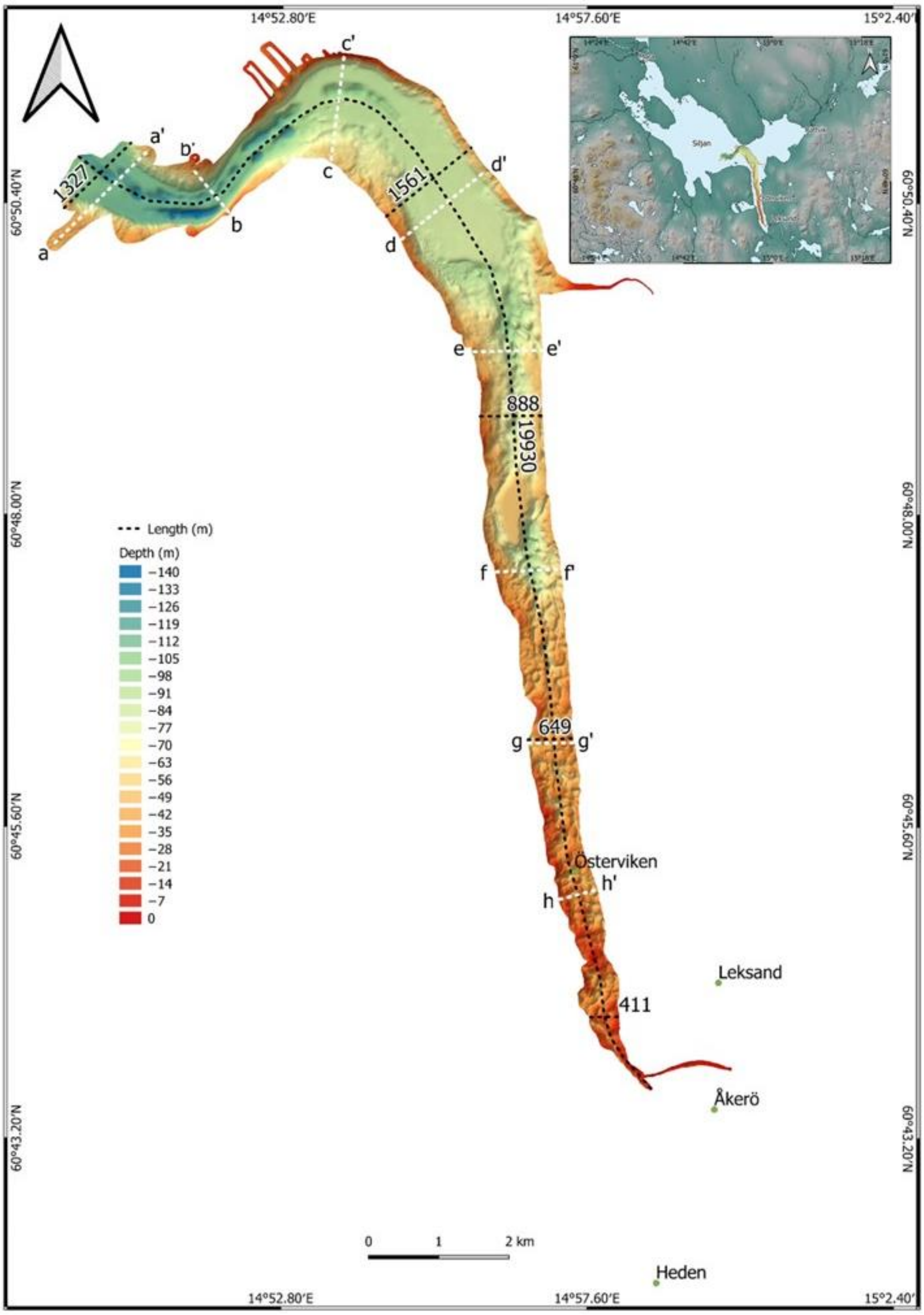

Figure 14. Multibeam bathymetry from the survey area that follows the shape of a large channel with steep sides and a smooth bottom in the north and a more complex, hummocky area in the south. Black, dotted lines show length and width measurements of the surveyed area while the white, dotted lines show the positions of the profiles seen in Figure 15.

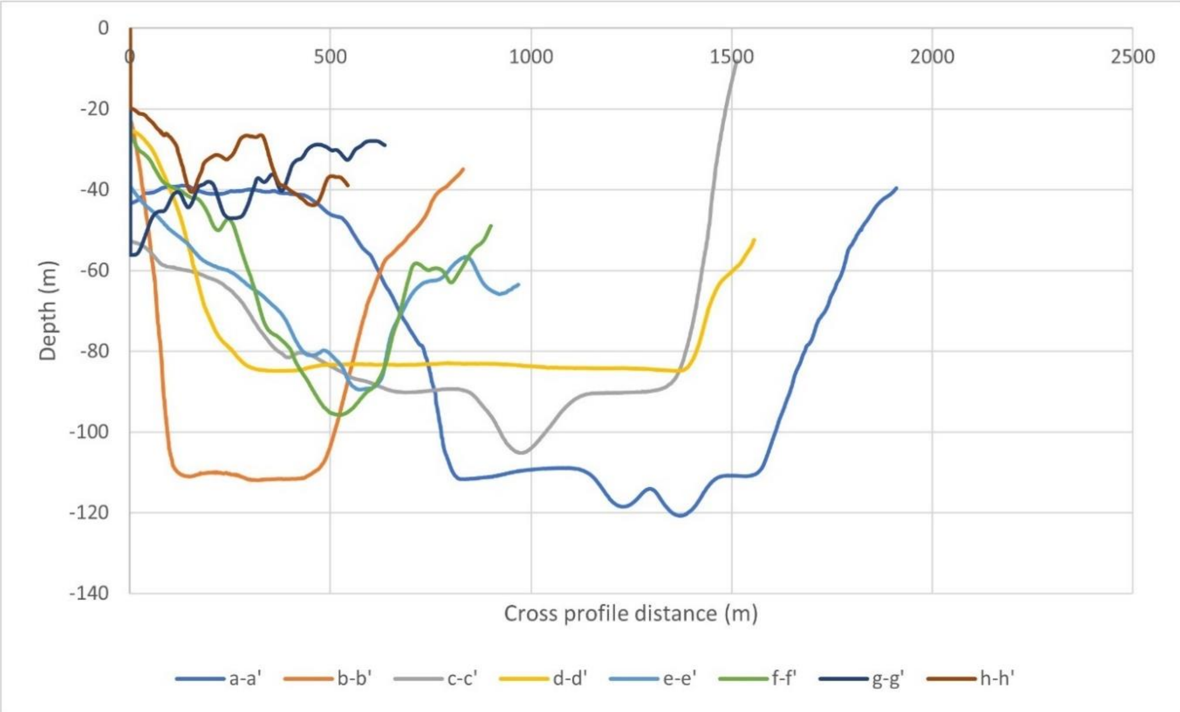

Figure 15. Cross profiles of the survey area show differences in width, depth, and shape of the lake floor. The positions of the profiles are shown with white, dotted lines in Figure 14.

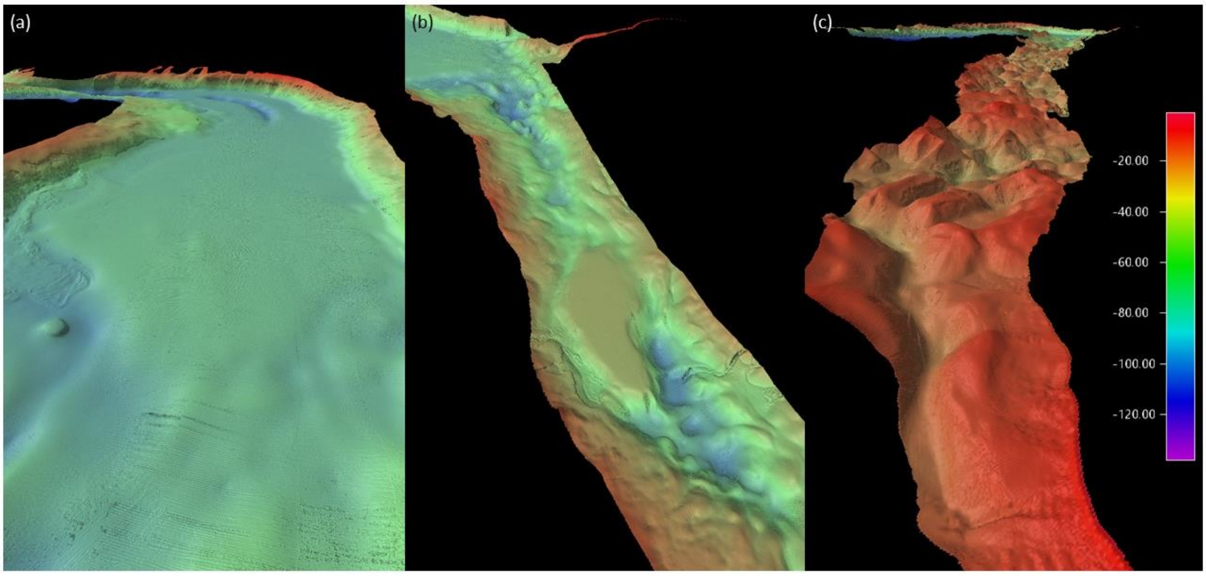

Figure 16. The multibeam bathymetry shows a relatively smooth lake floor in in the north (a) and a rather complex bathymetry moving south through Österviken Bay (b and c).

The backscatter mosaic shows low backscatter strengths in most of the survey area (Figure 17). Higher backscatter can be seen in the north-eastern part of the area and in some places around the edges, on the slopes of the channel. The backscatter strength is generally higher in parts of the Österviken Bay area with more complex bottom morphology. The highest backscatter values are found on the slopes of the channel in the north-east. The ARA-analysis shows a similar pattern as the backscatter mosaic with coarser grainsizes in the areas with higher backscatter values (Figure 18). In the northern part of the survey area coarse grainsizes are mostly observed on the slopes, while finer sediments appears to cover the flatter lake floor. In the narrow part leading in to Österviken Bay, an irregular pattern with both coarser and finer grainsizes is seen.

Figure 17. *Backscatter map of the entire surveyed area showing mostly low backscatter strenghts.*

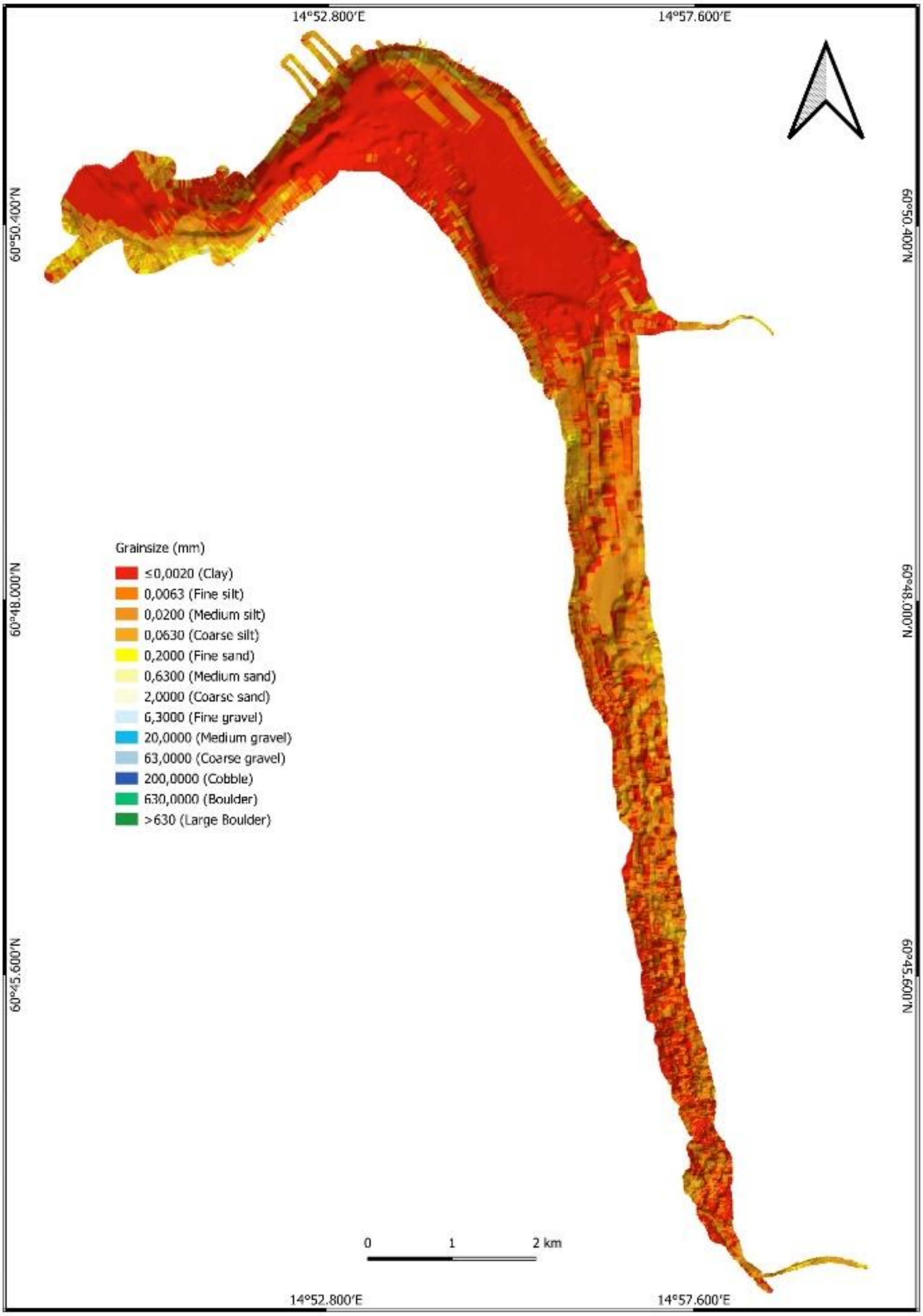

Figure 18. *Grainsize map of the entire survey area showing estimated grainsizes in mm based on the ARA-analysis of backscatter.*

In the north-western part of the survey area several smaller well pronounced channels are found in the otherwise smooth surface (Figure 19). They are following the shape of the large sinuous, main channel and there are two channels extending parallel to each other in some parts of the area. The lake seafloor surrounding the channels is between 88 m deep in the east and 112 m deep in the west. The lengths of the channels are varying with the shortest one being ~236 m and the longest ~1540 m. The variation in width is comparatively small with a mean width of about 190 m. The deepest part of the channels is around 36 m below the lake floor. The total length of the channelised area is ~5770 meters.

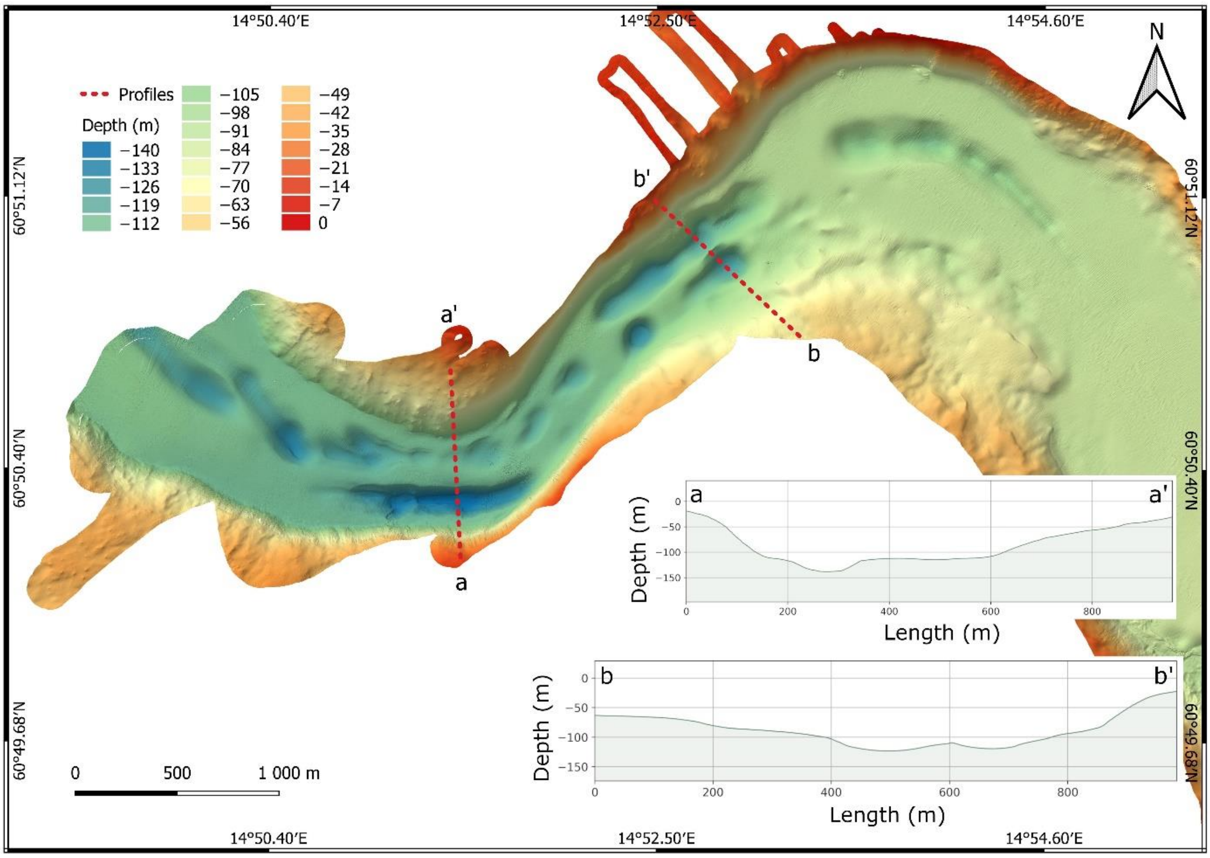

Figure 19. The north-western part of the survey area where the smaller channels can be seen.

The grainsizes calculated from the ARA-analysis in this area suggest that the bottom sediment of the main channel is mostly comprised of clay-sized particles (Figure 20). Coarser grainsizes (silt and sand) is found on the slopes forming the sides of the main channel. The smaller channels do not seem to have affected the grainsize distribution on the lake floor.

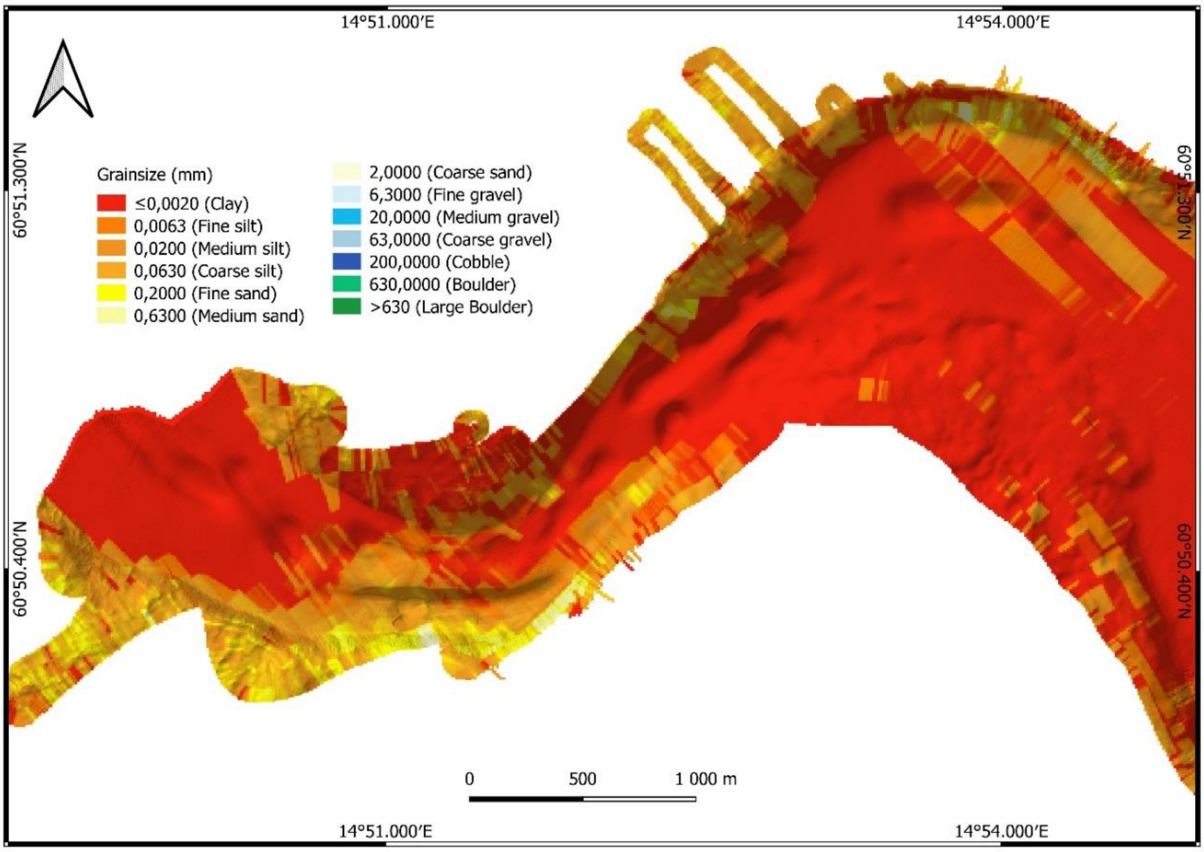

Figure 20. *Grainsize map of the north-western part of the survey area showing grainsizes in mm inferred from the ARA-analysis. The smaller channels found on the bottom of the main channel do not appear to have a different grain size distribution than the surrounding lake floor.*

A comparatively smooth, gently sloping surface is located in the northeast of the survey area (Figure 21). It is ~4 km long and as wide as the channel. This flat inclined section ends with a sharp edge to the south (Figure 21). The lake floor has a depth of ~94 m in the northern parts and ~80 m in the south. At the edge, which is very steep in some places and more irregular in others, the elevation drops with, at the most, approximately 15-20 meters.

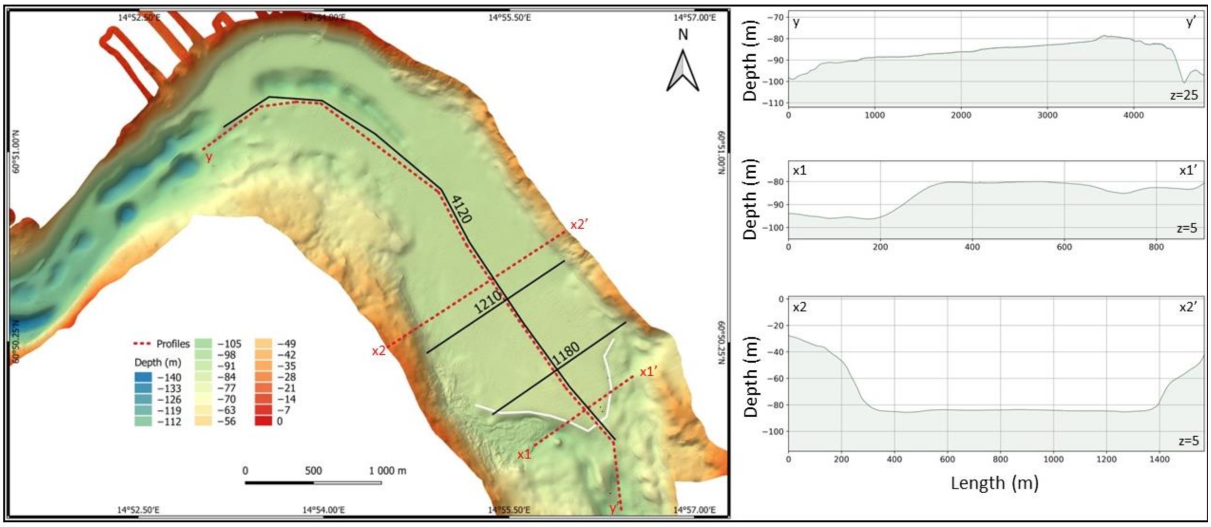

Figure 21. *The smooth surface seen in the north of the survey area. Measurements of length and width in meters are seen in black and the positions of the profiles are shown with dotted red lines. The edge is marked with a white line.*

Most of this smooth lake floor is covered by clay sized particles according to the ARA-analysis, except for an area in the northern and north-eastern parts where silt and sand sized particles occur (Figure 22). The result appears also to be affected by the backscatter calibration done by the ARA analysis. Silt and sand are also found along the surrounding slopes.

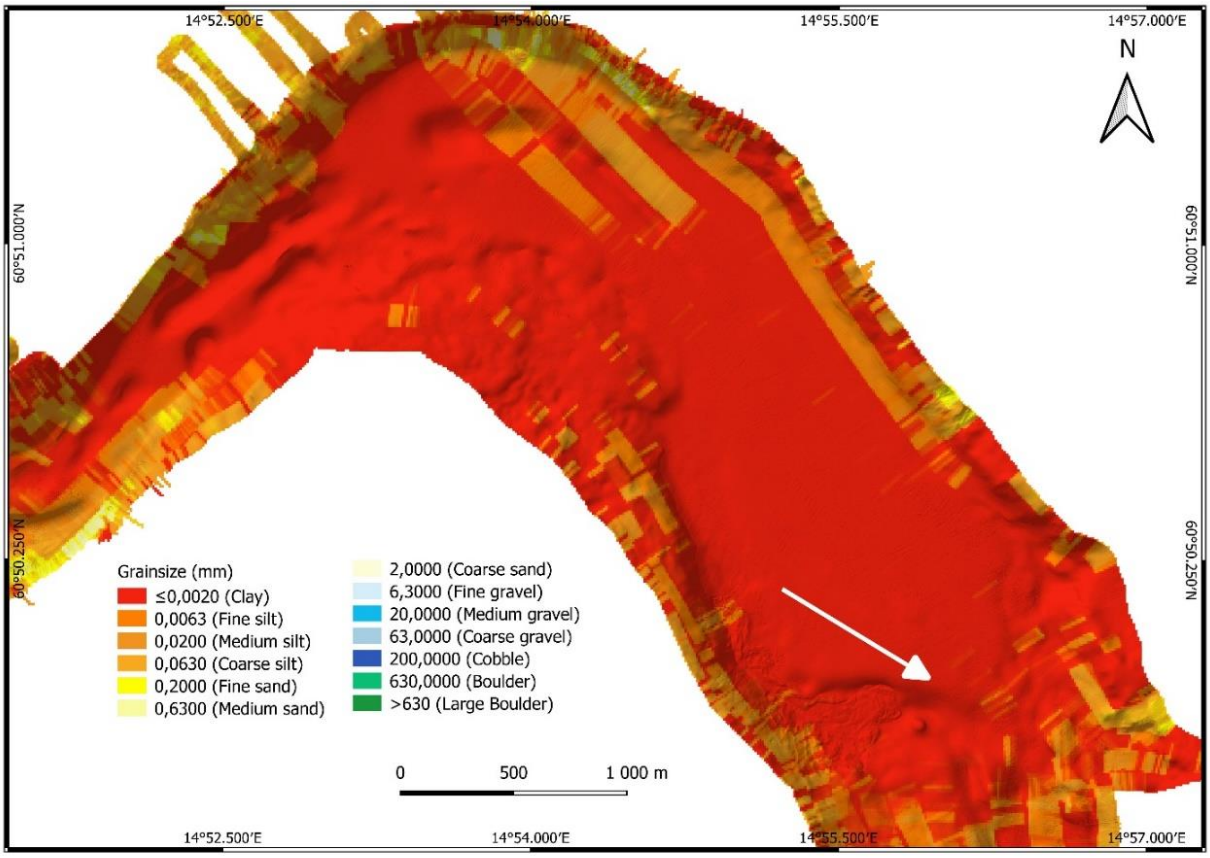

Figure 22. *Grainsize map of the smooth surface in the south-east showing grain sizes in mm.*

A deep area exists in Österviken Bay with depths as deep as 107 meters (Figure 23). It follows the main channel, stretching from north to south for approximately 4850 m, with the deepest part in the north. This area has an irregular shape and is deeper along its central part with steep slopes at the sides. The bottom is covered with hollows and a large, flat topped, shoal with steep sides is located in the southern part of the area (Figure 23).

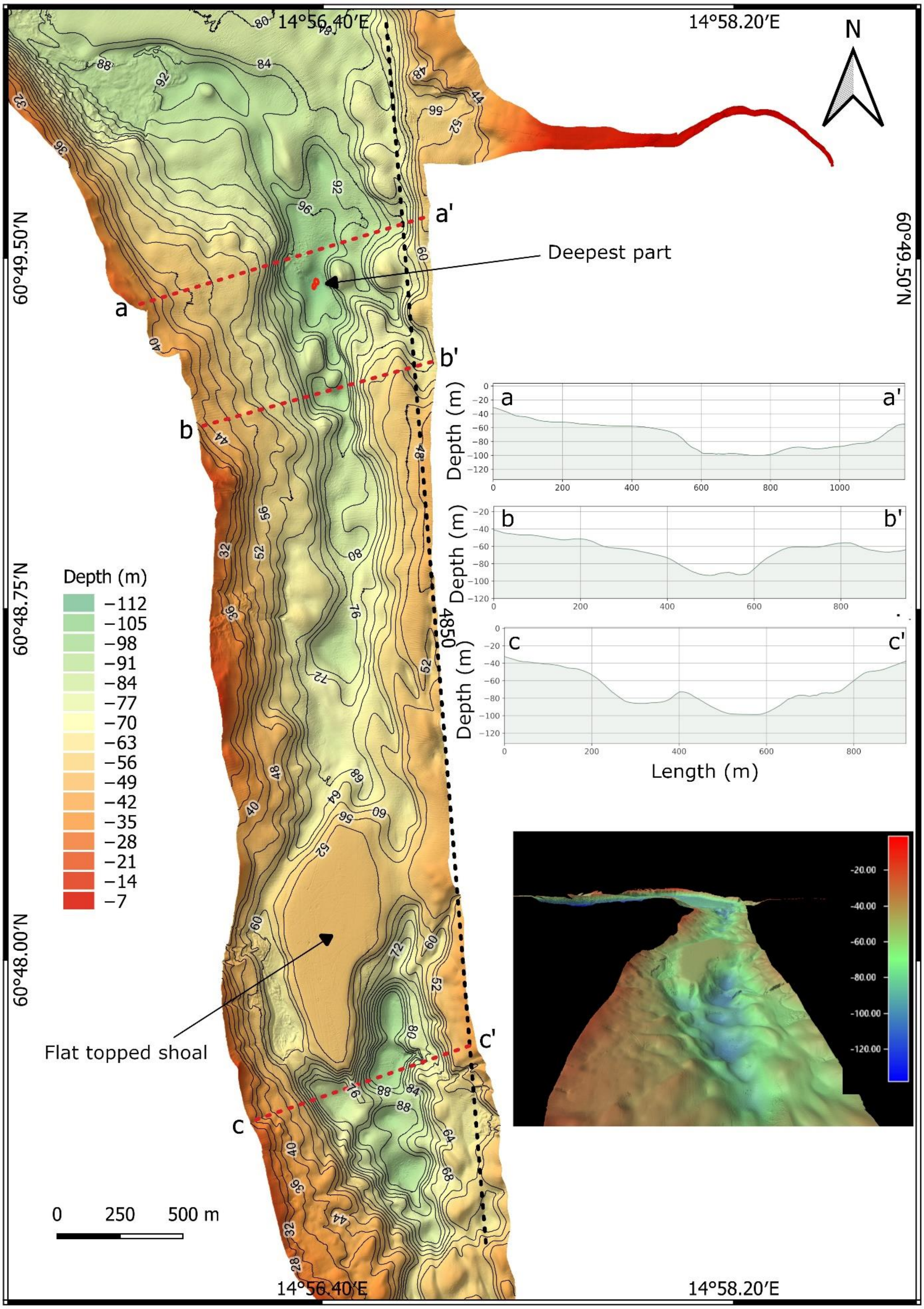

Figure 23. The deep area in Österviken Bay. The deepest part and the flat-topped shoal are marked by arrows.

The grainsizes of surface sediments are generally slightly coarser here in the southern part of the surveyed area compared to further north. According to the ARA-analysis, most of the area is covered with silt-sized particles, but smaller areas of clay and sand also occur (Figure 24).

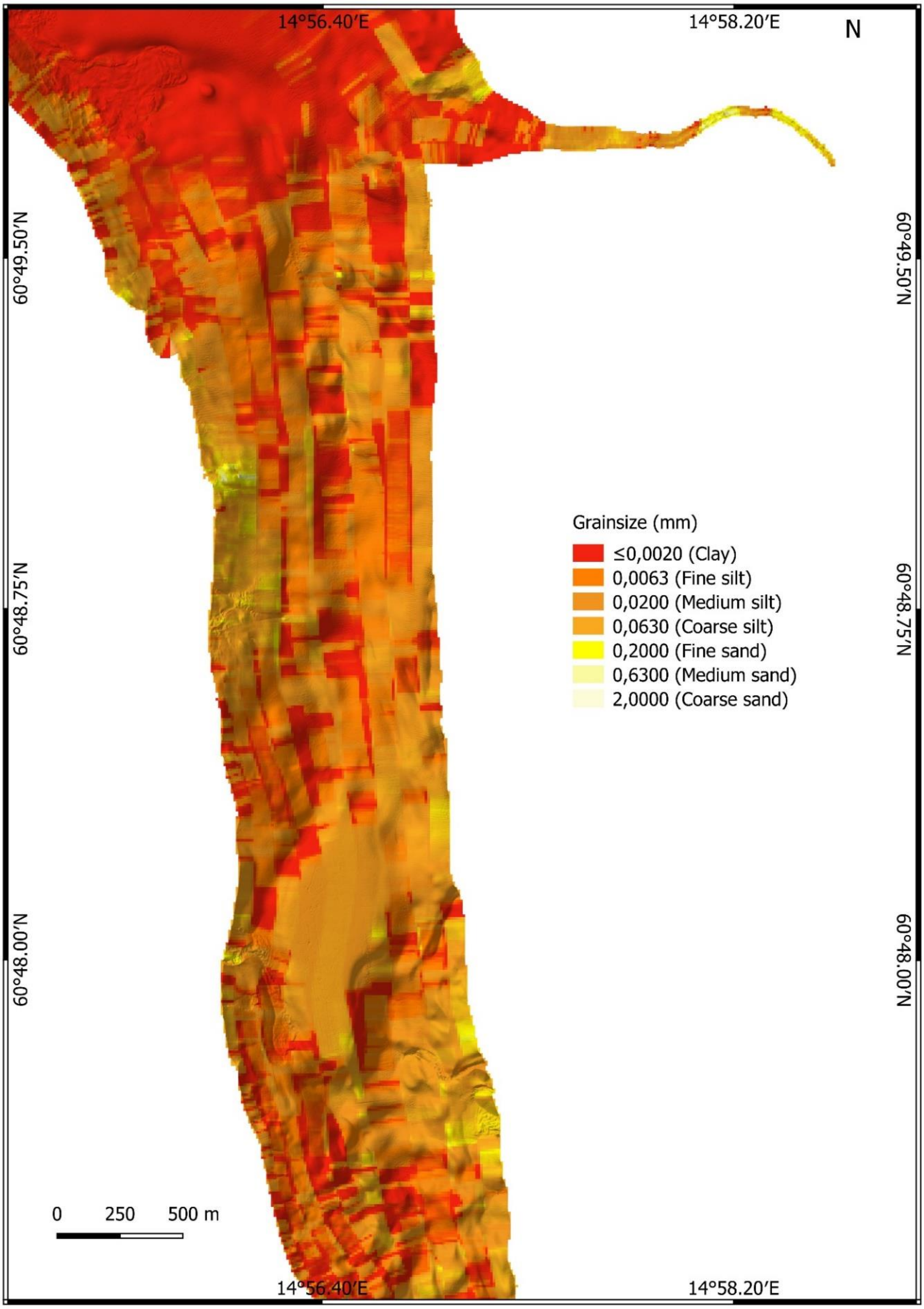

Figure 24. Grainsize map covering the deeper part of Österviken Bay with grainsizes shown in mm. A mixture of grainsizes occurs with silt sized particles dominating.

In the southern part of the deeper area of Österviken Bay the flat shoal mentioned previously is found (Figure 25). The flat top of the formation has an area of about 268600 m^2. The sides of the surface have steep slopes to the south and east while the slopes are less steep to the east and north. In a few locations, the shoal seems to have been connected to surrounding landforms. The top of the shoal is approximately 50 m deep and the deepest depth in the surrounding area is 93 m and located southeast of the shoal (Figure 25) (Figure 26).

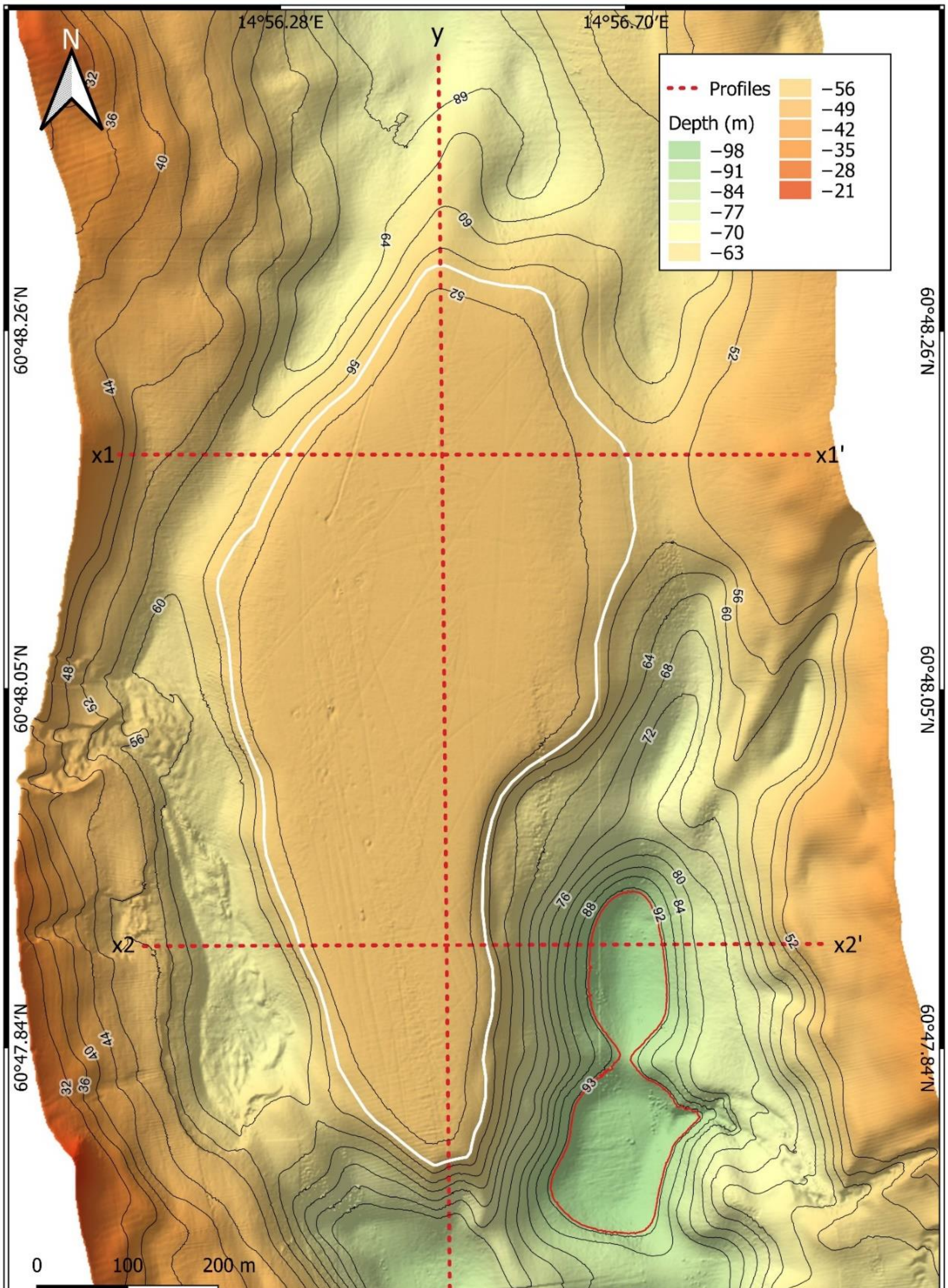

Figure 25. The flat shoal found in Österviken Bay. Red contours show the deepest area surrounding the shoal. The profiles x1, x2 and y are seen in Figure 26.

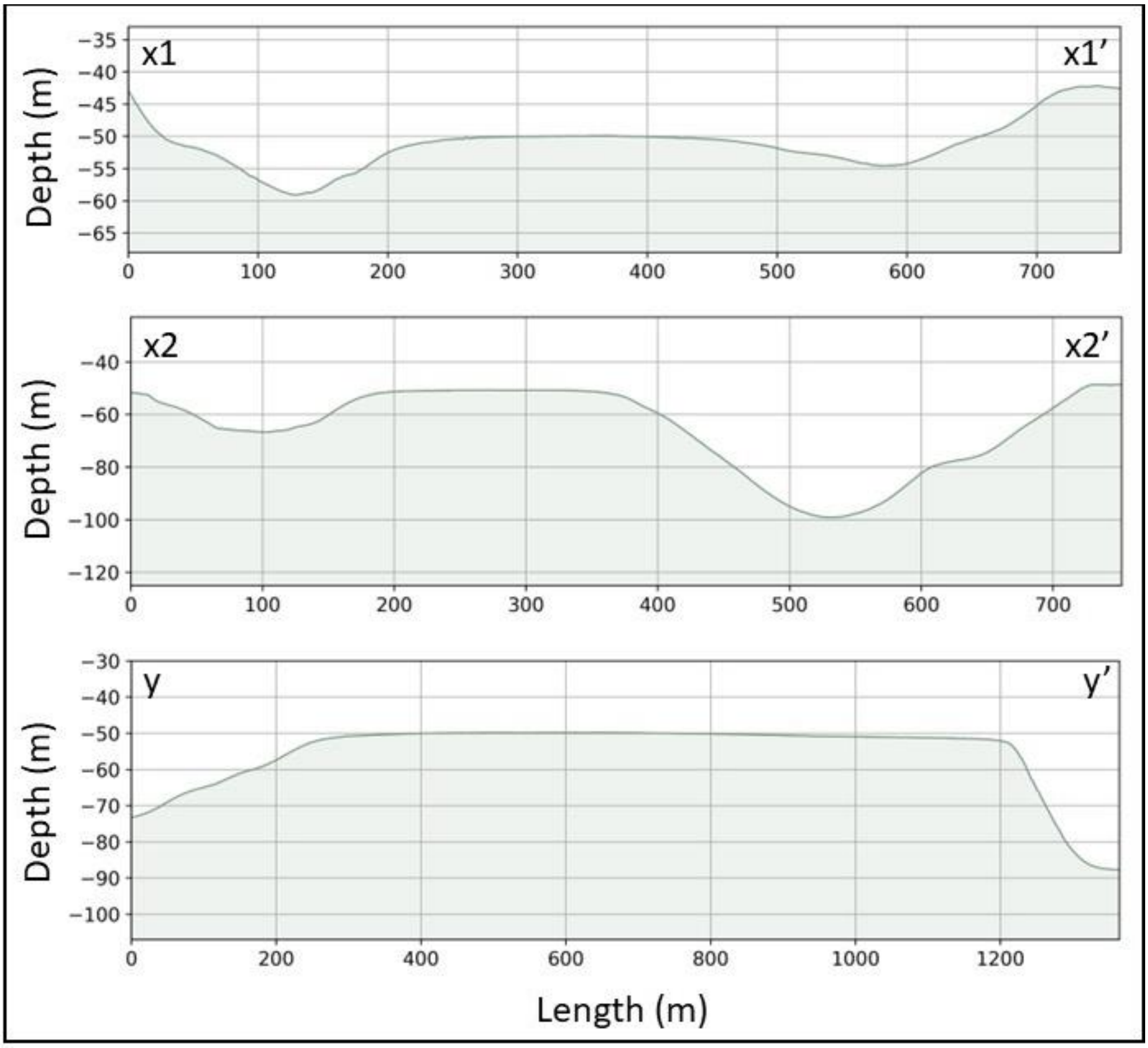

Figure 26. *Profiles of the flat shoal in Figure 25.*

The ARA indicates silt sized grains on most of the flat surface. Patches of finer and coarser materials are found on the slopes and on the edges of the top surface (Figure 27).

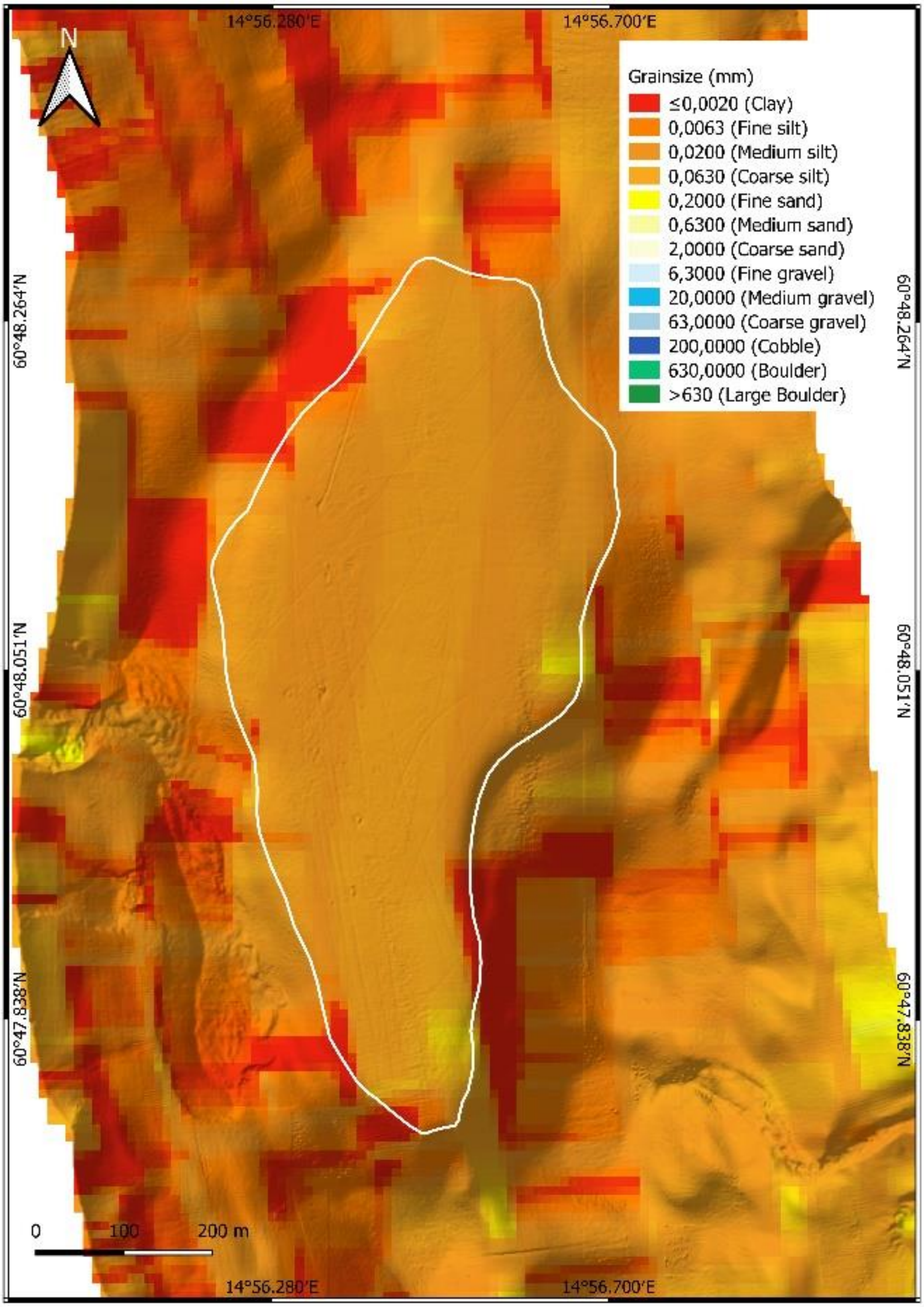

Figure 27. Grainsize map of the flat topped, elevated surface with the grainsize shown in mm.

The southern part of the Österviken Bay has a complex bathymetry with hills and ridges of different length (Figure 28). The name hill is in this work used for rounded, elevated features in the lake floor, while the name ridge is used for elongated features. Looking at the direction of their longest axis, the hills are unevenly distributed. With respect to their aspect, meaning the direction of their slopes, they can be connected into longer ridges. When connecting the hills, a complex pattern of braided broken ridges may be visualized. These ridges are mostly round- or sharp-crested with occasional flat- and multi-crested parts (Figure 29). The ridges follow the river channel and the direction of general ice-flow, except for in the southern part of Österviken Bay where a different pattern appears. The longest ridge has a length of ~2440 m, while the width of the ridges varies between about 28 m and 204 m, and the height between about 13 m and 61 m. The water depth of the ridge crests varies from 86 m in the north to 10 m in the south.

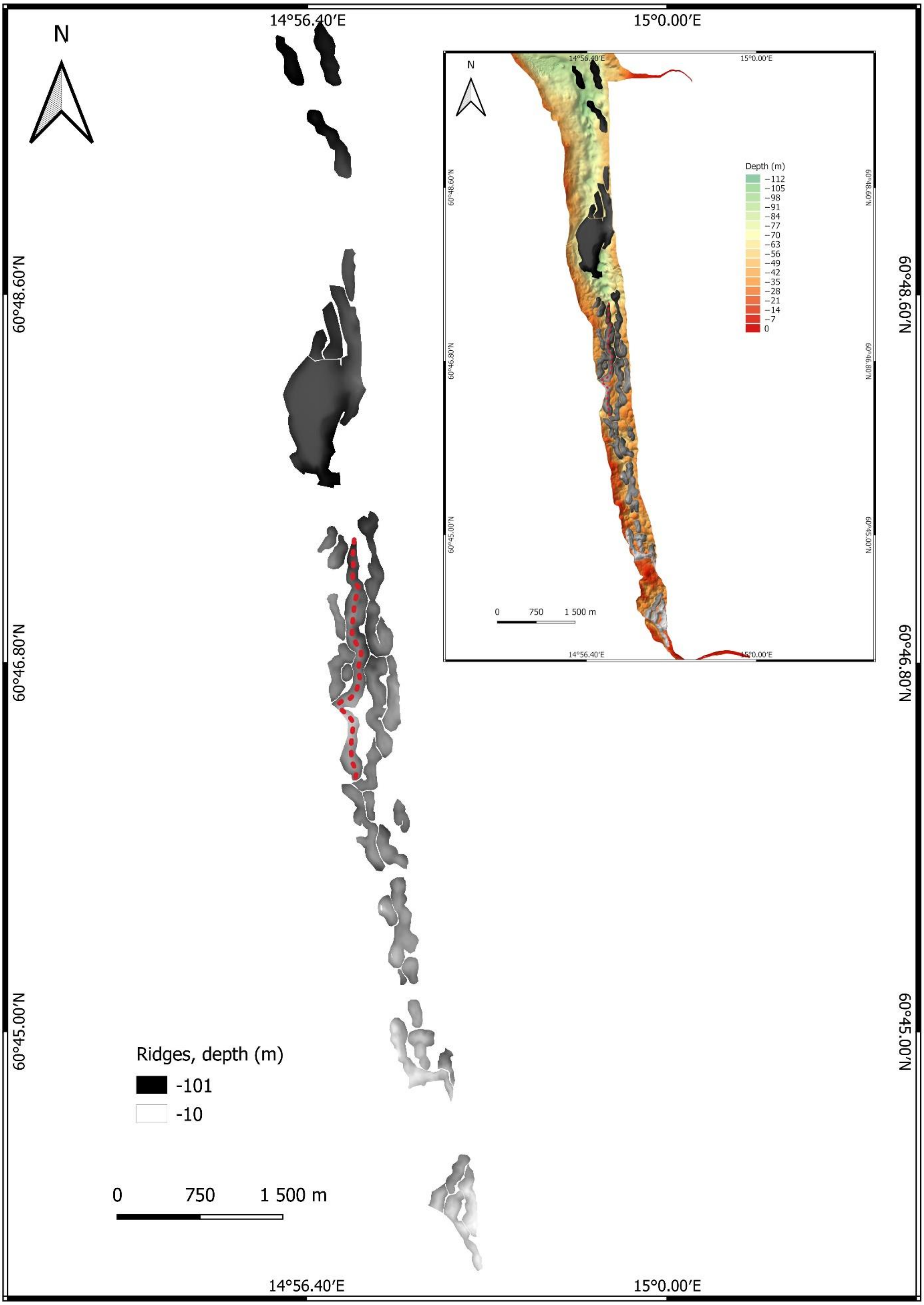

Figure 28. *Map of the ridges found in Österviken Bay. Very small hills or hills difficult to connect to others with the help of their slope and azimuth are not shown in this map.*

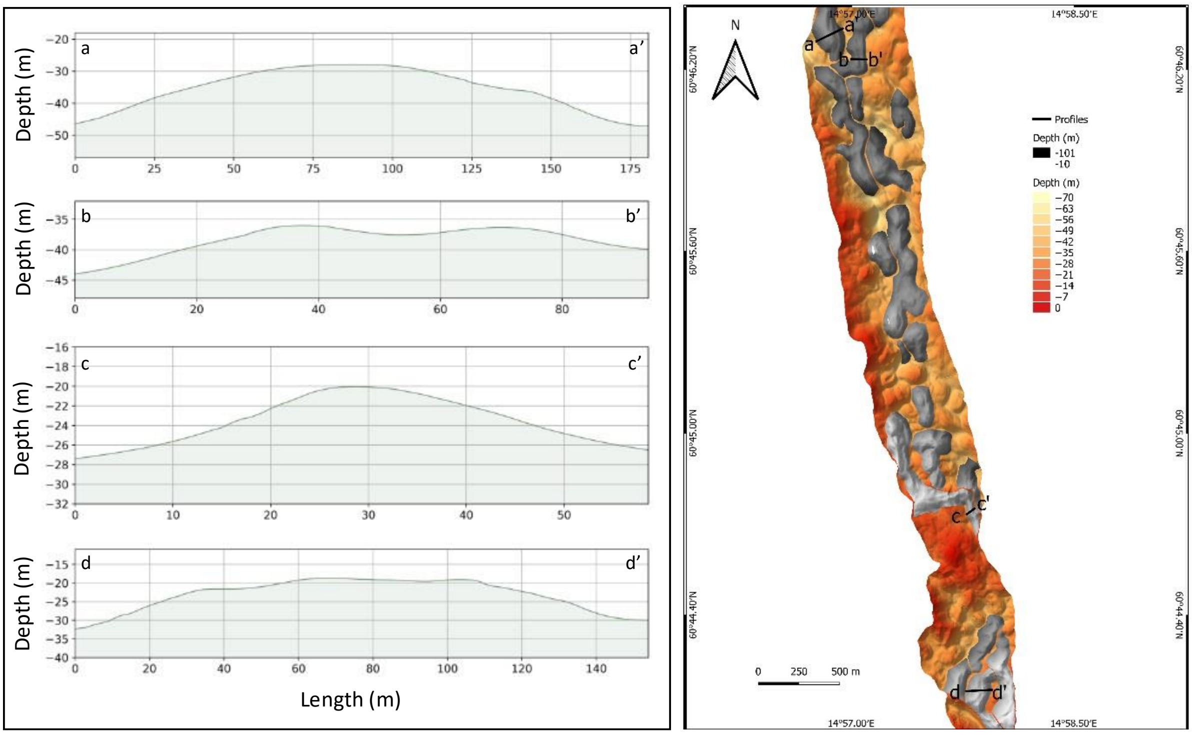

Figure 29. Bathymetric profiles showing a) round-crested, b) multi-crested, c) sharp-crested and d) flat-crested parts of the ridges.

The southernmost part of the surveyed area of the Lake Siljan has a mixture of grainsizes, from clay to sand, according to the ARA-analysis. In the north of this area, silt is dominating while going south an increase in areas covered with clay occurs (Figure 30). Most of the ridges are covered by silt and sand with some patches of clay, except from a few ridges in the south where clay dominates.

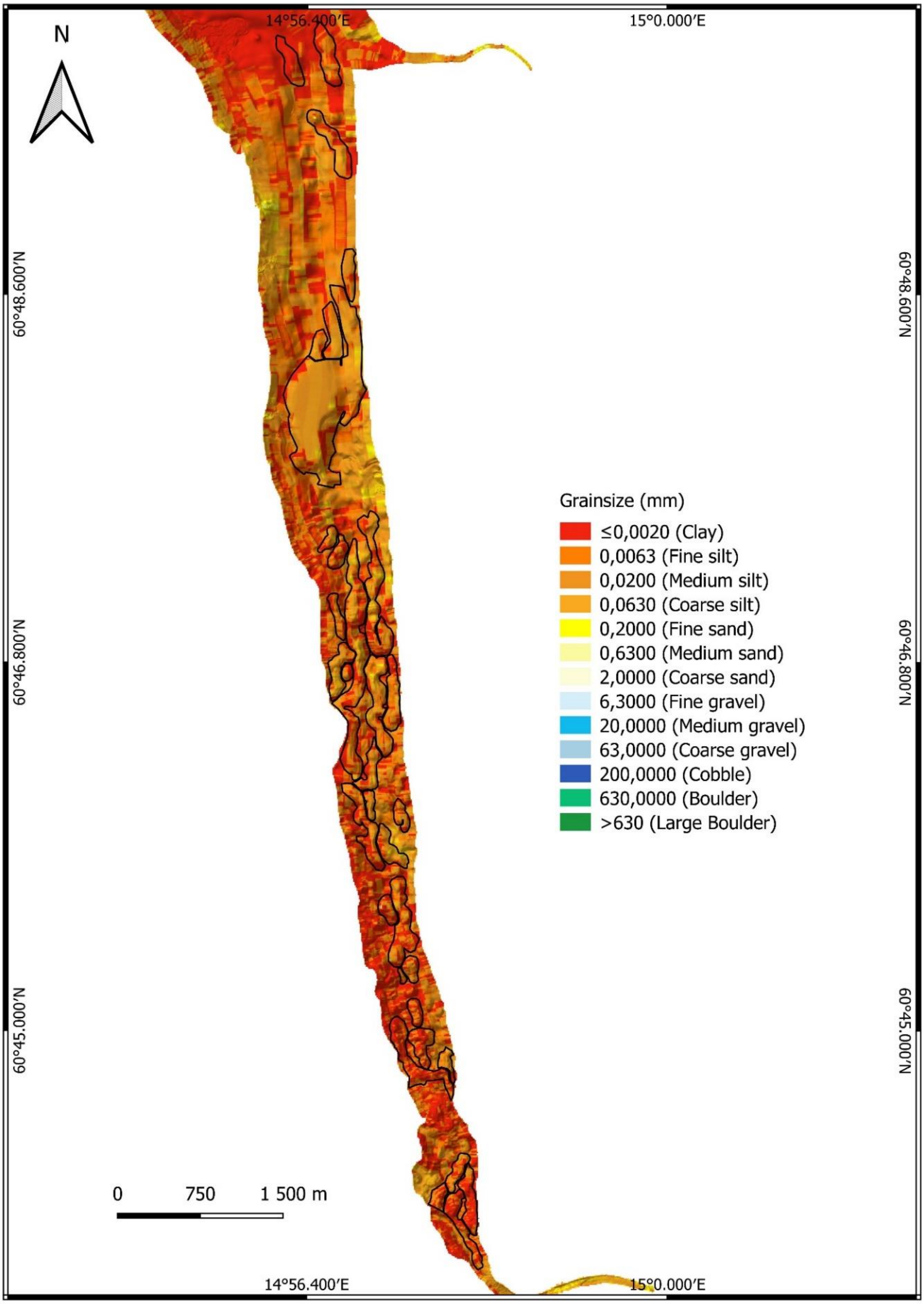

Figure 30. Grainsize map based on the ARA-analysis of the southern part of the surveyed area containing ridges. The estimated grainsizes are shown in mm.

4.2. Sub-bottom profiles

Three different acoustic units are here defined using the acquired sub-bottom profiles. These units are in the north-western survey area named 1a, 2a, and 3a while they are named 1b, 2b and 3b in the area further to the east, where some differences in the acoustic characteristics are seen. The acoustic unit 1a, having a maximum thickness of ~5.4 m in Figure 31, is characterized by low to medium amplitude, acoustically well stratified, continuous reflectors. Unit 2a, with a maximum thickness of ~2.9 m, has a more acoustically chaotic appearance with medium to high amplitude reflections. Unit 3a has a maximum thickness of ~5.3 m and the reflectors are of low amplitude and acoustically stratified. The acoustic stratification is however not as pronounced as in unit 1a. Along the slopes, the sediments are acoustically transparent to semi-transparent, at least partly most likely an effect of the slope itself on the data acquisition.

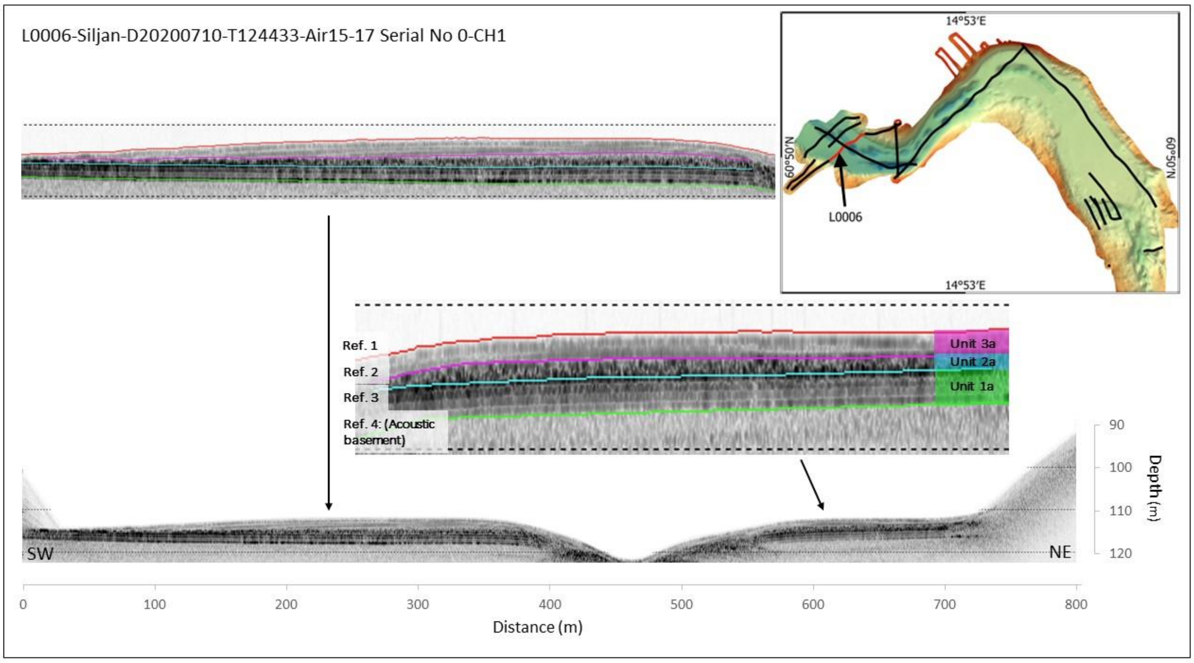

Figure 31. Sub bottom profile from the north-western part of the survey area with reflectors and units 1a, 2a, and 3a illustrated.

In figure 32 the same three units can be located but the amplitude of the reflectors is higher than in figure 31. A bow tie occurs when the vessel moves over a narrow depression and makes it difficult to interpret the correct position of the seafloor in the depression (Figure 32).

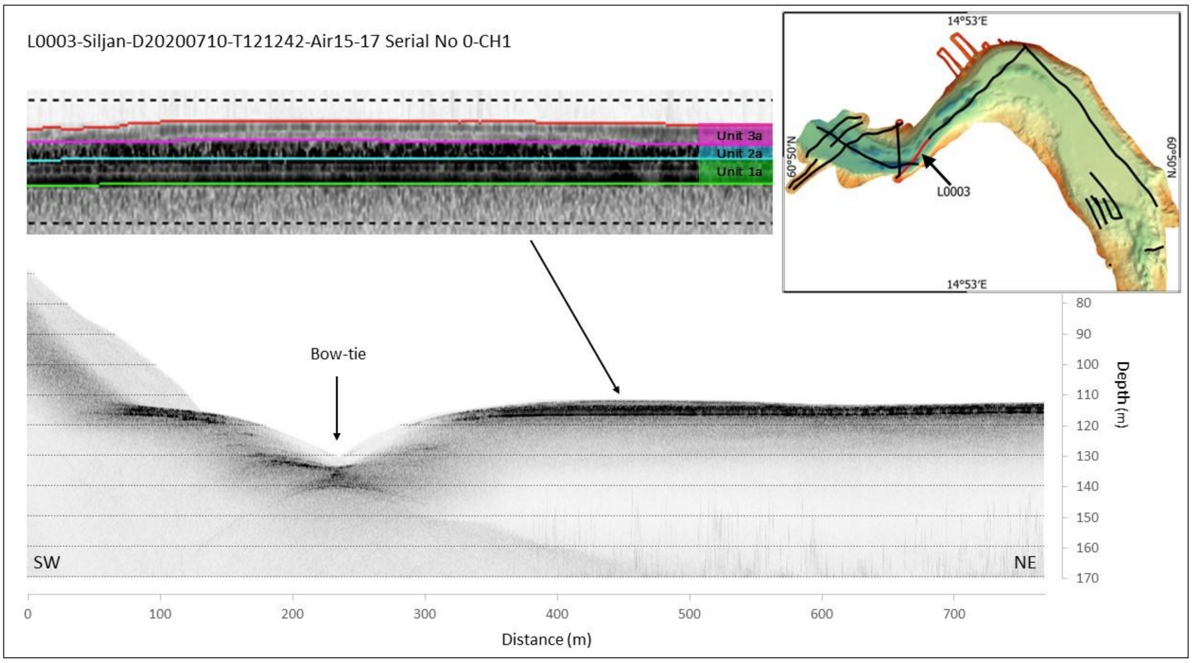

Figure 32. Sub bottom profile showing the same units as in figure 21. A bow tie complicates the interpretation of the lake floor in the depression.

Above the slopes of the main channel in the north-western part of the survey area, the sediment layer is thinner and acoustically transparent to semi-transparent. It covers an irregular, impenetrable or homogenous acoustic basement (Figure 33).

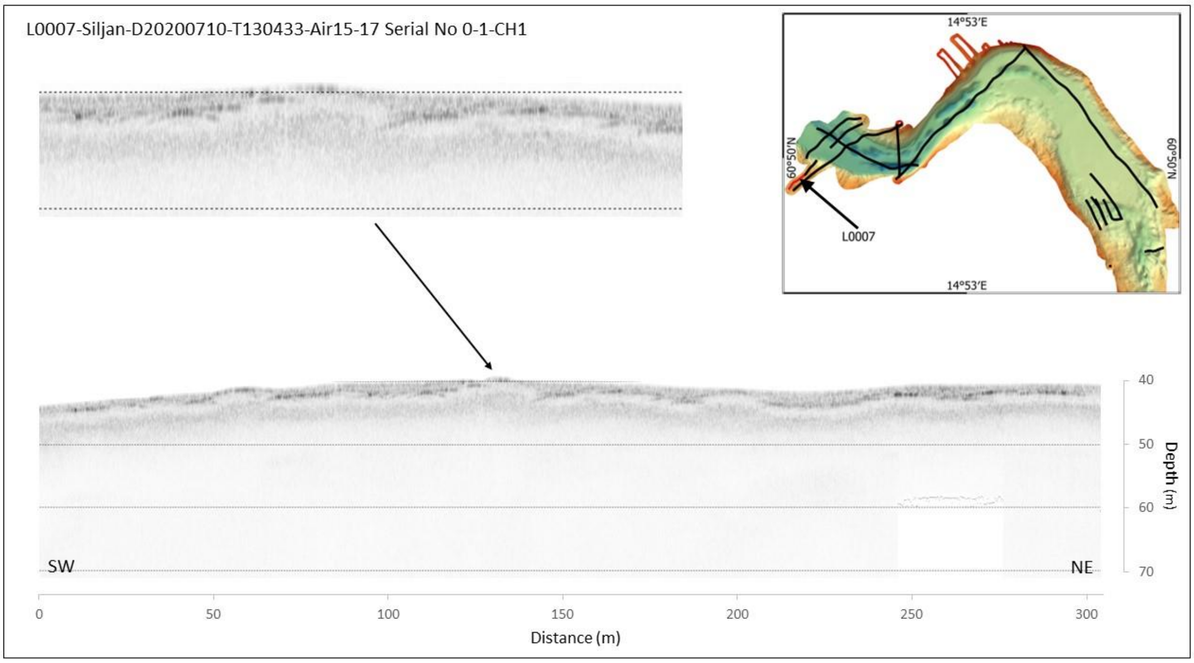

Figure 33. Outside the main channel seems thinner in the sub-bottom profiles.

The four prominent reflectors in the sub-bottom profiles recognized in the north-western part of the survey area are also found in the northeast. But the acoustic appearance of the units is not completely the same in the two areas. Unit 3b is acoustically stratified with medium amplitude reflectors and has a maximum thickness of ~3.4 m in the profiles shown in Figures 34 and 35. In unit 2b, with a maximum thickness of 5.5 m, acoustic stratification is clearly seen in Figure 34, but not as clearly in Figure 35. The reflectors are of low to medium amplitude. In the profile shown in Figure 35, Unit 2b is mostly acoustically transparent to semi-transparent, with some areas showing signs of stratification. Unit 1b has a maximum thickness of ~5.46 m and is acoustically transparent to semi-transparent with some signs of stratification. In Figure 34, the stratified layers are following the shape of one of the smaller channels suggesting that the channel was eroded before the deposition of the sediments.

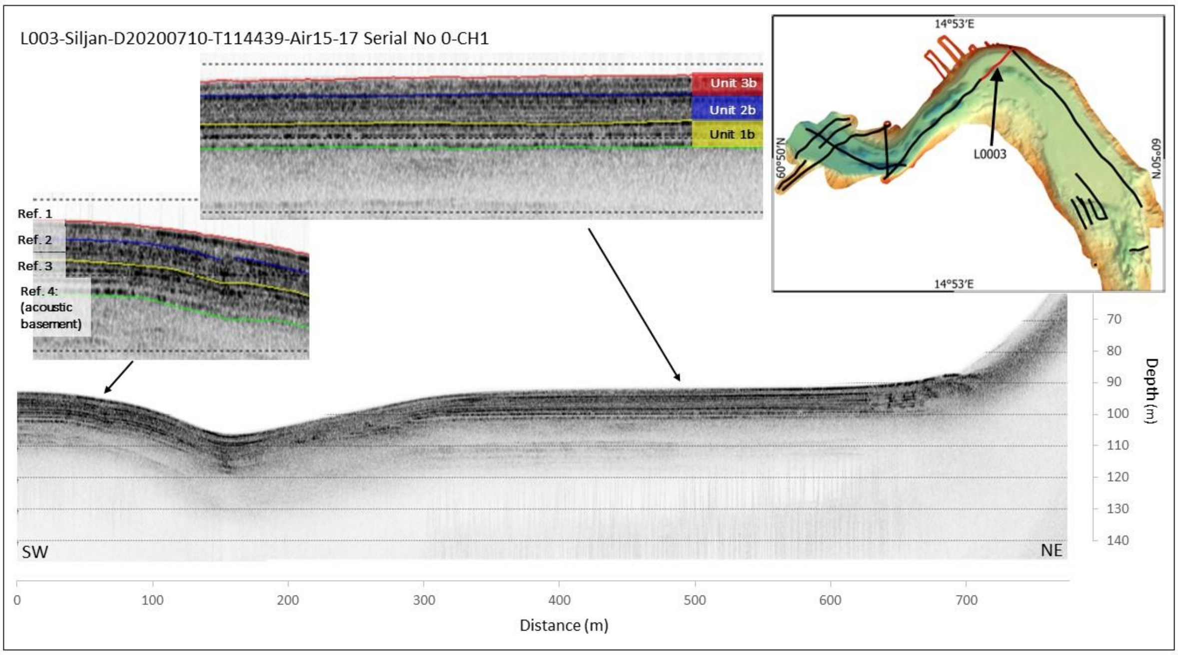

Figure 34. *Sub-bottom profile from the area of the large smooth surface with reflectors and units 1b, 2b, and 3b illustrated. The depression to the left shows one of the smaller channels in the northern parts of the survey area. The stratified sediments are following the shape of the channel, indicating a deposition after the formation of the channel.*

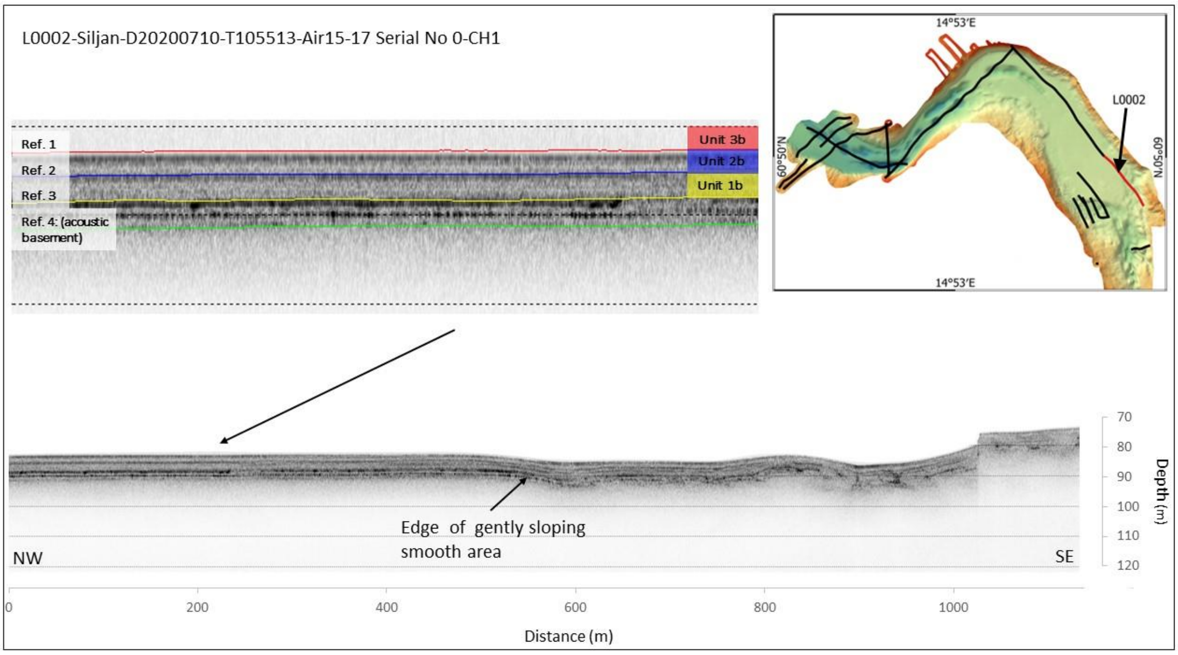

Figure 35. *Sub-bottom profile showing the same units as in 26. To the left the smooth, wedge-shaped surface is located with a smooth acoustic basement. To the right of the smooth surface the acoustic basement becomes more irregular.*

A couple of hills that may be part of the ridges located in Österviken Bay are found on the sub-bottom profiles (Figure 36) (figure 37). They are both lens shaped with an acoustically semi-transparent to chaotic appearance that may be caused by gas blanking. In figure 36 a stratified layer may be seen on top of the hill.

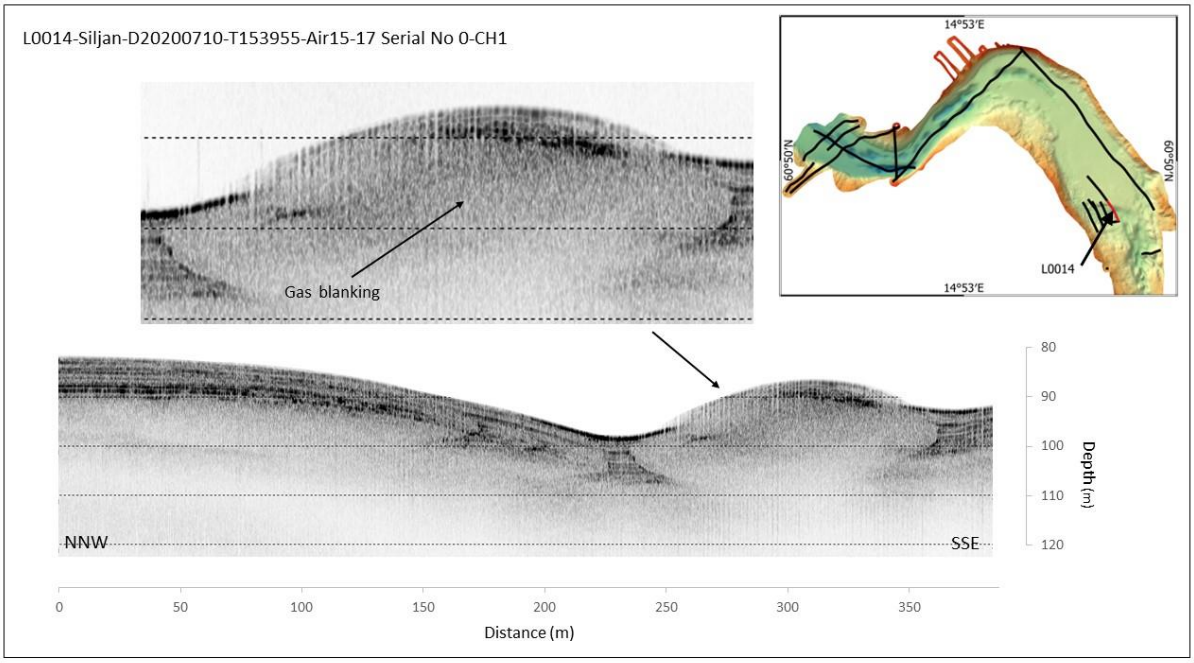

Figure 36. A hill shown in sub-bottom profile L0014. Some stratified sediments are apparent in the upper stratigraphy of this hill, while most of it has an acoustically semi-transparent to chaotic appearance maybe caused by gas blanking.

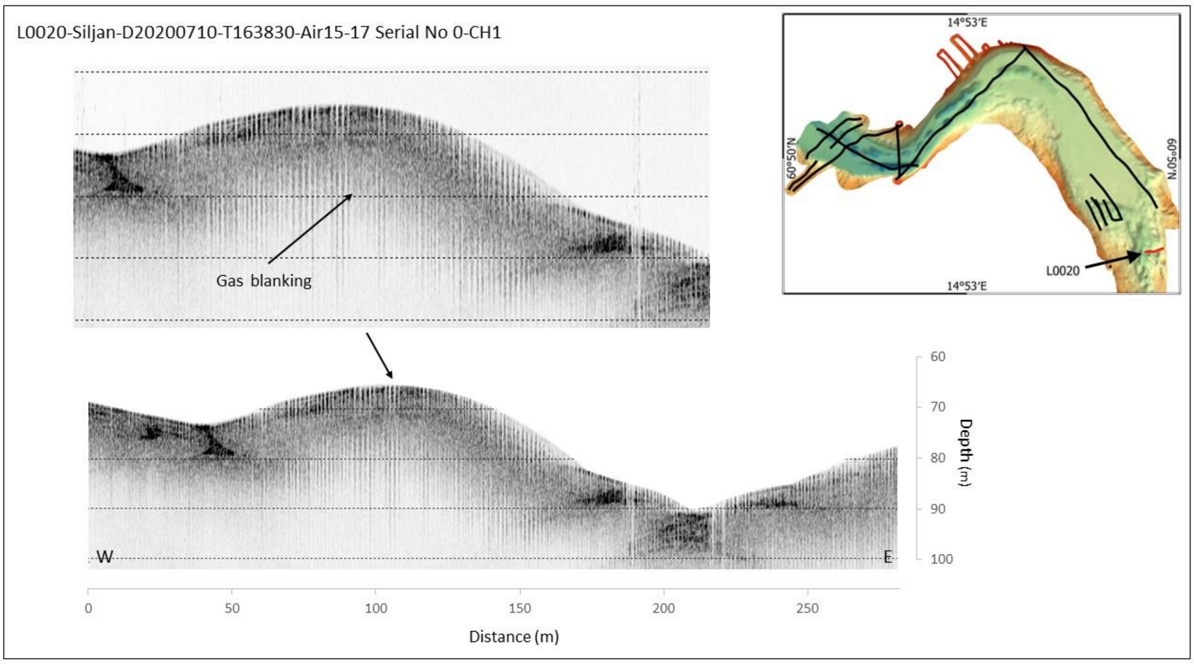

Figure 37. Hill in sub-bottom profile L0020. In this profile, no acoustically stratified layers are visible within the upper part of the stratigraphy. The hill has an acoustically semi-transparent to chaotic appearance maybe caused by gas blanking.

4.3. Mass-transport deposits

Five scars from mass wasted sediments of different sizes are mapped in the survey area (Figure 38). These are here numbered 1-5. Except from mass-transport deposit number 5, they all have occurred along the western slope of the main channel and are directed towards northeast, southeast and east. Mass movement number 5 occurred furthest to the south on the eastern slope of a hill and is directed to the northwest (Figure 38).

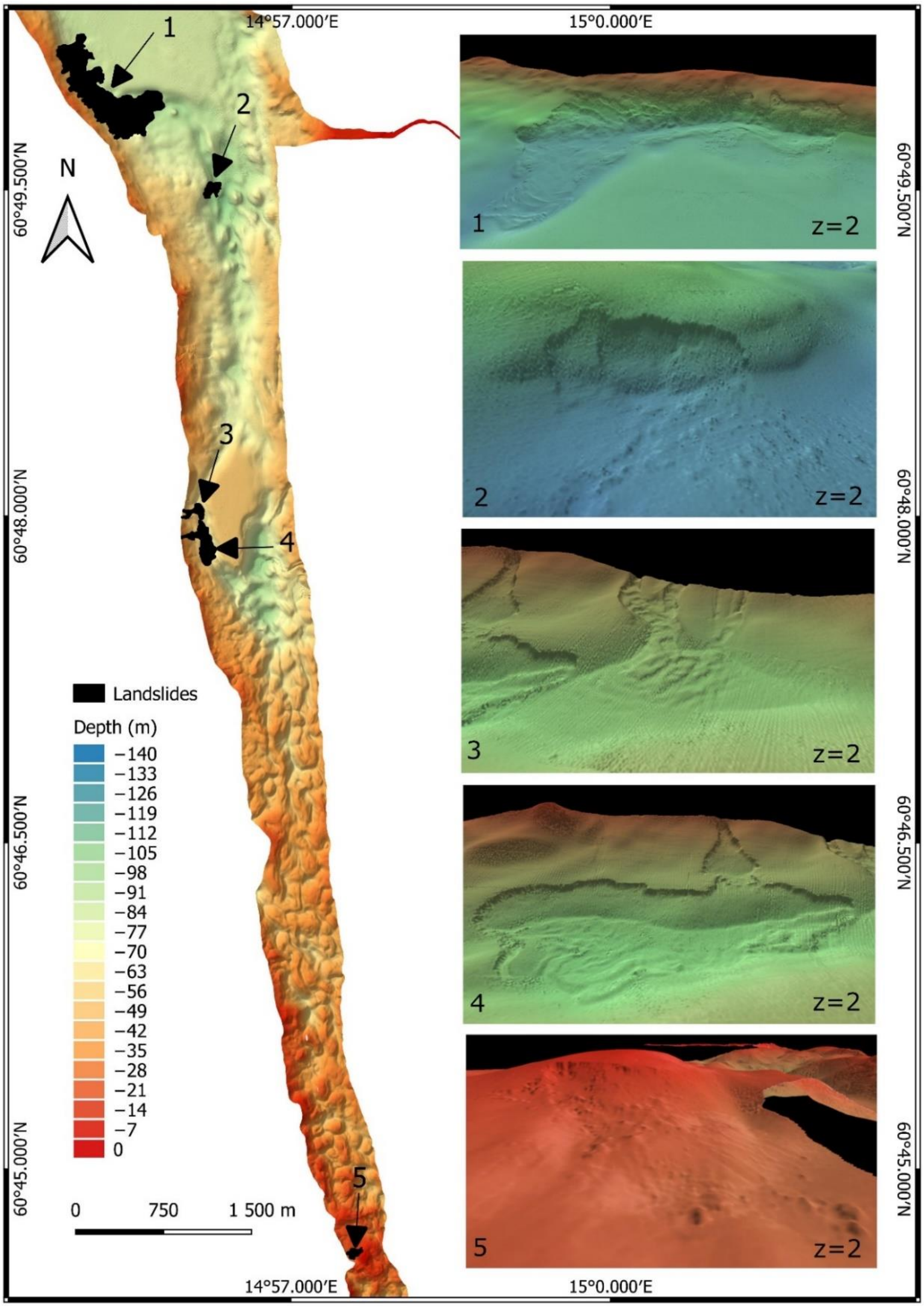

Figure 38. The five mass movement scars mapped in Lake Siljan with the largest one (no 1) locted furthest to the north. Z= over exaggeration.

The scars from the mass movements 1-5 have areas ranging from 7750 m^2 to 293220 m^2. Measures were also taken of the Scarp perimeter length (Ls), Maximum scarp width (Ws), Maximum deposit width (Wd), Total length (Lt), Deposit length (Ld), and Slope gradient (S) as defined by (Clare et al., 2019), (Table 2, Figure 39). Four of the MTDs are quite small and only the largest one will be described further in this text.

Table 2. *Measurements of the five MTDs in Lake Siljan. Areas and volumes are rounded to tens of m^2/m^3 while the other values are rounded to whole meters.*

MTD	1	2	3	4	5
Area (m^2)	279910	13650	12680	41950	7750
Volume (m^3)	678650				
S (°)	~17				
Ws (m)	993	149		393	67
Wd (m)	972	140	140	356	97
Ls (m)	1945	220		563	109
Lt (m)	547	114		148	128
Ld (m)	458	22	66	103	47

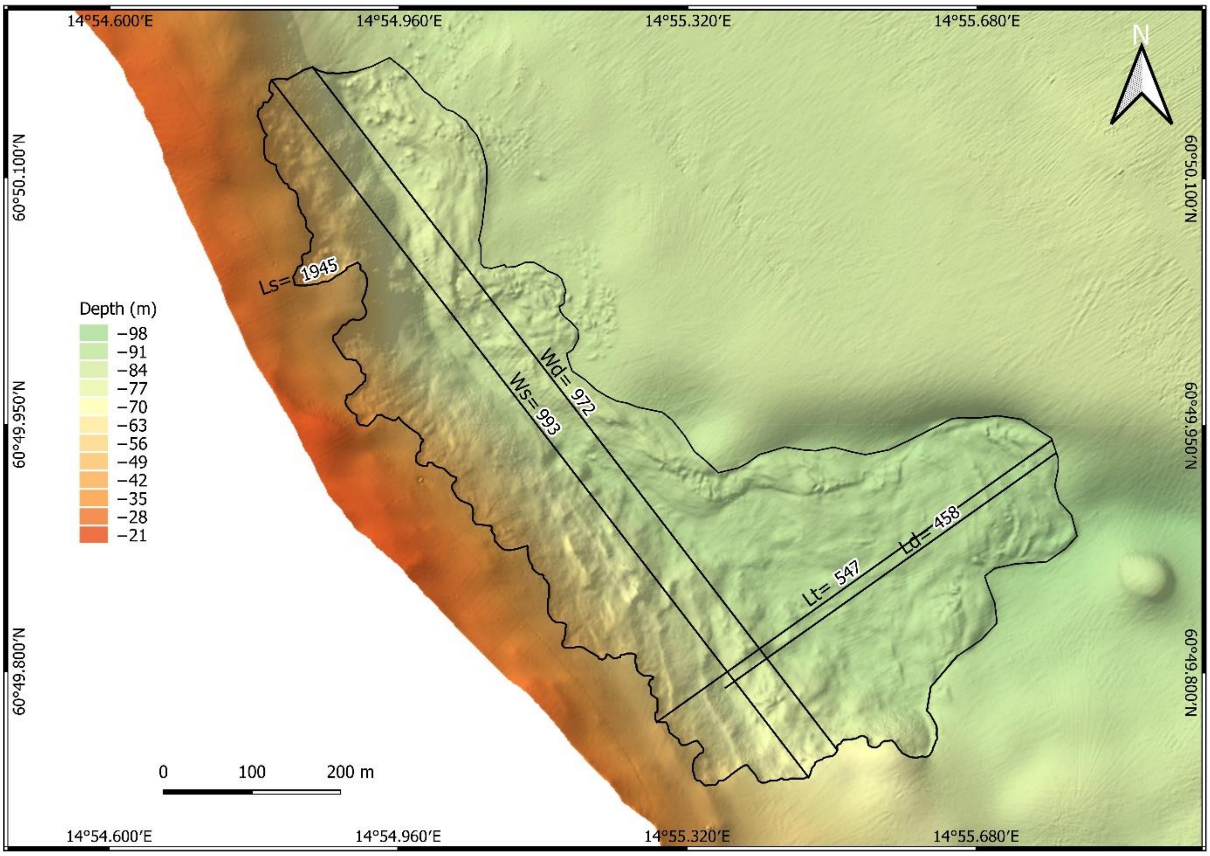

Figure 39. *Measurements of MTD 1, the largest landslide scar found in the survey area. The values are rounded to whole meters.*

The largest MTD (no 1) is located furthest to the north with the head wall situated at about 45 m below lake level, and the surface of the deposited sediments at depths between ~74 m and ~94 m. The headwall of the failure scar is clearly visible above the exposed gliding plane, and below the slope one large and two smaller arcuate lobes are visible (Figure 40). The sediments seem to have been constrained and directed by the shape of the tilted lake bottom described above.

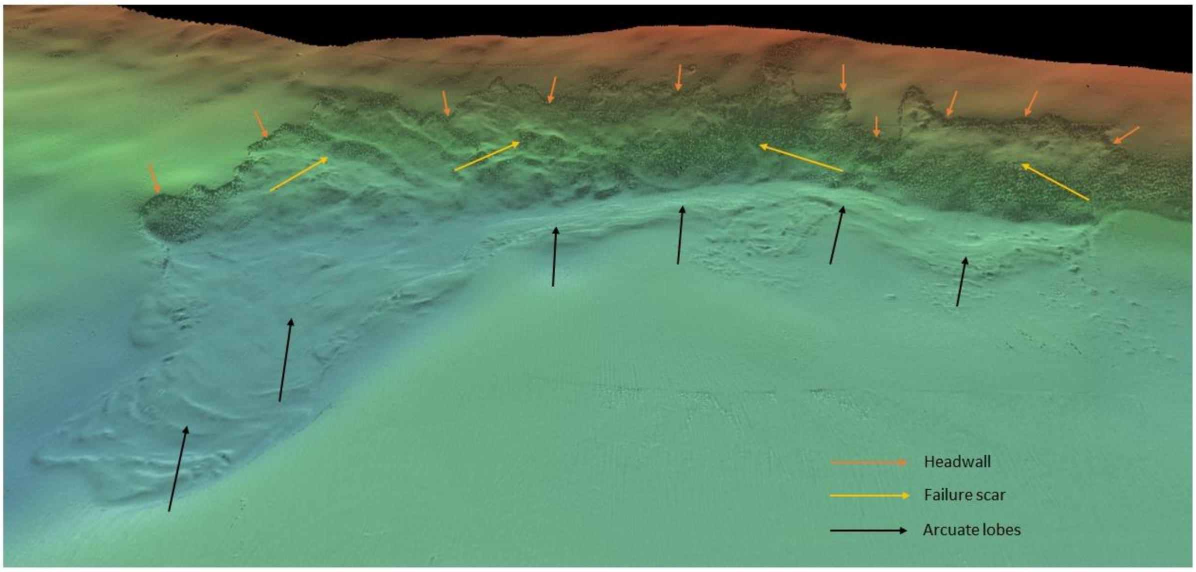

Figure 40. *The headwall, failure scar and arcuate lobes of the largest landslide in Lake Siljan shown by the arrows*

The backscatter map of the slide shows a mixture of high to low backscatter values with the low values dominating. The different backscatter values create a detailed picture of the MTD (Figure 41).

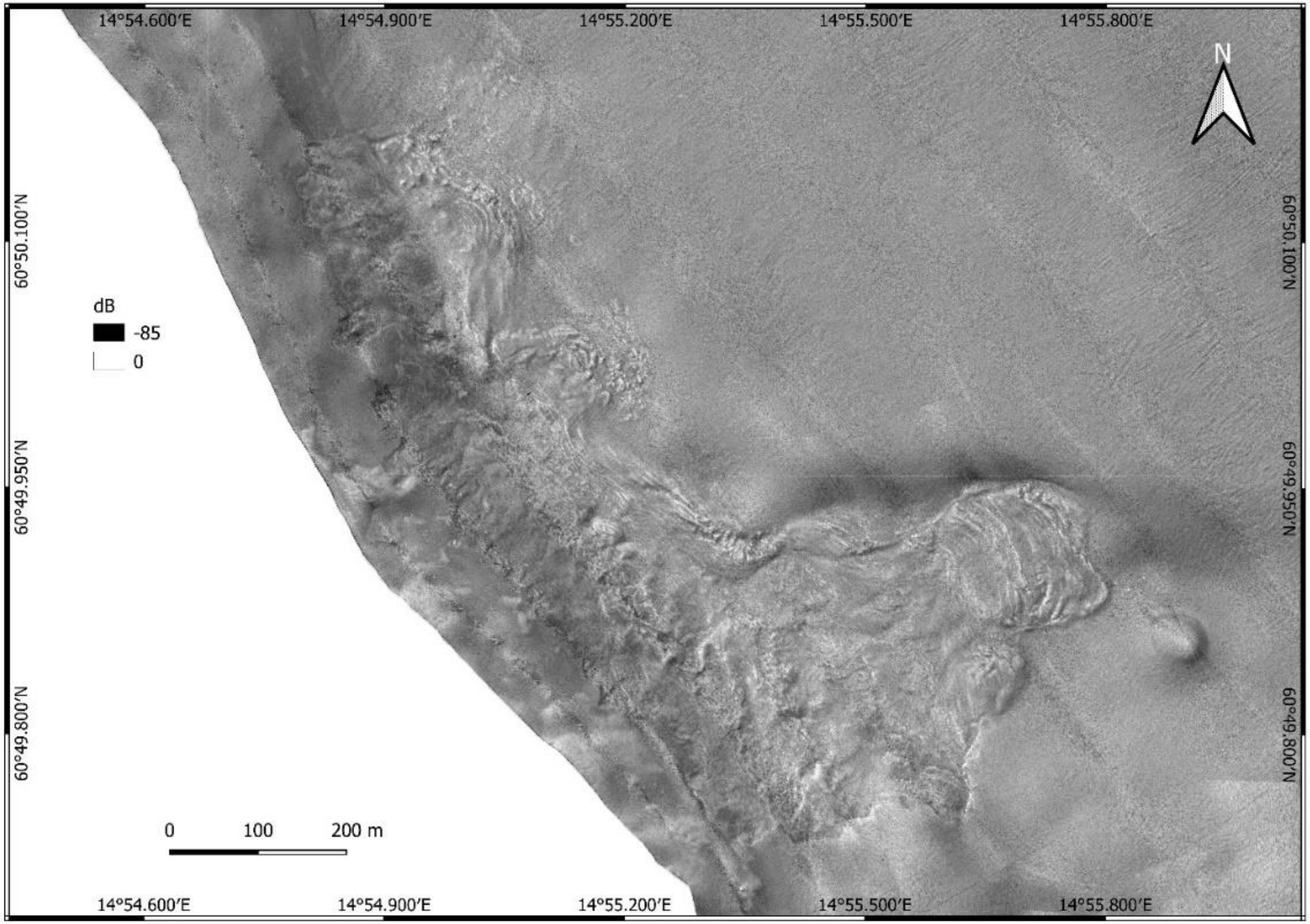

Figure 41. In the backscatter map the MTD is clearly seen with both high and low backscatter values revealing theMTD in beautiful detail.

The ARA-analysis suggests that most parts of the mass-transport deposits area is covered by clay, but silt sized materials are found on the upper parts of the slope and in some smaller parts of the deeper areas (Figure 42).

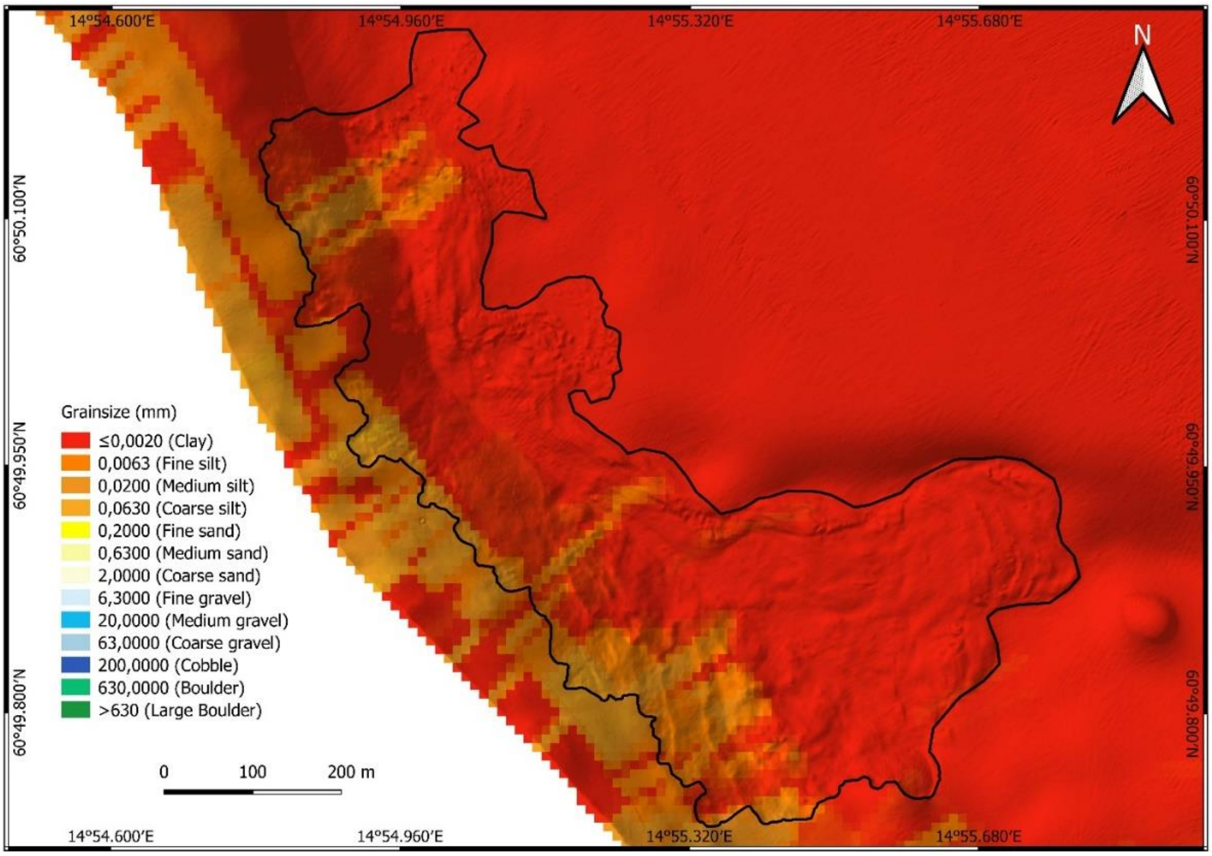

Figure 42. Grain size map of MTD 1 showing the grainsizes in mm.

The sub-bottom profiles reveal that the sediments transported and disturbed by the MTD have a semi-transparent to chaotic character, which differs from the adjacent acoustically stratified sediments (Figures 43 and 44). The basal shear surface cannot clearly be identified below the disturbed sediments, except for in Profile L00118, where it can be traced from below the undisturbed sediments into the slide area as an exposed slide surface (Figure 45). The acoustic basement is sometimes difficult to see, but it appears to be irregular below the mass-transport deposit masses and smoother at the end of the tilted smooth surface (Figure 44).

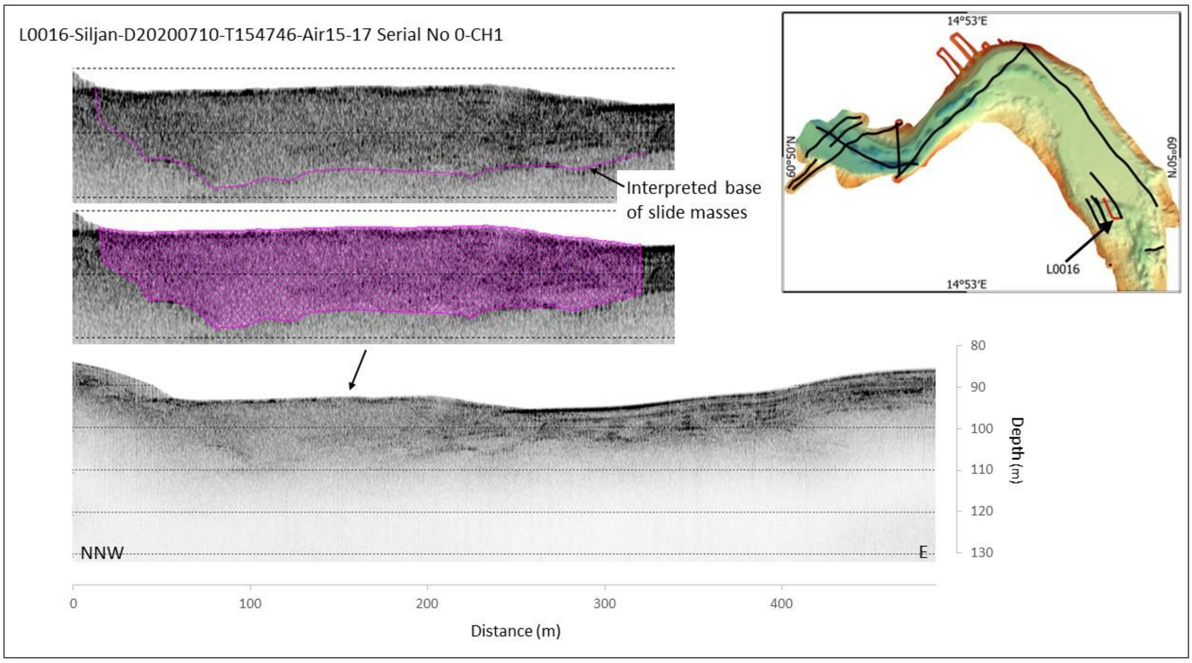

Figure 43. *Profile L0016 showing sediments disturbed by the MTD with a semi-transparent to chaotic appearance.*

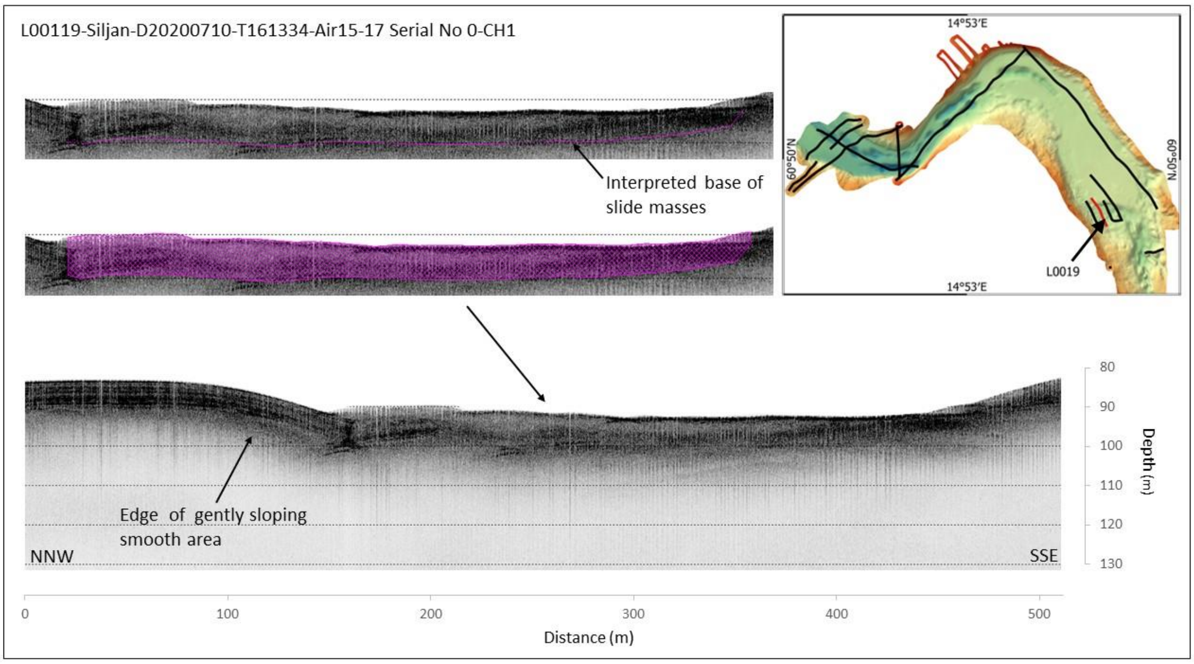

Figure 44. *Profile L00119 showing sediments disturbed by the MTD with a semi-transparent to chaotic appearance. To the left of the MTD masses in the profile, the edge of the gently sloping smooth area can be located. The acoustic basement below the smooth area is less irregular than below the mass wasted sediments.*

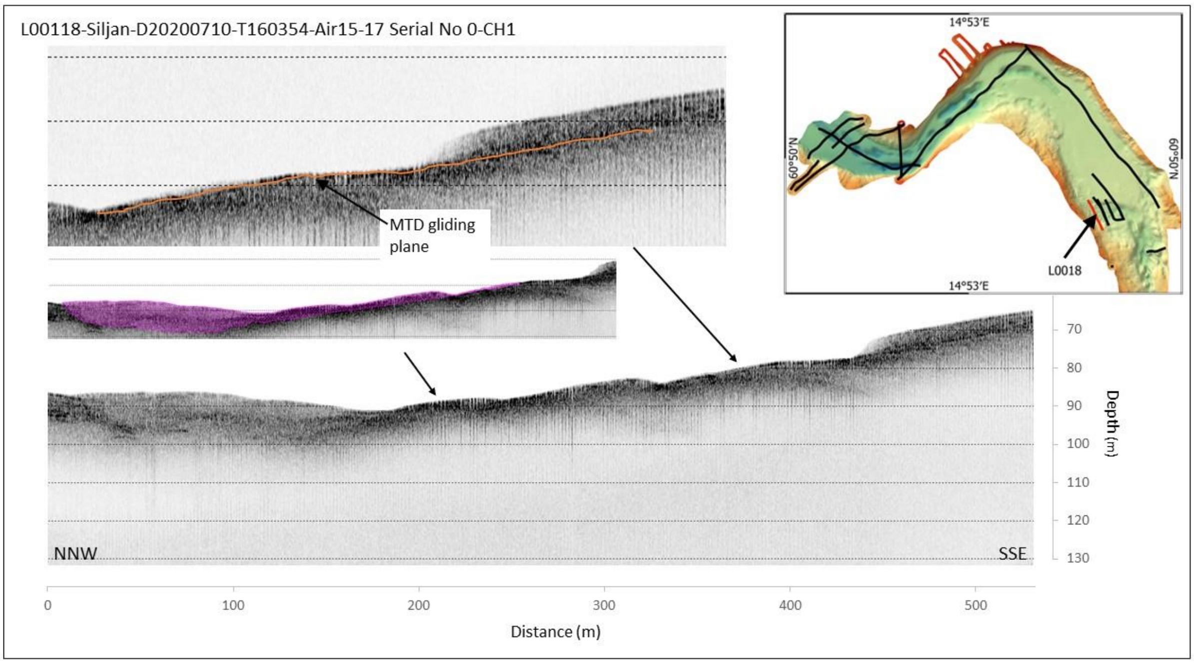

Figure 45. *Sediments disturbed by the mass-transport deposit are seen having a semi-transparent to chaotic appearance. The sliding surface is marked in orange where the exposed layer can be followed from the slide scar in under the undisturbed sediments above.*

5. Discussion

5.1. Interpretation of landforms

The characterizing and interpretation of landforms are here supported by different map layers in QGIS showing slope, aspect, contours, and slope contours. In particular, details not easily seen in the bathymetry are revealed when analysing the aspect of various lake-bottom features. The RVT Multi directions hillshade tool was also useful to avoid azimuth biasing. The ability to visualize the landforms in 3D using Fledermaus also helped with the interpretation, specifically changing the vertical exaggeration made it easier to compare different landforms not easily visualized in QGIS.

The large sinuous channel framing the survey area is here, in accordance with Möller et al. (2022), interpreted to be the pre-glacial river valley of Österdalälven, which continues south from Österviken Bay where it is filled with sediments. In this paleo-river valley several different landforms can be distinguished, most of them likely being glacial in their origin, possibly representing a subglacial drainage system (Figure 46).

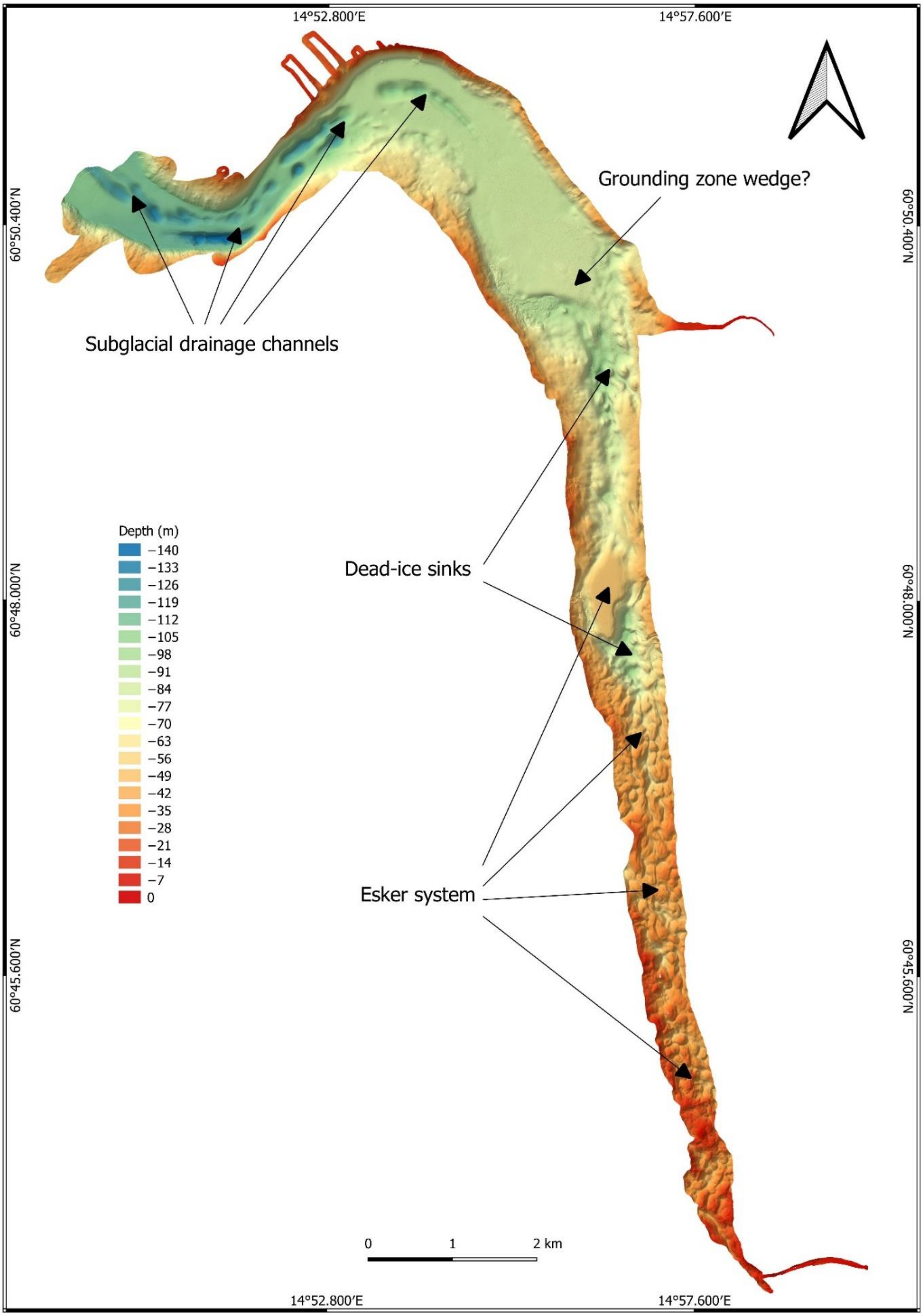

Figure 46. *The survey area with its different landforms illustrated.*

The elongated depressions found in the north-western part of the surveyed area of the lake may be the surface expression of underlying subglacial drainage channels or of deeper parts of the paleo-river channel partly filled with sediments. For the surface expression to be so clearly visible in the bathymetry, the underlying channels may have re-used several times (Simkins et al., 2021). An existing channel may be re-used during several stages of a glaciation, but also during different glaciations (Greenwood et al., 2007). Since existing channels are likely to be re-used, it may be possible that these channels, that are nicely following the shape of the river valley, were a part of the pre-glacial Österdalälven.

The smooth inclined lake bottom in the north ends up in a wedge-like formation ending before slide no 1 (Figure 44). This may be a grounding zone wedge (GZW) or an ice proximal fan, both of which are formed at the grounding zone of a glacier ending in water (Batchelor and Dowdeswell, 2015). These landforms are typically formed during periods of ice stability and a well-developed GZW may need decades or centuries to form (Batchelor and Dowdeswell, 2015). Since the shape of the landform in our case follows the shape of the relatively narrow river valley, it is difficult to determine whether sediment delivery occurred along a line source of the grounding zone or from a point source at the grounding zone. With sediments of GZWs being delivered from a line source and ice proximal fan sediments being delivered from a point source (Batchelor and Dowdeswell, 2015), determining this would assist the interpretation of this landform. The wedge shape of the formation and the lack of fan shaped appearance, leans towards that this is a GZW, implying that the ice halted here during its retreat for some time. On the other hand, supporting an ice proximal fan is the limited expansion of the feature, i.e., it does not reach outside of the channel.

The deep area in Österviken Bay differs from the areas around it where a larger volume of sediments seems to have been deposited. This may be a preserved part of the pre-glacial Dalälven not hidden by glaciofluvial sediments. This deep area may also have formed a part of the subglacial drainage system. If the Scandinavian ice sheet in this area was cold based before deglaciation, there is an increased possibility that the old river channel is preserved.On the bottom of the channel what seem to be eskers can be found. The flat-topped shoal located in the deep area in Österviken Bay, may be a part of an esker system formed in an ice-walled canyon with deposition in standing water. The flat-topped surface seems to be elevated above surrounding ridges, possibly overprinting them. This is typical for flat topped parts of hybrid eskers and may indicate increased sediment supply (Storrar et al., 2020).

Halden (1936) suggested that dead ice was formed in depressions in Lake Siljan and the surrounding area during the deglaciation (Halden, 1936). South of Österviken Bay the river valley is filled with glaciofluvial sediments and in the Heden Basin melting of stagnant ice blocks have create a hummocky landscape (Möller et al., 2022). That this part of the river valley have not been filled with sediments as further south may indicate that the area was covered with large blocks of stagnant ice that may have been separated from the retreating ice margin, partly preventing sedimentation. Stagnation of ice in the bay may have been favoured by the deep and narrow conditions (Eilertsen et al., 2016).

The complex bathymetry in the southern part of Österviken Bay was in this study first interpreted as a hummocky landscape where the length, width, height, and orientation of the hills were investigated. A drumlin field was also considered, but the hills had an uncontrolled distribution and were not strictly aligned with the direction of ice flow which, together with their shape, made interpretation of them as drumlins excluded. A few longer, winding sinuous ridges running through the Österviken Bay were directly interpreted as eskers, and when looking at the slope and aspect of the hills, it seemed possible that they could be shorter, beaded esker segments that may be connected to form longer ridges (Figure 28) (Figure 47). Together with the longer eskers these ridges are here interpreted to be part of a complex, braided esker system probably connected to the Badelunda esker further south.

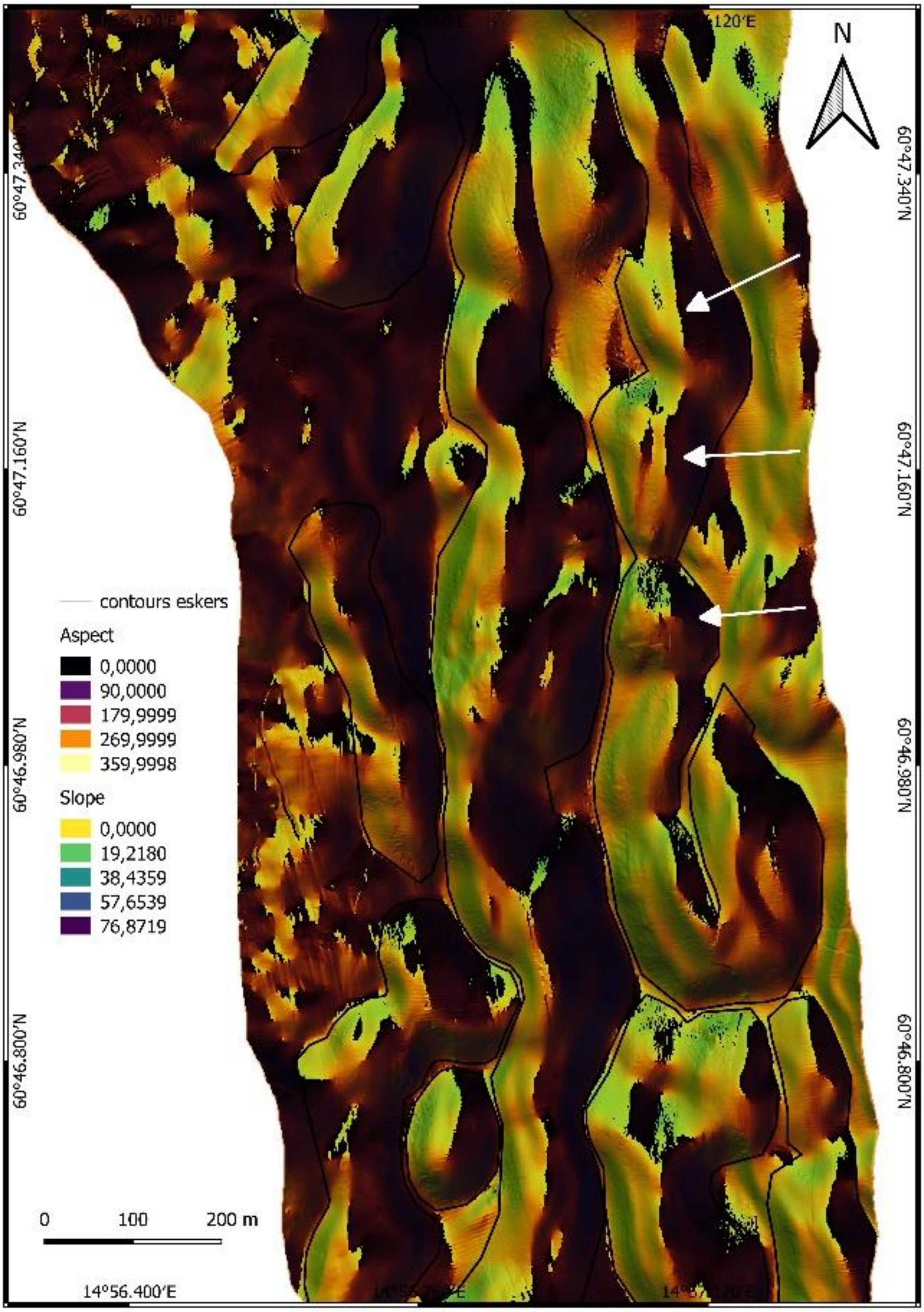

Figure 47. The figure illustrates how the slope and aspect can help when trying to connect esker segments. White arrows shows what may be parts of a beaded esker.

The landforms mapped on the bottom of Lake Siljan follows the pattern seen in the surrounding landscape with subglacial drainage systems found in the depressions of the impact structure. Fast and channelised drainage pattern with subglacial drainage channels suggests that the ice sheet was warm based during deglaciation. The erosional channels are changing into R-channels and esker formation going south. This may indicate changes in the slope of or thinning of the ice towards the south, possibly near the ice margin.

5.2. Mass-transport deposits

Of the five mass-transport deposits mapped in this part of Lake Siljan the largest (no 1) was more closely examined. Volume calculations were implemented for comparison with MTDs published in other studies in order to evaluate if MTD no 1 in Lake Siljan may have generated a tsunami. The volume was chosen as the comparative parameter since it is an important factor when it comes to MTD-induced tsunamis and is often used in tsunami simulations. Another reason for choosing the volume when comparing MTDs is that it was one of the most common characterizing parameters found in published articles. Other measurements that may have been valuable for comparison, like the vertical displacement and slope angle, are less frequently accounted for and presented in published articles. Furthermore, factors like speed and initial acceleration would be interesting to compare but are not known for the MTD in Lake Siljan and neither are the density or coherence of the material as no coring yet has been carried out. With respect to published volumes of slides in other studies, it is unfortunately common that the methods and approaches behind the calculations are rarely presented. This makes the comparison a bit inconsistent.

Volume calculations for the mass-transport deposit no 1 in Lake Siljan were first made using the sub-bottom profiles. Since the sub-bottom profiles did not cover the whole MTD, they could only be used for calculating volumes based on the largest arcuate lobe. The bottom of the MTDs masses was difficult to interpret because it was not clearly seen in the sub-bottom profiles, which make these volume calculations quite uncertain. Some problems also occurred with the interpolation of the surfaces in SonarWiz that may have affected the accuracy of the volume calculations. The volume calculation done in QGIS using the size of the failure scar is likely the more robust and representative (Figure 48). Of the two methods used for interpreting depth values of the points used for the interpolation the first one did not turn out as hoped, while the second one using depth contours gave a better result. Some differences could be seen in the resulting volume depending on the settings during the interpolation and depending on which dynamic surface was used as a DEM layer in the volume calculations (Appendix C, Table C1). The volume used in the text was calculated using the interpolated surface that looked best when comparing to the dynamic surface in Fledermaus together with the DEM layer with 0.5 m resolution.

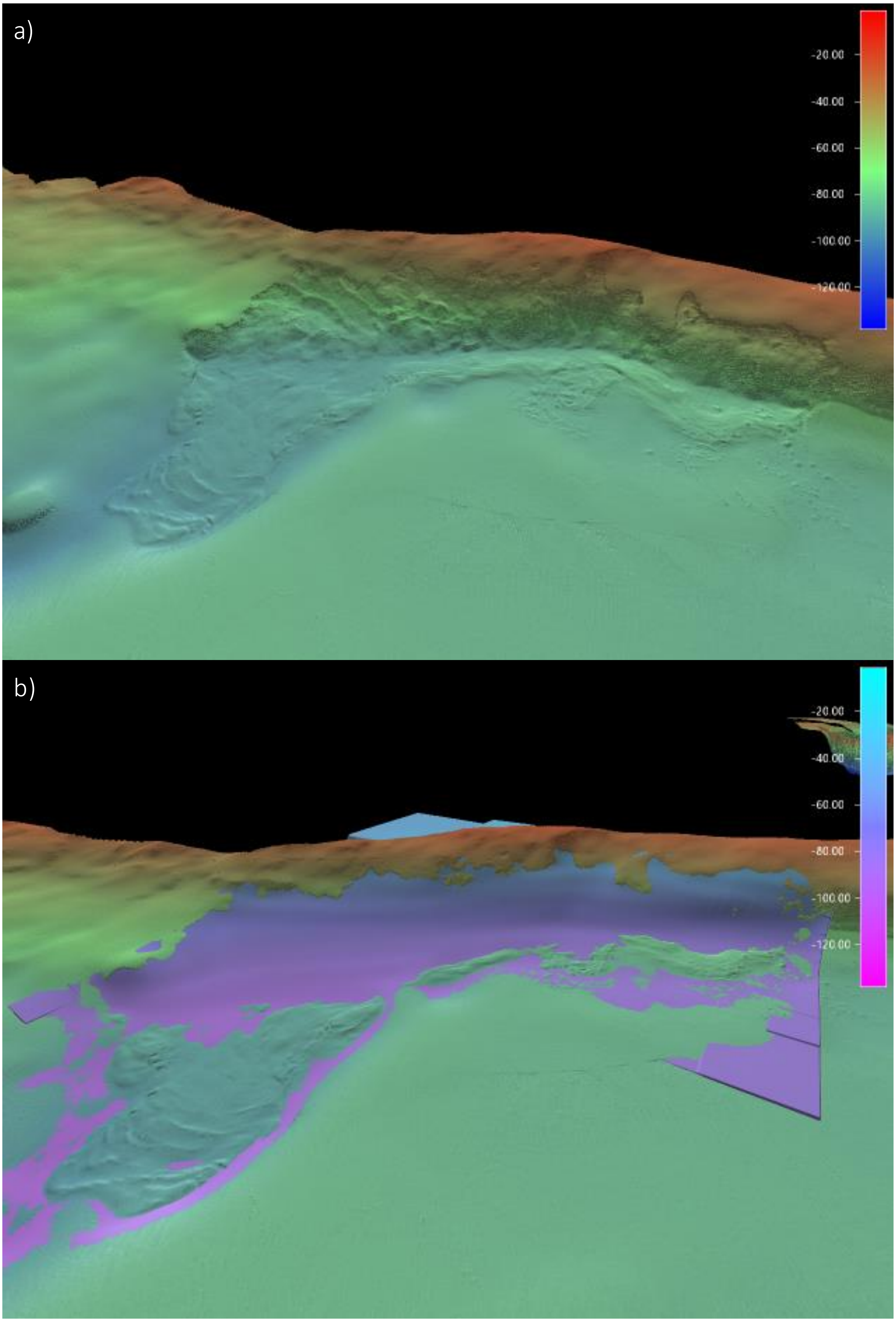

Figure 48. *a) The MTD (no 1) scar as it was mapped by the multibeam echosounder. b) The interpolated surface representing the lake floor as it may have been before the occurrence of the slide. In the area of deposition, the MTD masses are covering the interpolated surface, z=2.*

A plot was made comparing the volumes, maximum run-up height and, maximum wave amplitude of the mass-transport deposits in Table 1 together with the largest MTD no 1 in Lake Siljan (Figure 49). The largest MTDs in the list had the be removed from the plot for the smallest ones to be visualized. In the plot it is clearly seen that the largest MTD in Lake Siljan is small in comparison to many MTDs known to have induced tsunamis.

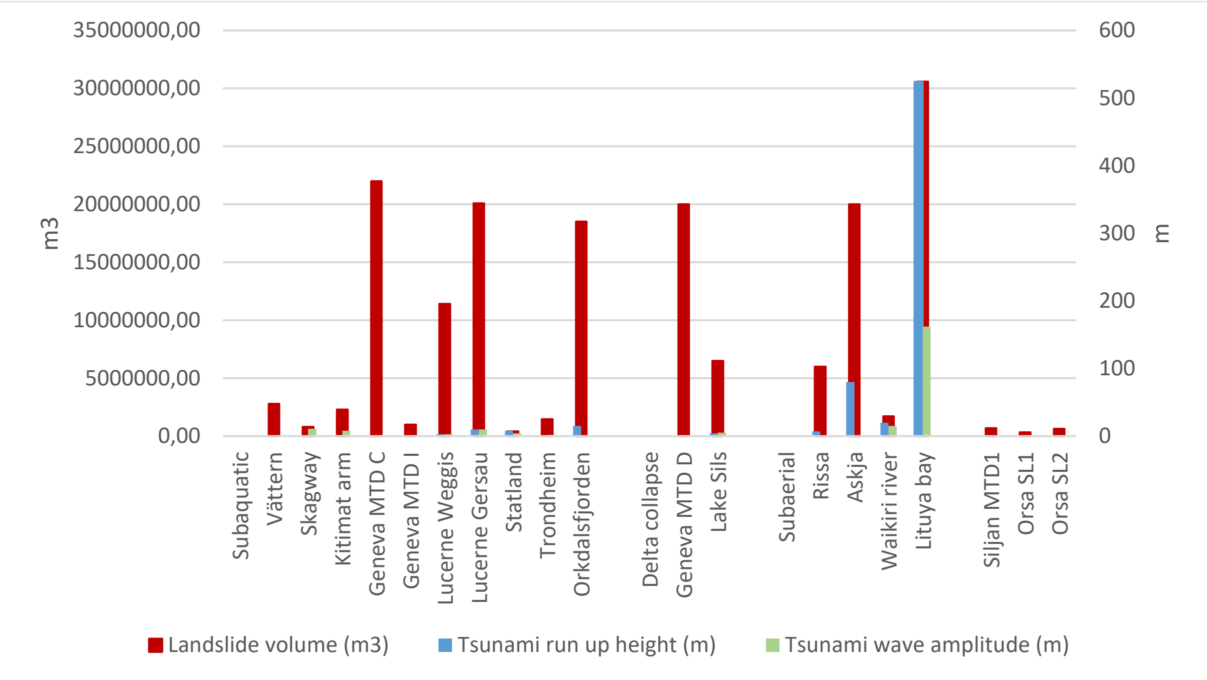

Figure 49. *Comparison of the volume, run-up height and wave amplitude of MTDs known to have caused tsunamis together with the largest MTD in Lake Siljan and the two largest MTDs in Lake Orsa.*

The mass-transport deposit closest in size, when comparing the volume, to the one in Lake Siljan occurred in Statland, Norway in 2014 with an evacuated volume of 350-400 000 m^3 (Glimsdal et al., 2016) and in Skagway Harbor, Alaska in 1994 with a volume of 800 000 m^3 (Rabinovich et al., 1999). Both the MTD in Statland and the one in Skagway differs from the MTD in Lake Siljan in that they reached the shoreline. In Skagway Harbor, 10 % of the MTD volume was subaerial (Rabinovich et al., 1999). Looking at the height difference and runout distance it was much larger in Statland than in Lake Siljan (Table 3).

Table 3. *Measurements from the MTD no 1 in Lake Siljan, with area and volume rounded to tens of m^2/m^3, and the two MTDs closest in size when comparing the volume* (Glimsdal et al., 2016), (Rabinovich et al., 1999).

MTD	Slope (°)	Area (m^2)	Volume (m^3)	Runout distance (m)	Total height difference (m)
Statland entire MTD		20000	400000	1300	380
Statland (stage 1)		8000	160000	900	377
Statland (stage 2)		12000	240000	1300	380
Siljan no 1	17	279910	678650	547	60
Skagway	30-35		0.8×10^6		

To have a Froude number close to unity the MTD no 1 in Lake Siljan would require having a speed of ~21 m/s in the shallow part and of ~30 m/s in its deepest area. This speed is within a plausible range for a subaquatic MTD at these depths. The MTD in Statland is modelled to have been moving with a speed between about 33 and 39 m/s, which the authors believed to be overestimated by the model by around 20 % (Glimsdal et al., 2016). Reducing the speed with 20 % implies that the Statland slide falls between about 26 and 31 m/s, very close to what we require to get a Froude number close to 1 in Lake Siljan. The MTD in Trondheim that occurred in 1888 was modelled to have a maximum speed of around 30 m/s (Glimsdal et al., 2013). Also here, the value is believed by the authors to have been overestimated by the model (Glimsdal et al., 2013) with the same model being used as for the Statland mass-transport deposit.

With the volume of the mass-transport deposit no1 in Lake Siljan being quite small in comparison to many known tsunami inducing MTDs it is difficult to say if it is likely to have caused a significant tsunami or not. However, comparing with the volumes of the MTD in Statland and Skagway Harbor and with the modelled MTD in Lake Tekapo, New Zealand with a volume as small as $<0.05 \times 10^6$ m^3 it seems plausible that also this mass-transport deposit may have caused a tsunami. Looking at the speed needed to get a Froude number close to unity at the depth of the MTD in Lake Siljan, the speed is possible for a mass-transport deposit. While this does not at all prove that the MTD in Lake Siljan caused a tsunami, it indicates that it is not completely unrealistic.

When the mass-transport deposit in Lake Siljan occurred in time more precisely will have to be the subject for further research. The commonly applied method to determining the age of a slide is to core the mass-wasted deposits and date the onset of post-slide sediment deposition (Urlaub et al., 2013). It is however possible to say that the MTD postdates the last glaciation and occurred after the ice had retreated from the area. First, the slides are clearly seen in the multibeam bathymetry and have not been eroded away by an overrunning ice. Second, if the landform here proposed to either be a GZW or ice proximal fan directed the flow of the largest MTD, it must have occurred after the ice had retreated from this area. When looking at the largest mass-transport deposit (no 1) and the surrounding area in Fledermaus with a large vertical exaggeration, it seems like the mass-wasted material may have been deposited in a channel that constitutes a continuation of the subglacial drainage channels found further north. This indicates that the channels were formed before the occurrence of the MTD.

Rapid deposition of sediments during the ice retreat phase and fine-grained sediments produced by the glacier may have made this area prone to mass-transport deposits. Transportation of sediments by the river Österdalälven may also have led to a high depositional rate in the surveyed channel of Lake Siljan. Rapid deposition and changes in sedimentation may lead to a build-up of an overpressure within the sediment pores and weak layers. The sub-bottom profiles reveal that the apparent basal shear plane of the large slide is coinciding with the level of the acoustic basement below layers of stratified and acoustically transparent to semi -transparent layers. This may indicate that a weak layer occurred due to changes in sedimentation. Often an external trigger is needed to cause land sliding, but without knowing the age of the MTD in Lake Siljan it is difficult to connect it to a certain event. Seismicity caused by isostatic rebound following the deglaciation may be a possible trigger (Jakobsson et al 2014). Mass-transport deposits are often occurring repeatedly on the same slopes through history and the western slope of the survey area in Lake Siljan is showing several MTD scars. This may indicate that this slope is prone to MTDs and that more MTDs than those now found may have occurred in the area and may occur in the future.

6. Conclusion

- Large parts of the survey area in Lake Siljan are covered by submarine glacial landforms. The whole area seems to be a part of a subglacial drainage system with erosional channels in the north and esker deposition in the south.
- Subglacial drainage channel indicates a warm based ice sheet during deglaciation with the partly beaded eskers indicating a stepwise retreat of the ice.
- Since channels may be re-used during different glaciations, the channels found may have existed before the last glaciation and been a part of the pre-glacial Österdalälven.

- The largest MTD found in this area of Lake Siljan with a volume of ~678650 m^3 is small compares to many of the MTD known to have induced tsunamis.
- Mass transport deposits both smaller and close in size to the one in Lake Siljan are known to have caused tsunamis, indicating that a tsunami in Lake Siljan may have been plausible.

Acknowledgements

I would like to thank my supervisor Martin Jakobsson for the opportunity to write this thesis and for help and guidance during this project. I also want to thank Anton Wagner for lots of valuable advice and support. Finally, I would like to thank Christian Gilander, Linnea Gilander and Oliver Gilander for your support and unbelievable patience during my studies.

References

Batchelor, C.L., Dowdeswell, J.A., 2015. Ice-sheet grounding-zone wedges (GZWs) on high-latitude continental margins. Mar. Geol. 363, 65–92. https://doi.org/10.1016/j.margeo.2015.02.001

Beaudoin, J., Renoud, W., Mohammadloo, T.H., Snellen, M., 2018. Automated Correction of Refraction Residuals. HYDRO18 Conf. 16.

Beigt, D., Villarosa, G., Gómez, E.A., Manzoni, C., 2016. Subaqueous landslides at the distal basin of Lago Nahuel Huapi (Argentina): Towards a tsunami hazard evaluation in Northern Patagonian lakes. Geomorphology 268, 197–206. https://doi.org/10.1016/j.geomorph.2016.06.004

Blais-Stevens A., Geertsema M., Schwab J.W., Bornhold B.D., and Mosher D.C., 2006: A Brief Overview of Landslide-Generated Tsunamis Affecting North America. *1st Speciality Conference on Disaster Mitigation*, Calgary, Alberta, Canada, May 23-26, 2006

Bondevik, S., 2022. Tsunami from the Storegga Landslide, in: Tilling, R.I. (Ed.), Complexity in Tsunamis, Volcanoes, and Their Hazards. Springer US, New York, NY, pp. 153–185. https://doi.org/10.1007/978-1-0716-1705-2_644

Calder, B.R., Mayer, L.A., 2003. Automatic processing of high-rate, high-density multibeam echosounder data. Geochem. Geophys. Geosystems 4. https://doi.org/10.1029/2002GC000486

Calles, B., 1985: Water discharges during the deglaciation of the Lake Siljan Basin, Central Sweden. *Geogr. Ann.* 67 A (1-2):101-112

Clare, M., Chaytor, J., Dabson, O., Gamboa, D., Georgiopoulou, A., Eady, H., Hunt, J., Jackson, C., Katz, O., Krastel, S., León, R., Micallef, A., Moernaut, J., Moriconi, R., Moscardelli, L., Mueller, C., Normandeau, A., Patacci, M., Steventon, M., Urlaub, M., Völker, D., Wood, L., Jobe, Z., 2019. A consistent global approach for the morphometric characterization of subaqueous landslides. Geol. Soc. Lond. Spec. Publ. 477, 455–477. https://doi.org/10.1144/SP477.15

Couston L., Mei C.C., and Alam M., 2015: Landslide tsunamis in lakes. *J. Fluid Mech*. 772, 784-804, doi:10.1017/jfm.2015.190

Dewald, N., Lewington, E.L.M., Livingstone, S.J., Clark, C.D., Storrar, R.D., 2021. Distribution, characteristics and formation of esker enlargements. Geomorphology 392, 107919. https://doi.org/10.1016/j.geomorph.2021.107919

Dowdeswell, J.A., Canals, M., Jakobsson, M., Todd, B.J., Dowdeswell, E.K., Hogan, K.A., 2016. The variety and distribution of submarine glacial landforms and implications for ice-sheet reconstruction. Geol. Soc. Lond. Mem. 46, 519–552. https://doi.org/10.1144/M46.183

Dowdeswell J.A., Canals M., Jakobsson M., Todd B.J., Dowdeswell E.K., and Hogan K.A., 2016: Introduction: An Atlas of Submarine Glacial Landforms. From: Dowdeswell J.A., Canals M., Jakobsson M., Todd B.J., Dowdeswell E.K., and Hogan K.A. (eds) 2016. *Atlas of Submarine Glacial Landforms: Modern, Quaternary and Ancient.* Geological Society, London, Memoirs, 46, 3-14, http://doi.org/10.1144/M46.171

Eilertsen R.R., Bøe R., Hermanns R., Longva O., and Dahlgren S., 2016: Kettle Holes, 'dead-ice' topography and eskers on a lake floor in Telemark, southern Norway. From: Dowdeswell J.A., Canals M., Jakobsson M., Todd B.J., Dowdeswell E.K., and Hogan K.A. (eds) 2016. *Atlas of Submarine Glacial Landforms: Modern, Quaternary and Ancient.* Geological Society, London, Memoirs, 46, 519-552, http://doi.org/10.1144/M46.44

Fjeldskaar W., Lindholm C., Dehls J.F., and Fjeldskaar I., 2000: Postglacial uplift, neotectonics and seismicity in Fennoscandia. Quaternary Science Reviews 19, 1413-1422.

Flink A.E., Noormets R., 2018: Submarine glacial landforms and sedimentary environments in Vaigattbogen, northeastern Spitsbergen. *Marine Geology* 402, 244-263, http://dx.doi.org/10.1016/j.margeo.2017.07.019

Fonseca, L., Brown, C., Calder, B., Mayer, L., Rzhanov, Y., 2009. Angular range analysis of acoustic themes from Stanton Banks Ireland: A link between visual interpretation and multibeam echosounder angular signatures. Appl. Acoust. 70, 1298–1304. https://doi.org/10.1016/j.apacoust.2008.09.008

Fonseca, L., Mayer, L., 2007. Remote estimation of surficial seafloor properties through the application Angular Range Analysis to multibeam sonar data. Mar. Geophys. Res. 28, 119–126. https://doi.org/10.1007/s11001-007-9019-4

Fonseca, L.E., Calder, B.R., 2005. Geocoder: An Efficient Backscatter Map Constructor 10.

Forwick M., Kempf P., and Laberg J.S., 2016: Eskers in deglacial sediments of three Spitsbergen fjords. From: Dowdeswell J.A., Canals M., Jakobsson M., Todd B.J., Dowdeswell E.K., and Hogan K.A. (eds) 2016. *Atlas of Submarine Glacial Landforms: Modern, Quaternary and Ancient.* Geological Society, London, Memoirs, 46, 519-552, http://doi.org/10.1144/M46.46

Fritz, H.M., Mohammed, F., Yoo, J., 2009. Lituya Bay Landslide Impact Generated Mega-Tsunami 50th Anniversary. Pure Appl. Geophys. 166, 153–175. https://doi.org/10.1007/s00024-008-0435-4

Glimsdal, S., L'Heureux, J.-S., Harbitz, C.B., Løvholt, F., 2016. The 29th January 2014 submarine landslide at Statland, Norway—landslide dynamics, tsunami generation, and run-up. Landslides 13, 1435–1444. https://doi.org/10.1007/s10346-016-0758-7

Glimsdal, S., L'Heureux, J.-S., Harbitz, C.B., Pedersen, G.K., 2013. Modelling of the 1888 Landslide Tsunami, Trondheim, Norway, in: Margottini, C., Canuti, P., Sassa, K. (Eds.), Landslide Science and Practice. Springer Berlin Heidelberg, Berlin, Heidelberg, pp. 73–79. https://doi.org/10.1007/978-3-642-31427-8_9

Greenwood, S. L., O'Regan, M., Swärd, H., Flodén, T., Ananyev, R., Chernykh, D., and Jakobsson, M., 2015, Multiple re-advances of a Lake Vättern outlet glacier during Fennoscandian Ice Sheet retreat, south-central Sweden: Boreas, v. 44, no. 4, p. 619-637 10.1111/bor.12132.

Greenwood, S.L., Clark, C.D., Hughes, A.L.C., 2007. Formalising an inversion methodology for reconstructing ice-sheet retreat patterns from meltwater channels: application to the British Ice Sheet. J. Quat. Sci. 22, 637–645. https://doi.org/10.1002/jqs.1083

Harbitz, C.B., Løvholt, F., Pedersen, G., Masson, D.G., n.d. Mechanisms of tsunami generation by submarine landslides: a short review. Nor. J. Geol. 10.

Henkel H. and Aaro S., 2005: Geophysical Investigations of the Siljan Impact Structure – A Short Review. In: Koeberl C., Henkel H. (eds) Impact Tectonics. Impact Studies. Springer, Berlin, Heidelberg. https//doi-org.ezp.sub.su.se/10.1007/3-540-27548-7_9

Hilbe, M., Anselmetti, F.S., 2015. Mass Movement-Induced Tsunami Hazard on Perialpine Lake Lucerne (Switzerland): Scenarios and Numerical Experiments. Pure Appl. Geophys. 172, 545–568. https://doi.org/10.1007/s00024-014-0907-7

Holm S., Alwmark C., Alvarez W., and Schmitz B., 2011: Shock barometry of the Siljan impact structure, Sweden. *Meteoritics & Planetary Science* 46:12, 1888-1909, https://doi-org.ezp.sub.su.se/10.1111/j.1945-5100.2011.01303.x

Holm-Alwmark S., Rae A.S.P., Ferrière L., Alwmark C., and Collins G.S., 2017: Combining shock barometry with numerical modelling: Insights into complex crater formation – The example of the Siljan impact structure (Sweden). *Meteoritics & Planetary Science* 52:12, 2521-2549, doi:101111/maps.12955

Jakobsson, M., Björck, S., O'Regan, M., Flodén, T., Greenwood, S.L., Swärd, H., Lif, A., Ampel, L., Koyi, H., Skelton, A., 2014. Major earthquake at the Pleistocene-Holocene transition in Lake Vättern, southern Sweden. Geology 42, 379–382. https://doi.org/10.1130/G35499.1

Jakobsson, M., Gyllencreutz, R., Mayer, L.A., Dowdeswell, J.A., Canals, M., Todd, B.J., Dowdeswell, E.K., Hogan, K.A., Larter, R.D., 2016a. Mapping submarine glacial landforms using acoustic methods. Geol. Soc. Lond. Mem. 46, 17–40. https://doi.org/10.1144/M46.182

Jakobsson, M., Gyllencreutz, R., Mayer, L.A., Dowdeswell, J.A., Canals, M., Todd, B.J., Dowdeswell, E.K., Hogan, K.A., Larter, R.D., 2016b. Mapping submarine glacial landforms using acoustic methods. Geol. Soc. Lond. Mem. 46, 17–40. https://doi.org/10.1144/M46.182

Jakobsson, M., Stranne, C., Fornander, R., O'Regan, M., Wagner, A., 2021. EL21-Estonia : Report of the MS Estonia shipwreck site survey with RV Electra. Stockholm University.

Juhlin C., Sturkell E., Ebbestad J.O.R., Lehnert O., Högström A.E.S., and Meinhold G., 2012: A new interpretation of the sedimentary cover in the western Siljan Ring area, central Sweden, based on seismic data. *Tectonophysics* 580, 88-89, http://dx.doi.org/10.1016/j.tecto.2012.08.040

Kirby, J.T., Shi, F., Nicolsky, D., Ma, G., Misra, S., Rao, P., 2017. The 1975 Kitimat Landslide Tsunami: Validation and Comparative Testing of Modeling Strategies, in: Coastal Structures and Solutions to Coastal Disasters 2015. Presented at the Coastal Structures and Solutions to Coastal Disasters Joint

Conference 2015, American Society of Civil Engineers, Boston, Massachusetts, pp. 13–23. https://doi.org/10.1061/9780784480311.002

Kirby, J.T., Shi, F., Nicolsky, D., Misra, S., 2016. The 27 April 1975 Kitimat, British Columbia, submarine landslide tsunami: a comparison of modeling approaches. Landslides 13, 1421–1434. https://doi.org/10.1007/s10346-016-0682-x

Kirkham, J.D., Hogan, K.A., Larter, R.D., Arnold, N.S., Nitsche, F.O., Kuhn, G., Gohl, K., Anderson, J.B., Dowdeswell, J.A., 2020. Morphometry of bedrock meltwater channels on Antarctic inner continental shelves: Implications for channel development and subglacial hydrology. Geomorphology 370, 107369. https://doi.org/10.1016/j.geomorph.2020.107369

Kokalj Ž., Zakšek K., Oštir K, Pehani P., Čotar K., and Somrak M., 2019: Relief Visualization Toolbox, ver 2.2.1, Manual. Research Centre of the Slovenian Academy of Sciences and Arts

Kremer K., Hilbe M., Simpson G., Decrouy L., Wildi W., and Girardclos S., 2015. Reconstructing 4000 years of mass movement and tsunami history in a deep peri-Alpine lake (Lake Geneva, France-Switzerland). *Sedimentology* 62:1305-1327. DOI:10.1111/sed.12190

Kremer K., Anselmetti F.S., Evers F.M., Goff J., and Nigg V., 2021: Freshwater (paleo)tsunamis – a review. *Earth-Science Reviews* 212, https://doi.org/10.1016/j.earscirev.2020.103447

Kulikov, E., Rabinovich, A., Thomson, R., Bornhold, B., 1996. The landslide tsunami of November 3, 1994, Skagway Harbor, Alaska. J. Geophys. Res. 101, 6609–6615. https://doi.org/10.1029/95JC03562

Lindhorst, K., Krastel, S., Papenberg, C., Heidarzadeh, M., 2014. Modeling Submarine Landslide-Generated Waves in Lake Ohrid, Macedonia/Albania, in: Krastel, S., Behrmann, J.-H., Völker, D., Stipp, M., Berndt, C., Urgeles, R., Chaytor, J., Huhn, K., Strasser, M., Harbitz, C.B. (Eds.), Submarine Mass Movements and Their Consequences, Advances in Natural and Technological Hazards Research.Springer International Publishing, Cham, pp. 497–506. https://doi.org/10.1007/978-3-319-00972-8_44

Lehnert O., Ahmed M., Arslan A., and Ebbestad J.O.R., 2014: Palaeogeographic setting of Upper Ordovician and Silurian source rocks preserved in the Siljan impact structure (central Sweden). *Research Gate*, Conference paper, IODP/ICDP Kolloquium

Lidmar-Bergström K. and Olvmo M., 2015: Plains, steps, hilly relief and valleys in northern Sweden – review, interpretations and implications for conclusions on Phanerozoic tectonics. *Geological Survey of Sweden*, Research Paper C 838

Liu, Z., L'Heureux, J.-S., Glimsdal, S., Lacasse, S., 2021. Modelling of mobility of Rissa landslide and following tsunami. Comput. Geotech. 140, 104388. https://doi.org/10.1016/j.compgeo.2021.104388

Livingstone, S.J., Utting, D.J., Ruffell, A., Clark, C.D., Pawley, S., Atkinson, N., Fowler, A.C., 2016. Discovery of relict subglacial lakes and their geometry and mechanism of drainage. Nat. Commun. 7, ncomms11767. https://doi.org/10.1038/ncomms11767

Lund, B., and Näslund, J., 2009: Glacial isostatic adjustment: Implications for glacially induced faulting and nuclear waste repositories. In Connor C., Chapman N., and Connor L. (Eds.), *Volcanic and Tectonic Hazard Assessment for Nuclear Facilities,* pp. 142-155. Cambridge: Cambridge University Press. doi:10.1017/CBO9780511635380.006

Løvholt, F., Glimsdal, S., Harbitz, C.B., 2020. On the landslide tsunami uncertainty and hazard. Landslides 17, 2301–2315. https://doi.org/10.1007/s10346-020-01429-z

Masson, D.G., Harbitz, C.B., Wynn, R.B., Pedersen, G., Løvholt, F., 2006. Submarine landslides: processes, triggers and hazard prediction. Philos. Trans. R. Soc. Math. Phys. Eng. Sci. 364, 2009–2039. https://doi.org/10.1098/rsta.2006.1810

Mohammadloo, T.H., Snellen, M., Renoud, W., Beaudoin, J., Simons, D.G., 2019. Correcting Multibeam Echosounder Bathymetric Measurements for Errors Induced by Inaccurate Water Column Sound Speeds. IEEE Access 7, 122052–122068. https://doi.org/10.1109/ACCESS.2019.2936170
Murty, T.S., 2003. Tsunami Wave Height Dependence on Landslide Volume. Pure Appl. Geophys. 160, 2147–2153. https://doi.org/10.1007/s00024-003-2423-z

Möller P., 2006: Rogen moraine: an example of glacial reshaping of pre-existing landforms. *Quaternary Science Reviews* 25, 362-389, https://doi.org/10.1016/j.quascirev.2005.01.011

Möller P., Björck S., Dowling T.P.F., Hammarlund D., Jakobsson M., Ljung K., Lund M., and Paradeisis-Stathis S., 2022: Deglaciation history and subsequent lake dynamics in the Siljan region, south-central Sweden, based on new LiDAR evidence and sediment records. *Earth Surface Processes and Landforms*, accepted

Orengo H.A., and Petrie C.A., 2018: Multi-Scale relief model (MSRM): a new algorithm for the visualisation of subtle topographic change of variable size in digital elevation models. *Earth Surface Processes and Landforms* 43, 1361-1369, DOI:10.1002/esp.4317

Paradeisis-Stathis S., 2020: *Holocene lake-level changes in the Siljan Lake District – Towards validation of von Post´s drainage scenario*. Master´s thesis, no 600, Dissertations in Geology at Lund University, Department of Geology, Lund University

Rabinovich, A.B., Thomson, R.E., Kulikov, E.A., Bornhold, B.D., Fine, I.V., 1999. The landslide-generated tsunami of November 3, 1994 in Skagway Harbor, Alaska: A case study. Geophys. Res. Lett. 26, 3009–3012. https://doi.org/10.1029/1999GL002334

Sammartini, M., Moernaut, J., Anselmetti, F.S., Hilbe, M., Lindhorst, K., Praet, N., Strasser, M., 2019. An Atlas of Mass-Transport Deposits in Lakes, in: Submarine Landslides. American Geophysical Union (AGU), pp. 201–226. https://doi.org/10.1002/9781119500513.ch13

Schimel, A.C.G., Beaudoin, J., Parnum, I.M., Le Bas, T., Schmidt, V., Keith, G., Ierodiaconou, D., 2018. Multibeam sonar backscatter data processing. Mar. Geophys. Res. 39, 121–137. https://doi.org/10.1007/s11001-018-9341-z

Sharp, M., 2005. Subglacial Drainage, in: Anderson, M.G., McDonnell, J.J. (Eds.), Encyclopedia of Hydrological Sciences. John Wiley & Sons, Ltd, Chichester, UK, p. hsa173. https://doi.org/10.1002/0470848944.hsa173

Shanmugam G., 2015. The landslide problem. *Journal of Palaeogeography*. 4(2): 109-166. DOI: 10.3724/SP.J.1261.2015.00071

Simkins, L.M., Greenwood, S.L., Munevar Garcia, S., Eareckson, E.A., Anderson, J.B., Prothro, L.O., 2021. Topographic Controls on Channelized Meltwater in the Subglacial Environment. Geophys. Res.

Lett. 48, e2021GL094678. https://doi.org/10.1029/2021GL094678SMHI (Sveriges meteorologiska och hydrologiska institut), 2022, Fakta om Siljan: https://www.smhi.se/kunskapsbanken/hydrologi/de-stora-sjoarna/fakta-om-siljan-1.100225

Smith, M.J., Wise, S.M., 2007. Problems of bias in mapping linear landforms from satellite imagery. Int. J. Appl. Earth Obs. Geoinformation 9, 65–78. https://doi.org/10.1016/j.jag.2006.07.002

Smith C.A., and Peterson G., 2014: Quaternary geomorphology of the Siljan area, central Sweden. *Journal of Maps* 10:4, 521-528, https://doi.org/10.1080/17445647.2014.890958

Storrar, R.D., Ewertowski, M., Tomczyk, A.M., Barr, I.D., Livingstone, S.J., Ruffell, A., Stoker, B.J., Evans, D.J.A., 2020. Equifinality and preservation potential of complex eskers. Boreas 49, 211–231. https://doi.org/10.1111/bor.12414

Strupler, M., 2017. Subaqueous landslide-triggered tsunami hazard for Lake Zurich, Switzerland 19. Strupler, M., Hilbe, M., Anselmetti, F.S., Kopf, A.J., Fleischmann, T., Strasser, M., 2017. Probabilistic stability evaluation and seismic triggering scenarios of submerged slopes in Lake Zurich (Switzerland). Geo-Mar. Lett. 37, 241–258. https://doi.org/10.1007/s00367-017-0492-8

Ståhl Emelie, 2019: Submarine landslides in Lake Orsa, central Sweden. Bachelor thesis. Department of Geological Sciences, Stockholm University

Talling, P.J., Clare M., Urlaub M., Pope E., Hunt J.E., and Watt S.F.L., 2014: Large submarine landslides on continental slopes: Geohazards, methane release, and climate change. *Oceanography* 27(2):32–45, http://dx.doi.org/10.5670/oceanog.2014.38.

Tang Q., Zhou X., Liu Z., Du D., 2005: Processing Multibeam Backscatter Data. *Marine Geodesy* 28:251-258, DOI: 10.1080/01490410500204595.

Urlaub M., Talling P.J., and Masson D.G., 2013. Timing and frequency of large submarine landslides: implications for understanding triggers and future geohazards. Quaternary Science Reviews 72:63-82, http://dx.doi.org/10.1016/j.quascirev.2013.04.020

Wang X., Mountjoy J., Power W.L., Lane E.M., 2016. Coupled Modelling of the Failure and Tsunami of a Submarine Debris Avalanche Offshore Central New Zealand, in Lamarche G. et al. (Eds.), Submarine Mass Movements and Their Consequences, Advances in Natural and Technological Hazards Research 41. Springer International Publishing, Cham, pp. 599–606. https://doi.org/10.1007/978-3-319-20979-1_60

Appendix A

Table A1: *Water level and discharge of Lake Siljan before and after it was regulated. (Source SMHI. Levels refer to RH2000)*

	Before regulation (1900-1925)	After regulation (1964-2019)
Lowest water level	159,92	159,88
Normal water level	160,16	160,03
Mean water level	161	161,17
Normal high-water level	162,74	161,99
Highest water level	163,9	163,04
Lowest water flow	26	23
Yearly mean water flow	155	156
Highest water flow	757	572

Table A2: *Water levels during survey¨*

Date	Observed	Monthly max	Monthly mean	Monthly min
7 july	161.58	162.59	161.61	161.14
8 july	161.57	162.59	161.61	161.14
9 luly	161.60	162.59	161.61	161.14
10 july	161.59	162.59	161.61	161.14

Appendix B

```
# -*- coding: utf-8 -*-
"""
Created on Fri Feb 25 11:21:06 2022

@author: linda Hoff
"""

import math

def name_outfile(textfile):
# Function for naming the outfile.
    text=textfile[:-4] # Extracts the part of the input file containing the name to be used.
    ext='mm.xyz' # Defines the extension for the output file.
    global out
    out=text+ext # Adds the extension to the name.
    return out

textfile=(input("Enter file path for input file: "))
# ex... C:\\Users\linda\OneDrive\Dokument\SU\Siljan\Backscatter\Phi.xyz
infile=open(textfile,"r")
outfile=open(name_outfile(textfile),"w")

inlines=infile.readlines()
```

```
for lines in inlines:
	m=lines.split(",")
	k=float(m[0])
	l=float(m[1])
	phi=float(m[2])
	mm=2**-phi
	outfile.write(str('{:-f},{:-f},{:-f}\n'.format(k,l,mm)))

infile.close()
outfile.close()
```

Appendix C

Table C1. The table shows the differences in resulting volume between different settings during the interpolation and with different DEM layers used in the volume calculations.

Interpolated surface	Setting during interpolation	DEM layer used in volume calculations	Volume (m^3)
Interpolated_RST_33	Tension parameter: 30 Smoothing parameter: 4 Grid size: 1	DS_Siljan-Cube_1 Grid size: 1,25 m	678684.3
Interpolated_RST_33	Tension parameter: 30 Smoothing parameter: 4 Grid size: 1	DS_Siljan-Cube_0 Grid size: 0,5 m	679674.1
Interpolated_RST_34	Tension parameter: 25 Smoothing parameter: 4 Grid size: 1	DS_Siljan-Cube_1 Grid size: 1,25 m	678661.5
Interpolated_RST_34	Tension parameter: 25 Smoothing parameter: 4 Grid size: 1	DS_Siljan-Cube_0 Grid size: 0,5 m	679656.7
Interpolated_RST_35	Tension parameter: 15 Smoothing parameter: 3 Grid size: 1	DS_Siljan-Cube_1 Grid size: 1,25 m	678092.6
Interpolated_RST_35	Tension parameter: 15 Smoothing parameter: 3 Grid size: 1	DS_Siljan-Cube_0 Grid size: 0,5 m	679112.4
Interpolated_RST_36	Tension parameter: 20 Smoothing parameter: 3 Grid size: 1	DS_Siljan-Cube_1 Grid size: 1,25 m	677646.8
Interpolated_RST_36	Tension parameter: 20 Smoothing parameter: 3 Grid size: 1	DS_Siljan-Cube_0 Grid size: 0,5 m	678650.9